

Improved Medical X-Ray Imaging Device  
Employing a CdZnTe Detector Array

6/26/95

Sponsored by

Advanced Research Projects Agency (DOD)  
U. S. Army Missile Command  
Redstone Arsenal, AL

ARPA Order 5916 Amdt 66

Issued by U.S. Army Missile Command Under  
Contract No. DAAH01-94-C-R183

Aurora Technologies Corporation  
7408 Trade St.  
San Diego CA 92121-2410

Principle Investigator: F. P. Doty

Effective date of contract: September 3, 1994  
Expiration Date: April 3, 1995

DISCLAIMER

The views and conclusions contained in this document are those of the authors and should not be interpreted as representing the official policies, either express or implied, of the Advanced Research Projects Agency or the U.S. Government.

**DISTRIBUTION STATEMENT A**

Approved for public release  
A. Distribution Unlimited

DTIC QUALITY INSPECTED 5

19950703 065

## Abstract

The goal of this program is to develop a new method of x-ray imaging in which room temperature semiconductor arrays provide direct, digitized detection. The objectives of Phase I have been achieved, and a Phase II program to develop a practical instrument for medical radiography has been outlined.

The approach of Phase I was to experimentally determine the achievable spatial resolution of monolithic cadmium zinc telluride (CZT) arrays, and to evaluate the feasibility of CZT-based imaging systems for medical radiography. For low x-ray energies useful for imaging soft tissue such as the breast, 50  $\mu\text{m}$  spatial resolution with virtually 100% detection efficiency was demonstrated, while for higher energy x-rays used for more general radiography 100 - 200  $\mu\text{m}$  spatial resolution was demonstrated. Calculated dynamic range of systems using existing commercial multiplexer readouts is 100 times that of film-screen systems.

The Phase I results provide a basis for design of  $\text{Cd}_{1-x}\text{Zn}_x\text{Te}$  instruments for x-ray radiography. The data support electron trapping rather than lateral charge diffusion as the chief mechanism for signal spreading within the semiconductor under conditions of low bias. A model was developed to design  $\text{Cd}_{1-x}\text{Zn}_x\text{Te}$  imaging arrays for radiography. Available readout technologies have been surveyed and, example detectors have been designed for current-mode imaging using a commercial readout. It is concluded that CZT imagers are presently both technically and economically feasible in scanning or focusing systems, similar to existing systems for breast imaging and fluoroscopy.

Accession For	
NTIS	CRA&I <input checked="" type="checkbox"/>
DTIC	TAB <input type="checkbox"/>
Unannounced <input type="checkbox"/>	
Justification _____	
By _____	
Distribution / _____	
Availability Codes	
Dist	Avail and / or Special
A-1	

## Table of Contents

<b>1. ABSTRACT</b>	<b>2</b>
<b>2. INTRODUCTION</b>	<b>5</b>
<b>3. EXPERIMENTAL</b>	<b>6</b>
<b>3.1 Array Fabrication</b>	<b>6</b>
<b>3.2 Test Set-up</b>	<b>6</b>
<b>4. RESULTS AND DISCUSSION</b>	<b>9</b>
<b>4.1 Test Arrays</b>	<b>9</b>
<b>4.2 Multichannel Pulse Height Analysis</b>	<b>11</b>
<b>4.2.1 Histogram Plots: Energy Resolution</b>	<b>11</b>
<b>4.2.2 Correlation Plots: Spatial Resolution</b>	<b>12</b>
<b>5. DESIGN BASIS</b>	<b>16</b>
<b>5.1 Electron Collection Efficiency Vs Thickness</b>	<b>18</b>
<b>5.2 Point Spread Function Vs Required Bias Voltage</b>	<b>19</b>
<b>5.3 Resistivity Vs Alloy Composition &amp; Temperature</b>	<b>20</b>
<b>5.4 Linear Absorption Coefficient</b>	<b>21</b>
<b>5.5 Leakage Current Density Vs Thickness</b>	<b>22</b>
<b>5.6 Leakage Current Density Vs Temperature</b>	<b>23</b>
<b>6. REVIEW OF READOUT TECHNOLOGY</b>	<b>24</b>
<b>6.1 Circuit Design and Performance</b>	<b>24</b>
<b>6.2 Fabrication Techniques and Size Limitations</b>	<b>28</b>
<b>6.3 Environmental Constraints</b>	<b>29</b>
<b>6.4 Summary</b>	<b>29</b>
<b>7. APPLICATION EXAMPLES</b>	<b>30</b>

<b>7.1 Scanned system</b>	<b>30</b>
<b>7.2 Focused system</b>	<b>33</b>
<b>8. CONCLUSIONS</b>	<b>36</b>
<b>9. APPENDIX A: RAW DATA</b>	<b>37</b>
<b>10. APPENDIX B: COMMERCIAL MUX SPECIFICATIONS</b>	<b>38</b>
<b>11. APPENDIX C: FOCUSED COLLIMATOR</b>	<b>39</b>

## 2. Introduction

X-ray radiography is an integral part of trauma care and other medical diagnostic applications. However, current film-based X-ray imaging technology has inherent technical limitations. Performance of current systems is a function of the efficiencies and spatial frequency characteristics of the intensifying screen and film as well as the dynamic range of the film. Other significant disadvantages include the time and inconvenience of chemical processing, the lack of available spectral information, and the difficulty of transmitting, enhancing and archiving the spatial information contained in a film radiograph.

The objective of this program is to develop an entirely new method of x-ray imaging in which the performance-limiting film imager is replaced by an array of room temperature semiconductor detector elements providing direct, digitized detection. The approach is made possible by this company's recent development of cadmium zinc telluride (CZT) detectors and the availability of sophisticated readout technologies developed under DOD programs. The new approach enables:

- Increased detector dynamic range.
- Substantial reduction in patient exposure.
- Virtual elimination of the tradeoff between spatial resolution and sensitivity.
- Direct pulse readout allowing energy discrimination and dual energy imaging.
- A directly digitized output which greatly facilitates electronic image enhancement, data management and rapid data transmission.
- Portable, low-power medical imaging devices that provide for remote/field use and instantaneous transmission of images from remote locations.

The Phase I goals were achieved. These goals were to demonstrate technical feasibility and ultimate clinical and economic viability of the approach, and to establish a foundation of essential information on which to build a Phase II program. The results of Phase I are given in Section 4, and a series of calculations and plots based on these results are presented in the Design Basis, Section 0. An assessment of practical readout technology available at the present time follows in Section 6, and example designs based on available readouts are developed in Section 7. It is concluded from these examples that CZT imagers are presently both technically and economically feasible in scanning or focusing systems.

### 3. Experimental

#### 3.1 Array Fabrication

A number of "counting-grade" CdZnTe detectors were fabricated for the Phase I study. This relatively low quality material was used to demonstrate the response achievable with arrays which can be easily produced in quantity. The material was diced, polished, metallized and tested for gamma response at 60 keV (before patterning) using DIGIRAD's standard manufacturing methods.

The arrays are further described in Section 4.1. Test data taken during the fabrication process are included in Appendix A.

#### 3.2 Test Set-up

The CdZnTe detector arrays were mounted in a plastic 10 pin dual in-line package (DIP). The cathode (continuous front surface) of each detector was bonded to the 1 mm thick plastic DIP body with a Au wire connection to one of the 10 pins of the DIP. The DIP package was placed in a Zero Insertion Force (ZIF) socket mounted to a printed circuit (PC) board. The central portion of the ZIF socket was drilled out to allow low energy x-rays to illuminate the detector cathode. A matching hole was drilled in the PC board. The PC board was mounted to the bottom of a standard aluminum electronics box. Bias was applied to the cathode via an SHV connector mounted to the chassis.

A Bertan 205A03R high voltage power supply was used for the bias voltage, with a two stage filter on the PC board. The segmented anode ( 8 strips plus a guard ) was formatted with 4 strips and the guard tied to one pin, and each of the four remaining strips connected to separate pins. Each of the five anode segments were coupled to a jumper to allow individual or summed strip readout.

For the tests discussed here one of the four individual strips was always DC coupled to an AMPTEK A-250 charge sensitive preamplifier (CSPA) and labeled S2. In configuration 1, each of the adjacent strips was DC coupled to A-250 CSPAs with the guard (plus four strips) coupled to ground. In configuration 2 the adjacent strips were summed and DC coupled to an A-250 CSPA with the guard also DC coupled to an A-250 CSPA. These configurations are shown in Figure 1. The CSPAs were mounted in the chassis next to the detector PC board.

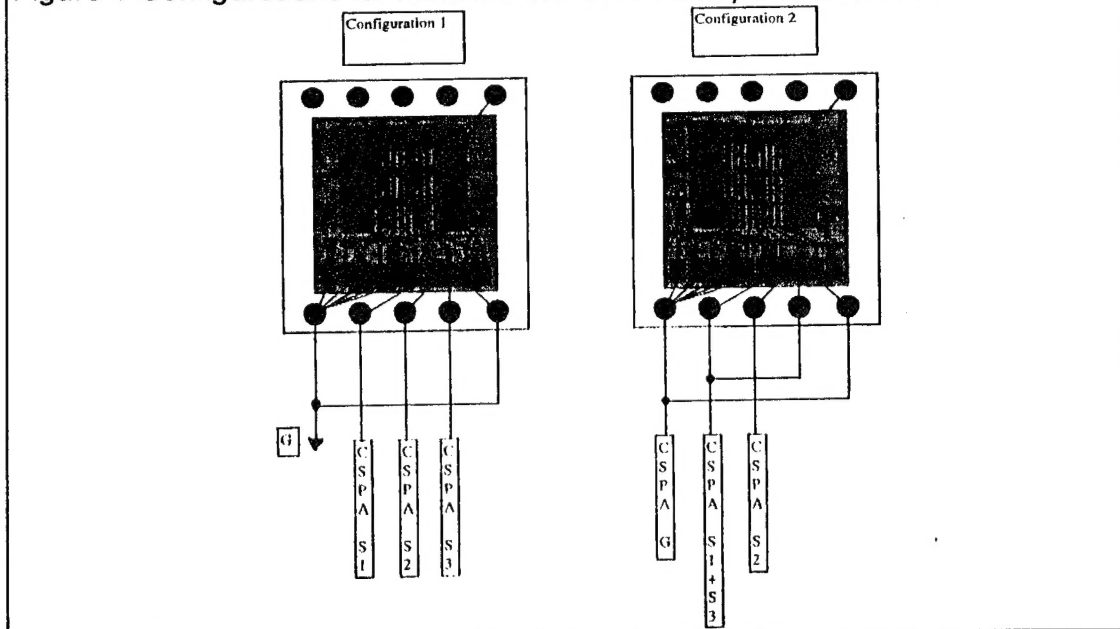
The output of each CSPA was coupled to a Canberra 2022 Spectroscopy Amplifier. The uni-polar output of each amplifier was coupled to an Ortec AD811 8-channel ADC. The AD811 is a CAMAC module under the control of a laboratory computer (486). All of the channels in the ADC are pulse height analyzed simultaneously when the AD811 strobe is asserted. The strobe pulse was obtained from an Ortec 550 SCA running in lower level discriminator mode

on the bi-polar output of the S2 amplifier. The SCA output was level converted by a Stanford Research Labs DG535 pulse generator, and the strobe width set to 4 times the value of the amplifier shaping time. All events with a signal above noise in channel S2 were recorded and logged in a file on the PC. This data was then transferred to a SUN UNIX workstation for subsequent analysis. A schematic of the test set-up for configuration 2 is seen in Figure 2 Schematic representation of the test set-up for configuration 1

Calibration data was obtained for each test configuration and detector for gain and offset corrections. This calibration data was acquired by stimulating the test input of each CSPA with tail pulses from a BNC PB-4 precision research pulser of varying amplitude. For each test the chassis was sealed for electrical shielding and light tightness. A thin aluminum window below the detector PC board allowed low energy x-rays to fall on the cathode of the detector. A 1 mm Pb shield was typically placed between the detector and the ZIF socket to shield the contact fan-out from incident radiation. In addition a collimator consisting of a 1mm hole in a 10mm thick Pb plate was used external to the chassis to limit the region of the detector illuminated by radiation.

The calibration data were used to normalize the x-ray data from each channel. This was accomplished by fitting calibration data at each amplitude with gaussians, then fitting the resulting test voltage vs. pulse height plot with a straight line. The x-ray data were normalized using the gain and offset parameters determine from the line fitting program. Results were then plotted using 'awk' and 'axis', both unix to available on the SUN workstation.

*Figure 1 Configurations for multichannel coincident pulse detection*



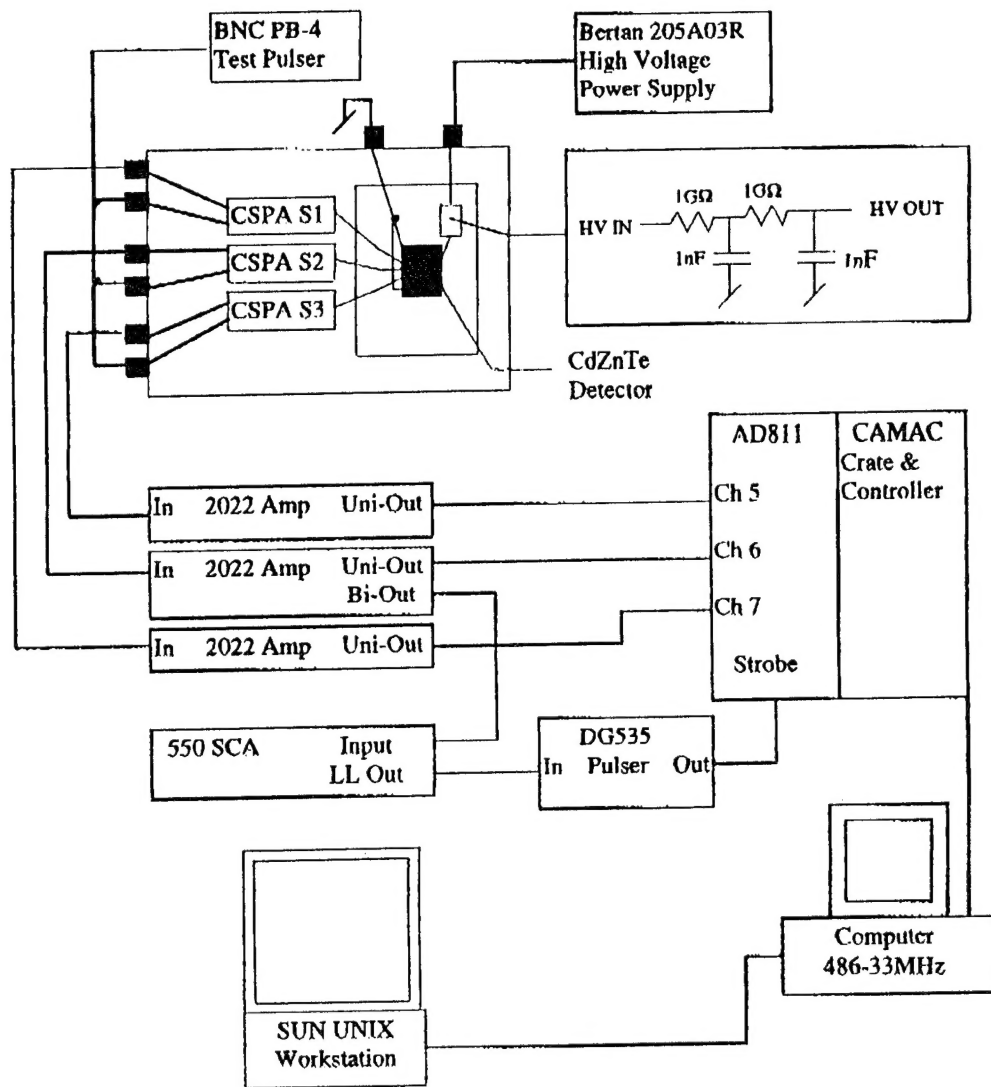


Figure 2: Schematic representation of test set-up for configuration 1.

## 4. Results and Discussion

### 4.1 Test Arrays

Characteristics of the detectors and dimensions for the arrays are reported in the table below. Pulse height spectra for the detectors prior to patterning the array strips using an  $^{241}\text{Am}$  isotopic source are included in Appendix A.

**Table 1 Detectors used in the Phase I study**

No.	Serial No.	Size (mm)	FWHM (%) @ 60 kev	Array Dimensions: Pitch, Gap (mm)
1	701899	10 x 10 x 1	NA	
2	701247	10 x 10 x 1	23.7	100, 10
3	701251	10 x 10 x 1	19.5	100, 30
4	701897	10 x 10 x 1	NA	
5	701571	10 x 10 x 2	44	400, 200
6	<b>701904</b>	<b>10 x 10 x 2</b>	<b>9.9</b>	<b>200, 100</b>
7	<b>701903</b>	<b>10 x 10 x 2</b>	<b>10.9</b>	<b>100, 50</b>
8	701898	10 x 10 x 2	19	50, 25
9	701895	10 x 10 x 3	13.4	25, 10
10	<b>701901</b>	<b>10 x 10 x 3</b>	<b>15.5</b>	<b>50, 10</b>
11	701902	10 x 10 x 3	10.6	50, 25
12	701900	10 x 10 x 3	14.	100, 40

Photographs of two of the arrays are seen in Figure 3 and Figure 4. The arrays studied extensively for this report are highlighted in **bold type** in the table. Spectra obtained from the patterned arrays are reported below.

Figure 3 Photograph of array with 200 micron strips and 200 micron gaps

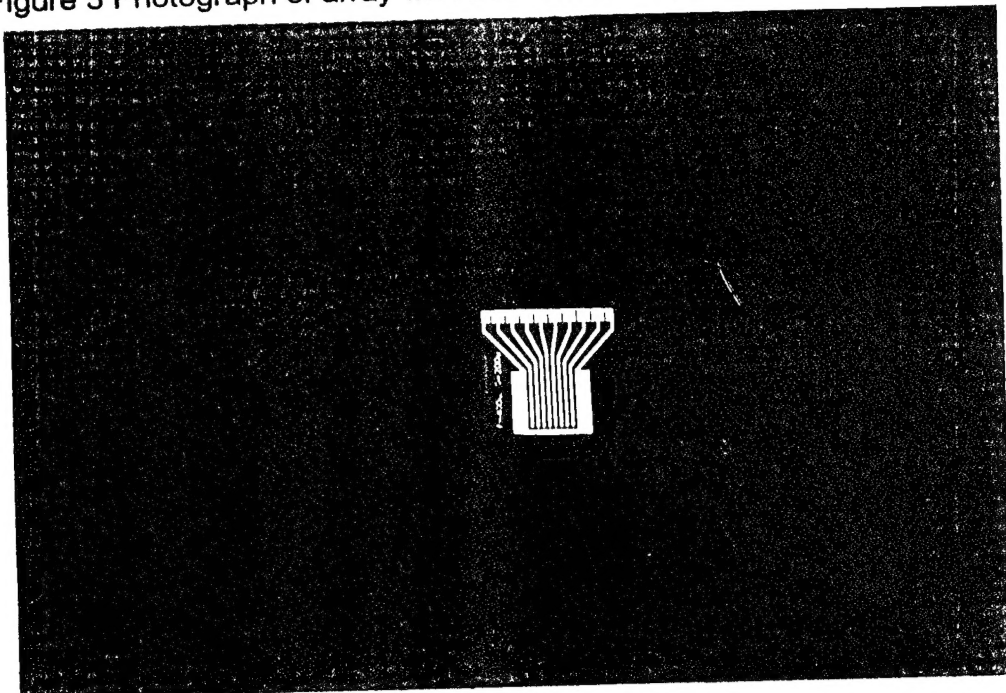
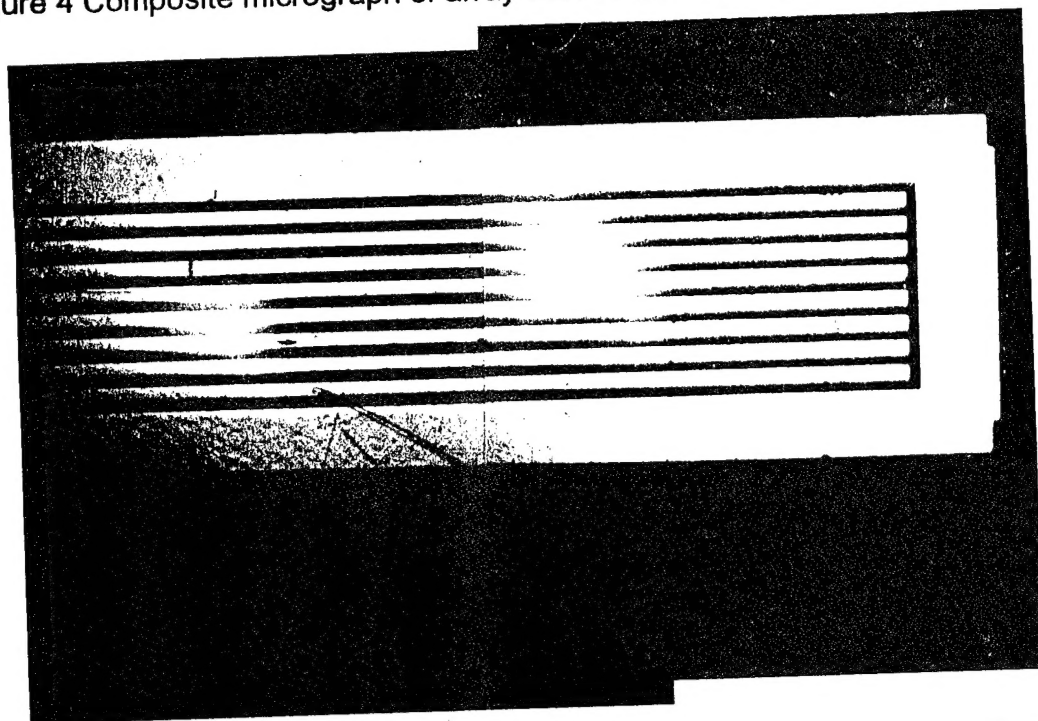


Figure 4 Composite micrograph of array with 50 micron strips and 50 micron gaps.



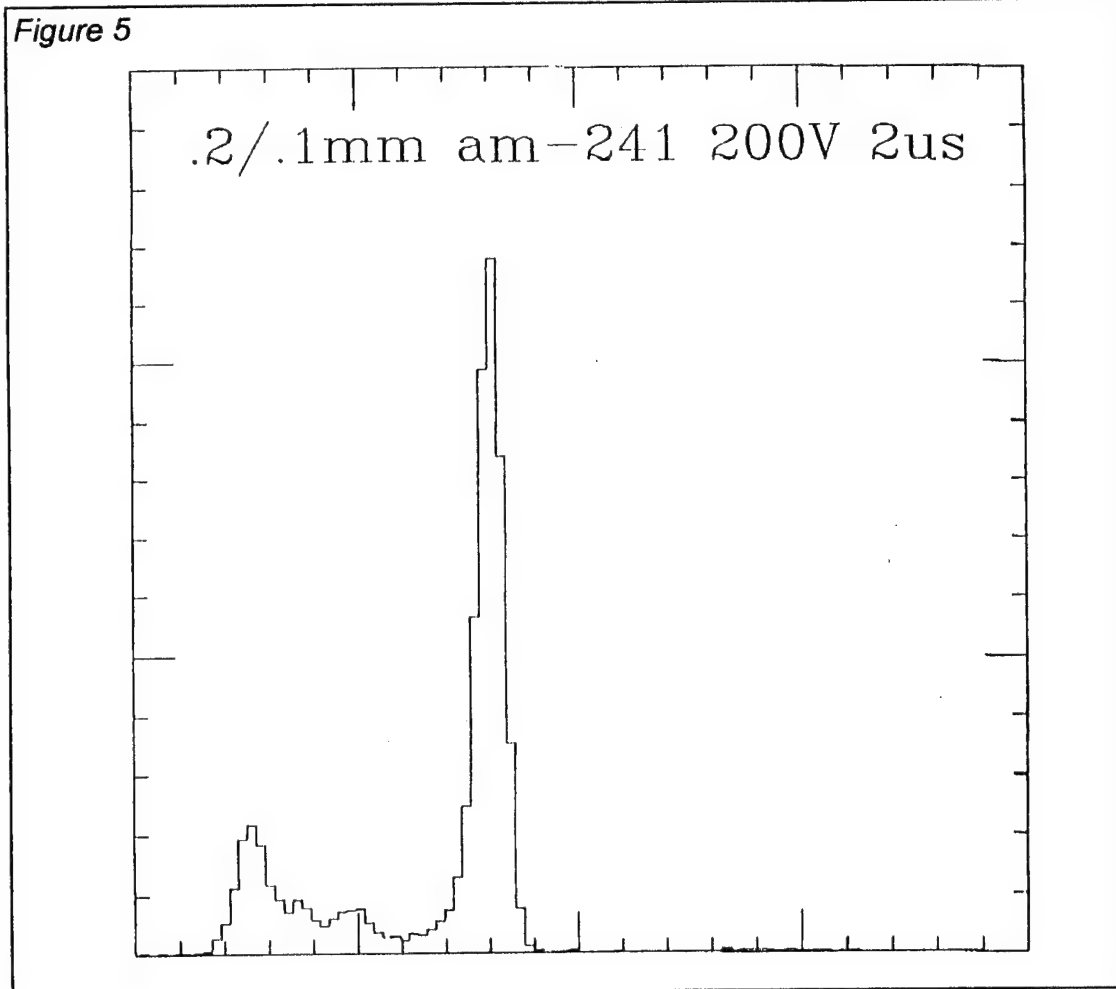
## 4.2 Multichannel Pulse Height Analysis

All data acquired with the test set described in Section 3 were stored for later analysis. Two useful ways to view the data are as histograms of various combinations of coincident pulses, and as scatter plots of coincident pulses heights on different channels or combinations of channels. A complete set of histograms and scatter plots analyzed in the phase I effort are included in this report in Appendix A. In this section the main results are summarized, analyzed and compared with predictions made in the Phase I proposal.

### 4.2.1 Histogram Plots: Energy Resolution

Isotopic sources were used to provide radiation at energies representing various x-ray applications. A typical histogram for Am-241 radiation detected with array No.6 (200  $\mu\text{m}$  pitch with 100  $\mu\text{m}$  gap) is seen in Figure 5. The energy resolution seen here is considerably better than that measured for this detector prior to segmenting the contact into strips (See Table 1). This phenomenon is generally observed, and is coming to be known as the small pixel effect, which is a subject of active investigation by DIGIRAD and other research groups. An important

Figure 5



consequence of this effect is that it enables higher production yield for a given set of performance specifications, relative to slab geometry detectors. That is,  $\text{Cd}_{1-x}\text{Zn}_x\text{Te}$  pixel detector processing is tolerant of variations in material quality.

One isotope used to irradiate the detectors was Cd-109, providing a line at 88 keV which is near the average energy used for fluoroscopy and orthopedic radiography, and the x-rays of Ag from 22 to 25 keV, which simulate sources used for imaging soft tissue such as the breast. Histogram spectra from the various isotopes and array configurations are found in Appendix A.

Figure 7 Pulse histograms of Cd109 radiation detected with 100 micron strip detector shows a series of Cd109 histograms from detector No. 7 (100  $\mu\text{m}$  pitch, 50  $\mu\text{m}$  gap). In this figure the effective strip width is varied from essentially infinity ( $S_1+S_2+S_3+G$ ) to 100  $\mu\text{m}$  ( $S_1$ ) by plotting the sums of the individual strip responses and the guard. It is seen that the Ag x-ray peak is not strongly affected, whereas the 88 keV gamma peak decreases with the effective collecting strip width. This is in accord with the predictions of the proposal, since the gamma ray is above the K-edges of Cd and Te atoms in the semiconductor ( $>27$  keV). Photons above this energy excite fluorescent x-rays in the  $\text{Cd}_{1-x}\text{Zn}_x\text{Te}$ , which have absorption lengths near 100  $\mu\text{m}$ .

Results such as the above show that signal is spread out under certain conditions, but contain no information on the distribution of signal among the collecting electrodes. In the next section correlation plots are used to show that the signal spreading is usually restricted, and signal strength is conserved, under appropriate operating conditions for imaging.

#### 4.2.2 Correlation Plots: Spatial Resolution

Spatial resolution of  $\text{Cd}_{1-x}\text{Zn}_x\text{Te}$  arrays for various pitch, thickness, bias voltage and photon energy are determined from the scatter plots in Appendix A. The coincident pulse heights on adjacent detector strips are correlated in these plots to reveal the magnitude of signal-spreading in the semiconductor. Three main observations can be made from the data:

1. At high bias voltage signal is generally collected onto a single strip or shared with *only one adjacent strip*, and the summed amplitude is constant.
2. For high energy photons ( $>27$  keV) at high bias, signal spreading onto two or more adjacent strips occurs when the strip width is reduced below 100 microns, and the summed amplitude remains constant.
3. For all photon energies, at low bias voltage the signal is spread over more than two adjacent strips, and the summed amplitude is reduced.

That charge is conserved is evident in the typical correlation plot of Figure 6. Cd109 radiation was used for these experiments, and two distributions of pulses, corresponding to the 88 and  $\sim$ 25 keV peaks, can be seen. Recall that the readout system triggers on strip no. 2, and records the pulses occurring simultaneously on strips 1,2 and 3. These data show a proportional sharing of the signal charge between Strip 2 (S2) and its neighbors.

A series of correlation plots illustrating the spatial extent of the sharing as a function of bias voltage are shown in Figure 8. In this series the bias voltage on a 2 mm thick, 200  $\mu$ m pitch array is reduced from 800 volts to 10 volts, and the signal is seen to gradually spread and reduce in magnitude. In the 800 v plot all pulses lie on the axes, showing that charge is confined to two strips for all these events (that is the trigger, strip 2 (not plotted) and either 1 or 3) . This condition obtains over all bias levels down to about 50 v, where a significant number of events begin to register on 1 and 3 simultaneously. At about 20 volts there is no longer any clustering of pulses near the axes. This means that the point spread function for this 200  $\mu$ m array degrades to  $>600$   $\mu$ m at about 20 volt bias. This is not in accord to predictions made in the proposal, where lateral diffusion of the charge cloud was assumed to be the mechanism for charge spreading at low bias.

In addition to the lateral signal spreading, Figure 8 shows that the integrated charge is diminished drastically in the lower bias experiments. Both of these observations are accounted for by the phenomenon of electron trapping. For a 2 mm thick  $\text{Cd}_{1-x}\text{Zn}_x\text{Te}$  crystal with typical  $\mu_e\tau_e$  product, the collection efficiency for electrons is approximately 50 % at 50 volts bias. It is thus reasonable to expect the onset of degradation of the point spread function at about this level. The trapped charges result in a loss of integrated signal, and result in induced signal on all the strips, in relation to  $1/R_i^2$ , R being the distance between strip i and the trapping site.

Figure 6 Correlation plot

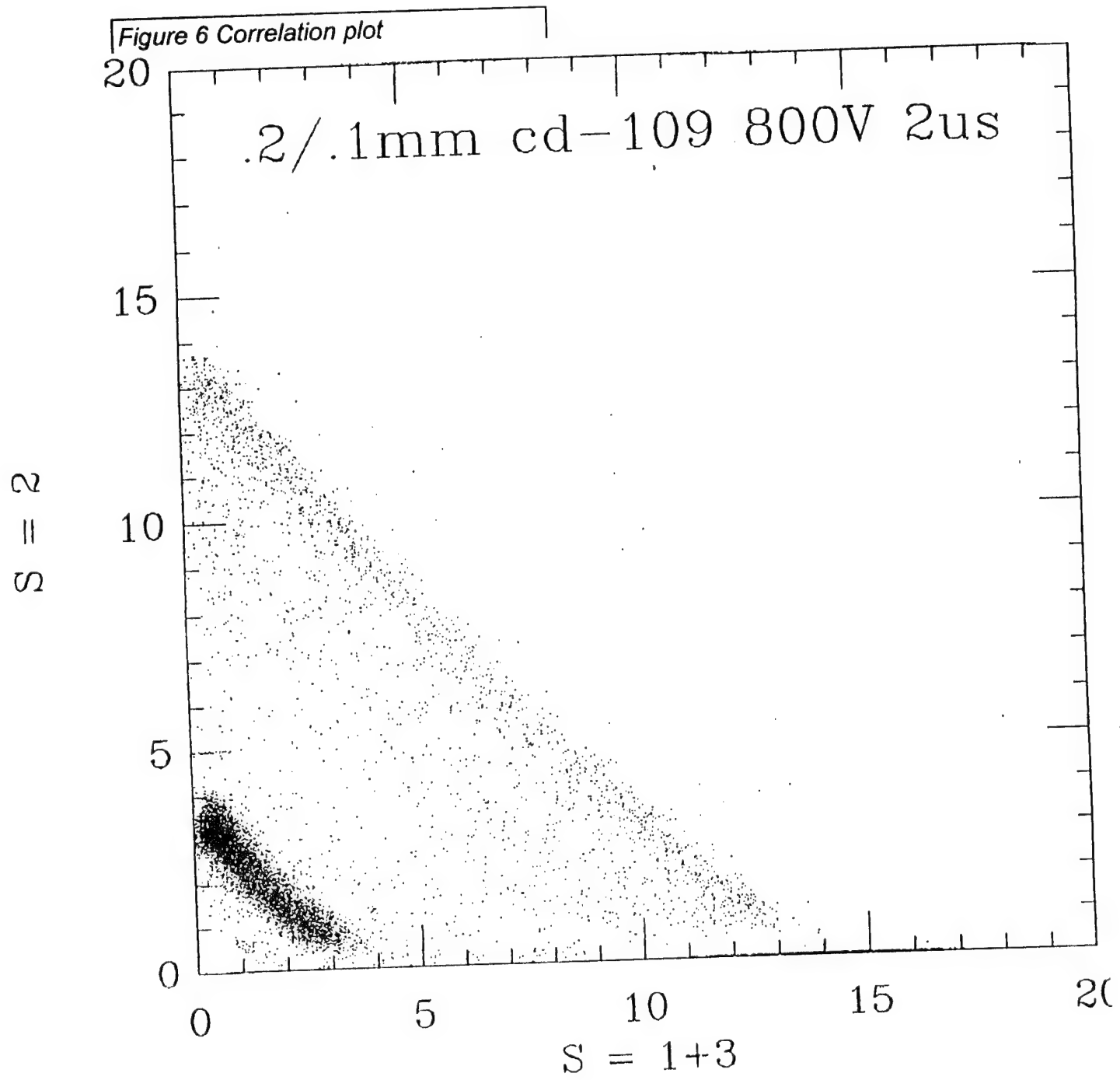


Figure 7 Pulse histograms of Cd109 radiation detected with 100 micron strip detector

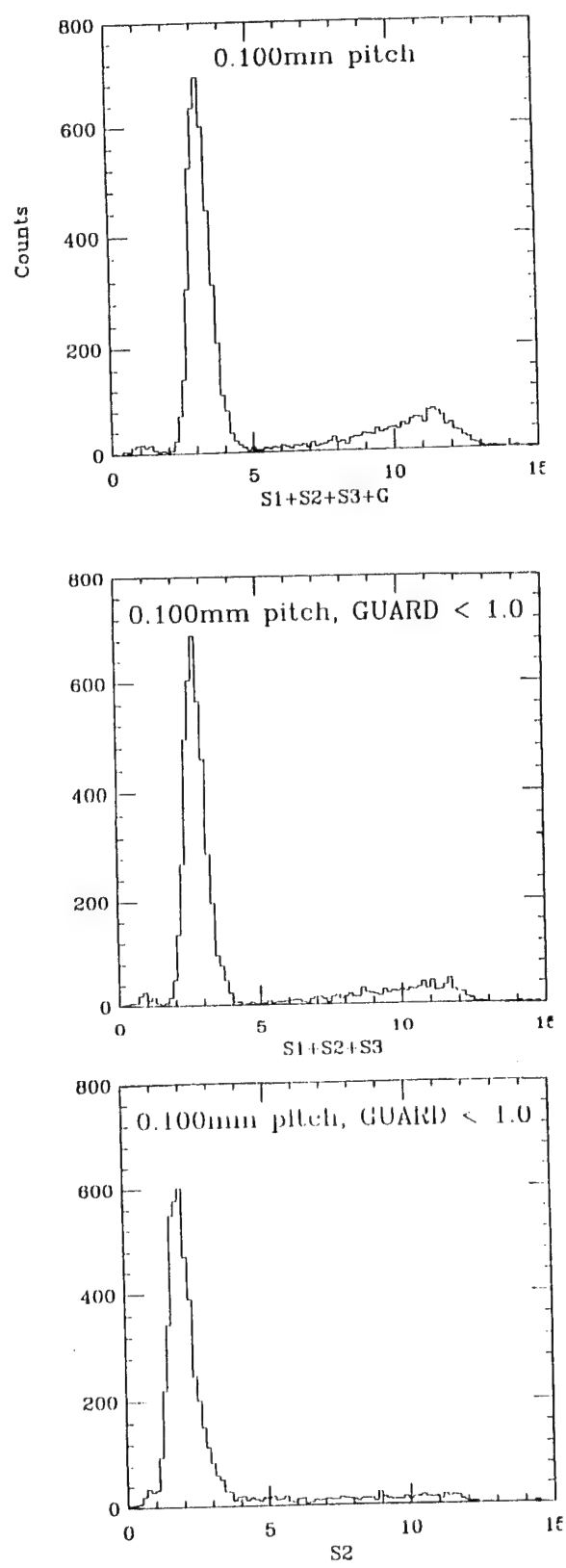
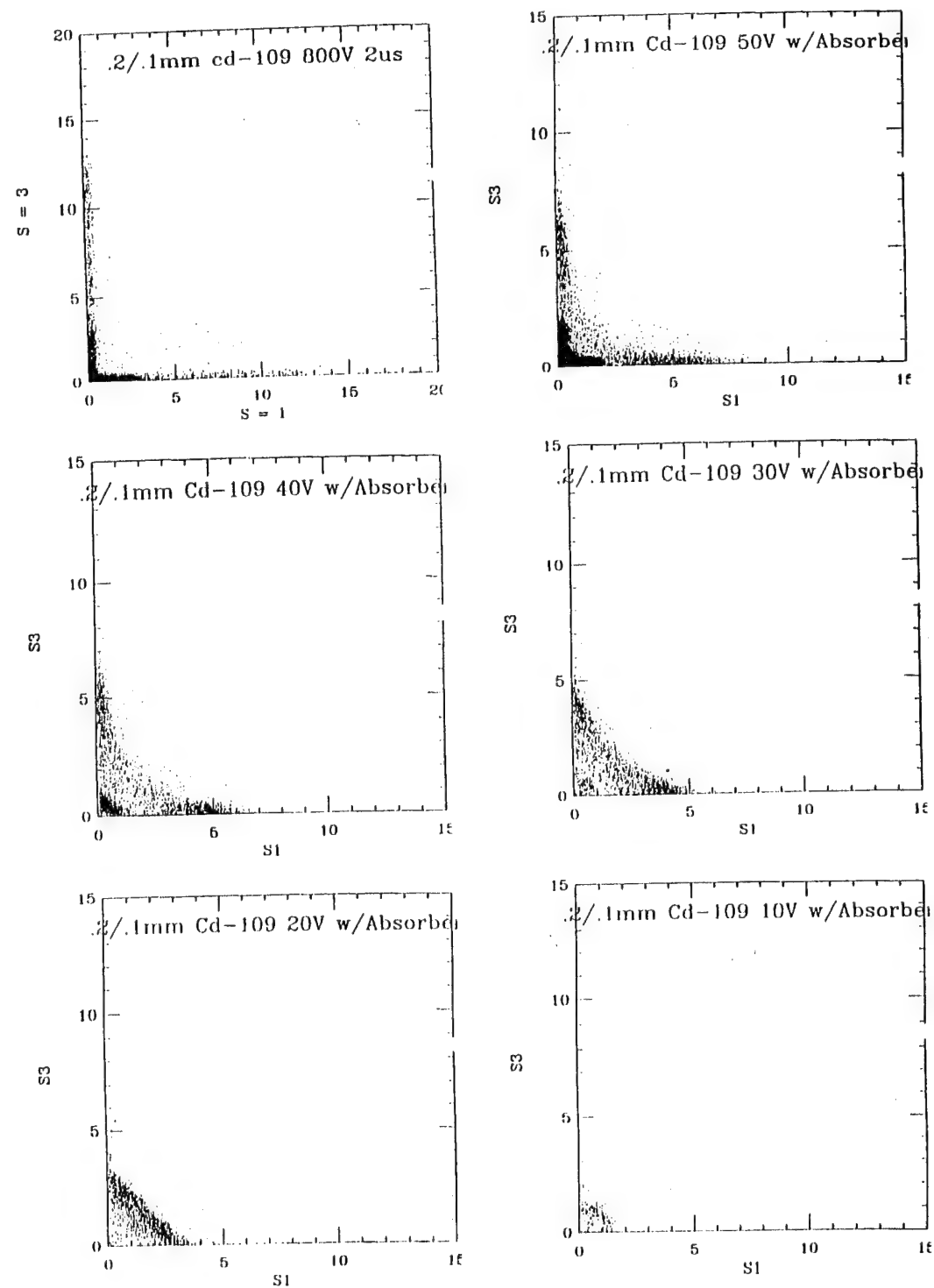


Figure 8



## 5. Design Basis

The equations below derive from the Phase I measurements, published data and standard equations of the physics of semiconductors. These equations model operating characteristics and can be used to design and predict performance of  $\text{Cd}_{1-x}\text{Zn}_x\text{Te}$  arrays for radiography.

Specific designs are developed in section 7, beginning on page 30. In these examples the specifications of a commercial multiplexer are used, to illustrate the feasibility of designing  $\text{Cd}_{1-x}\text{Zn}_x\text{Te}$  instruments for radiography with existing readout technology. The examples given are intended to illustrate the Design Basis developed in the Phase I program. Carrying out these calculations in the suggested order gives reasonable first-cut design specifications for imaging  $\text{Cd}_{1-x}\text{Zn}_x\text{Te}$  arrays. The parameters used for specific applications will vary from those used in the examples.

## 5.1 Electron Collection Efficiency Vs Thickness

The plot below, based on typical measured transport properties for electrons in  $\text{Cd}_{1-x}\text{Zn}_x\text{Te}$ , provides a graphic analysis of the charge collection efficiency achievable at low bias voltages for arrays of various thickness.

### Assign Range Variables for Voltage and Thickness

$$j := 1..1001 \quad i := 1..10$$

$$v_j := \frac{j}{2} \quad d_i := \frac{i}{10}$$

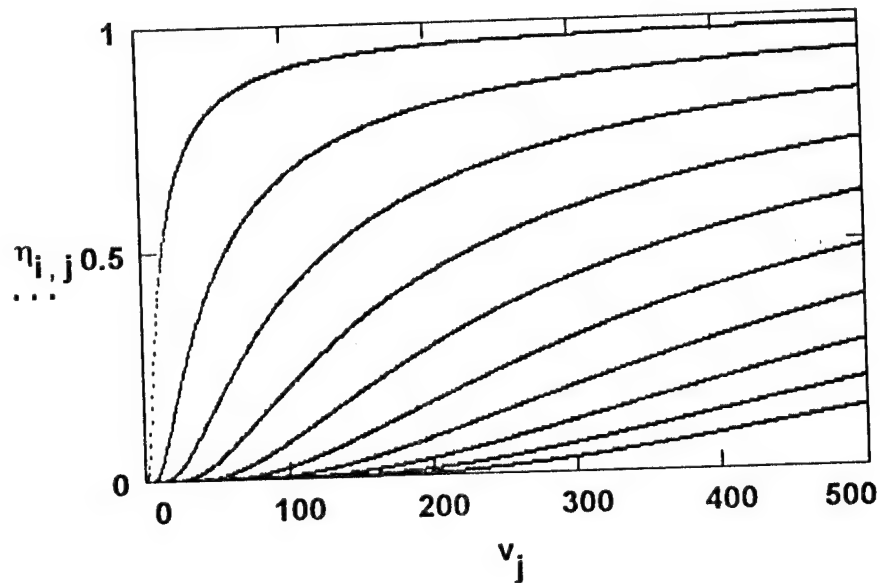
### Define Constants

$$\mu := 1000 \quad \tau := .000001$$

### Calculate Efficiency Matrix

$$\eta_{i,j} := e^{-\left[ \frac{(d_i)^2}{\mu \cdot \tau \cdot v_j} \right]}$$

### Plot Electron Collection Efficiency Vs Voltage, $V$ for Thicknesses 0.1 through 1.0 cm



## 5.2 Point Spread Function Vs Required Bias Voltage

Electron trapping at low bias voltage determines the minimum bias voltage for operating high spatial resolution arrays. The calculation below is based on the criterion that a minimum fraction of the charge generated by the x-ray absorption event be collected in order to maintain the spatial information in the image. That is, a fraction of the charge generated  $\eta$  must drift to within one pixel diameter of the collecting electrode.

These curves provide estimates for minimum operating voltage of arrays designed for a given stopping power and spatial resolution. For example, it is seen that a 2mm thick array with 50 micron pixels must be biased to at least 50 volts. Operating at voltages above this will result in slightly improved spatial resolution in current-mode, at the expense of dynamic range.

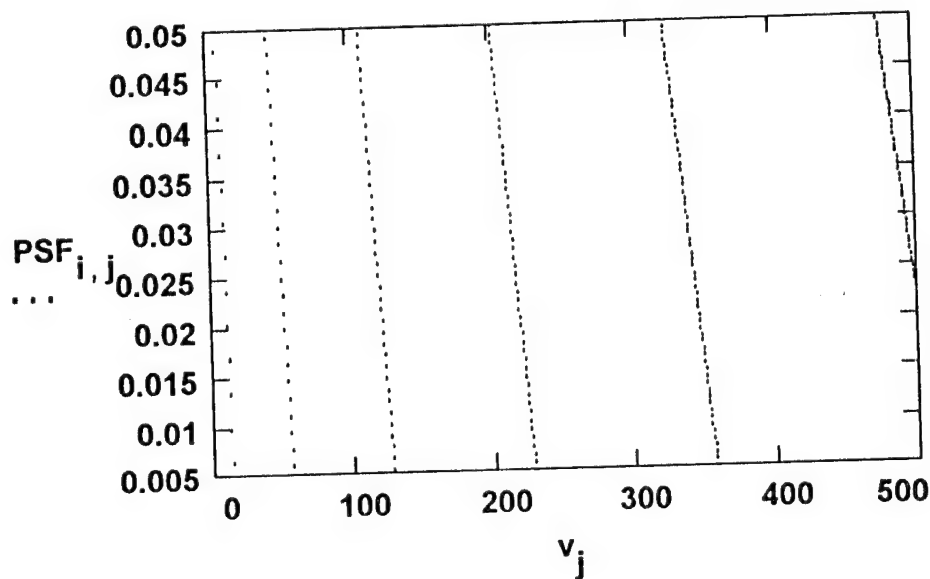
### Choose Minimum Electron Collection Efficiency

$$\eta := 0.5$$

Assume Minimum PSF Equals Depth of  $\eta$  Plane

$$\text{PSF}_{i,j} := \frac{(d_i)^2 + \mu \cdot \tau \cdot v_j \cdot \ln(\eta)}{d_i}$$

Plot Point Spread Function, cm Vs Applied Bias, V  
for Thickness  $\geq 0.1\text{cm}$



### 5.3 Resistivity Vs Alloy Composition & Temperature

Having determined the operating voltage above, the resulting minimum leakage current can be evaluated. The bulk resistivity of the  $\text{Cd}_{1-x}\text{Zn}_x\text{Te}$  material controls leakage current, an important noise source in detector arrays. This material property can be controlled through alloy composition and operating temperature. Curves for this parameter are calculated below.

#### Alloy Range Variable

$$I := 1..3$$

$$x_I := \frac{I - 1}{10}$$

#### Temperature Range Variable

$$m := 1..400$$

$$T_m := 400 - \frac{25 \cdot m}{50}$$

#### Calculate Resistivity, $\Omega\text{-cm}$

$$\rho_0 = 2.907 \cdot 10^{-3}$$

$$\rho_{I, m} := \rho_0 \cdot e^{\frac{E_I}{2 \cdot k \cdot T_m}}$$

#### Constants

$$k := 8.613 \cdot 10^{-5}$$

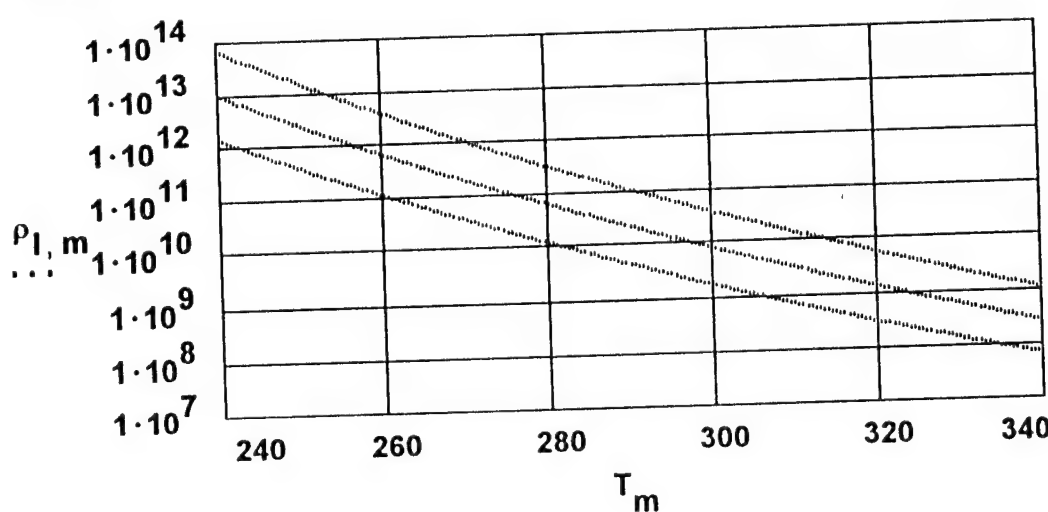
$$\rho_0 := 2.907 \cdot 10^{-3} \text{ eV/K}$$

#### Bandgap Variable, eV

$$E_I := 1.4 \cdot (1 - x_I) + 2.2 \cdot x_I$$

#### Plot Resistivity of $\text{Cd}(1-x)\text{Zn}(x)\text{Te}$ Vs Temperature,

$$x = 0.0, 0.1, 0.2$$

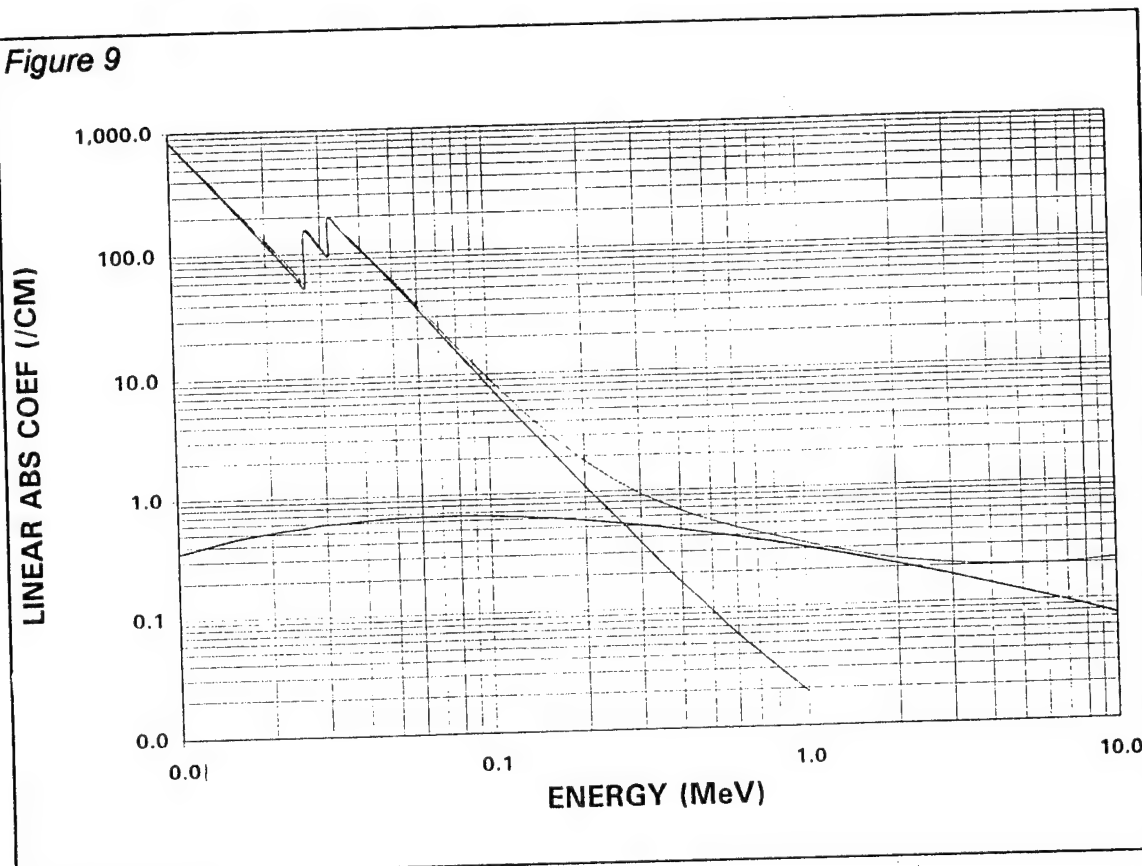


## 5.4 Linear Absorption Coefficient Vs X-Ray Energy

A plot of linear absorption coefficient versus photon energy for  $\text{Cd}_{0.8}\text{Zn}_{0.2}\text{Te}$  is shown in Figure 9 below. This plot is used to determine the thickness required for a given application i.e. a given photon energy and desired efficiency.

The cross-section data used to derive these curves were taken from the University of California Radiation Laboratory standard compilation of evaluated cross-sections. There is a slight difference in absorption for  $\text{Cd}_{1-x}\text{Zn}_x\text{Te}$  alloys in the range  $0 < x < 0.2$ . The 20% alloy was chosen as a conservative representation, since it has the lowest cross-sections.

Figure 9



## 5.5 Leakage Current Density Vs Thickness

The resistivity determined above is used to compute trade-offs between the leakage current of the device and detector thickness or pitch. In the example calculation below, the minimum charge collection is again assumed, as well as the resistivity of the 10% alloy at room temperature, to plot the trade-off with thickness.

The tolerable level of dark current will depend on the mode of operation, pixel size, source strength, readout parameters, etc. In a complete analysis, the effect on image quality of reduced quantum efficiency in a thinner array would be weighed against the improved SNR resulting from lower leakage current noise.

### Choose Collection Efficiency

$$\eta := 0.5$$

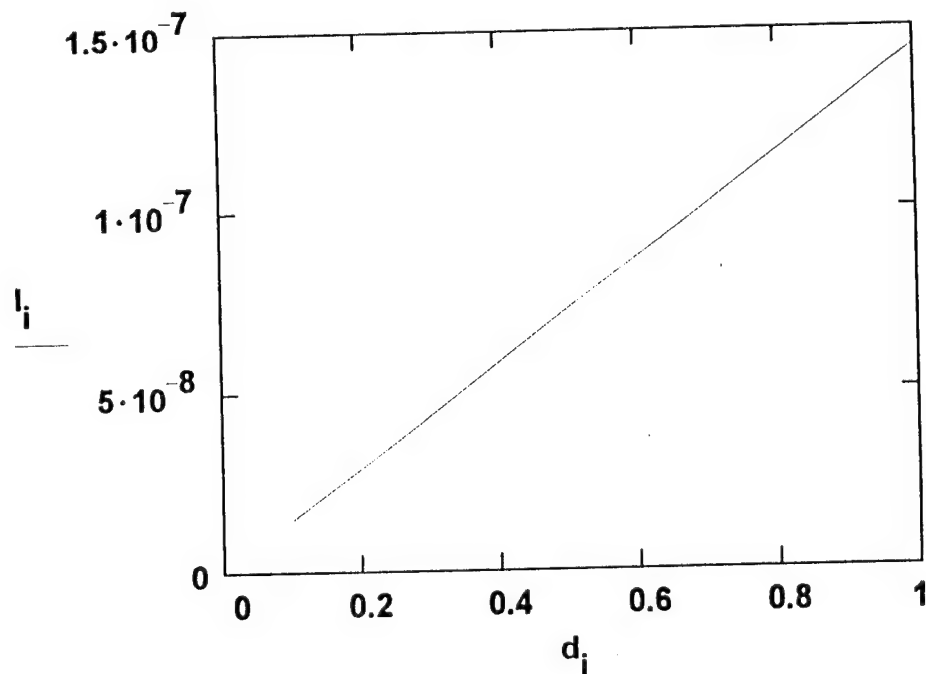
### Choose Resistivity

$$\rho := 1 \cdot 10^{10}$$

### Calculate Leakage Current Density, A/cm<sup>2</sup>

$$I_i := - \left( \frac{d_i}{\mu \cdot \tau \cdot \ln(\eta) \cdot \rho} \right)$$

### Plot Leakage Current Density, A/cm<sup>2</sup> Vs Thickness, cm



## 5.6 Leakage Current Density Vs Temperature

Properly designed detectors will maintain a minimum level of performance over a specified range of operating temperatures. The curves calculated below are useful in predicting noise performance under conditions of varying temperature. It is seen that dark current is strongly dependent on the temperature and alloy composition. These facts could be used to mitigate leakage current noise in cases of thick arrays for high stopping power, large pixels, or low source strength.

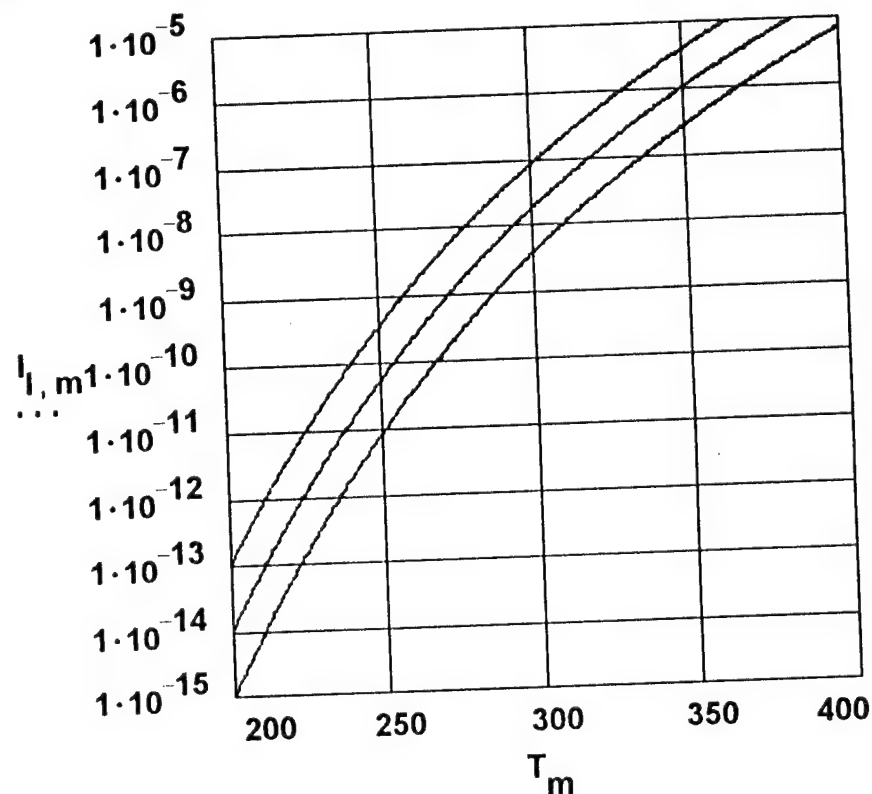
**Choose Thickness, cm**

$$d := .1$$

**Calculate Leakage Current Density, A/cm<sup>2</sup>**

$$I_{l, m} := \frac{d}{\mu \cdot \tau \cdot \ln(\eta) \cdot \rho_0 \cdot e} \left( \frac{E_l}{2 \cdot k \cdot T_m} \right)$$

**Plot Leakage Current Density, A/cm<sup>2</sup> Vs Temperature, K**



## 6. Review of Readout Technology

The key elements of the readout technologies to support CdZnTe X-ray imaging fall into three categories: circuit design and performance, fabrication techniques and size limitations, and environmental constraints. This effort addressed these elements through a literature search, a review of commercially available arrays, and a basic analysis of the parameters of the X-ray imaging system.

### 6.1 Circuit Design and Performance

An extensive literature search provided insight into the current state of readout electronics for CdZnTe applications. There are two classes of devices: integrating charge amplifiers for imaging systems and pulse shaping amplifiers for spectroscopy systems. The pulse shaping amplifiers are more complex than the simple integrators and require more circuitry for each readout channel or unit cell corresponding to a detector pixel. The result is more silicon area per channel and a lower density readout. Current pulse shaper designs require approximately  $180\mu\text{m} \times 180\mu\text{m}$  per unit cell for an area array. The first stage of pre-amplification in the pulse shaping design is done with an integrating charge amplifier while the pulse shaping and filtering is done in later stages. A representative example of the work in this area is given in the paper by Haneue, *et al*<sup>1</sup>. However, for imaging applications, an integrating charge amplifier is the more appropriate circuit choice. The remainder of this section will address integrating amplifiers.

The integrating charge amplifier was developed for military IR applications when the single element detectors and discrete transimpedance amplifiers (TIAs) gave way to linear and two-dimensional detector arrays in the early 1980s. The simplest form of this device is the source follower per detector (SFD), illustrated in Figure 10<sup>2</sup>. This is a single MOSFET source follower combined with MOSFET switches that control reset and enabling functions. The integration is performed on the parasitic input capacitance of the source follower MOSFET. The principal

---

<sup>1</sup> [1] J.A. Haneue, B.E. Boser, and B.H. Hasegawa, 1994 IEEE Nuclear Science Symposium and Medical Imaging Conference Record, Norfolk VA., (1994), p. 1762.

<sup>2</sup> P.L. Augustine, Nuclear Instruments and Methods in Physics Research A 353 (1994) 201-204.

drawback of the SFD is that signal voltage appears at the input and debiases the detector, which may cause increased crosstalk between detector pixels. The main advantage of the SFD circuit is that its simplicity allows it to be fabricated in a very small area, say  $25\mu\text{m} \times 25\mu\text{m}$ . This packing density results in the highest spatial resolution of the available circuit types.

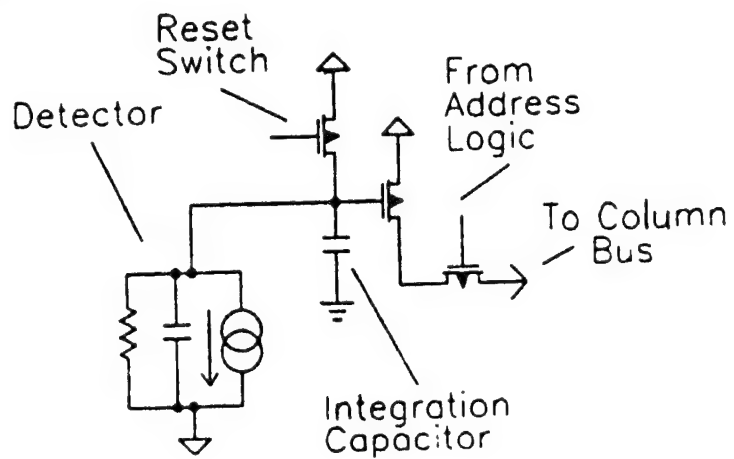
The capacitive-feedback transimpedance amplifier (CTIA) addresses the shortcomings of the SFD with a slight penalty in packing density. Considering the anticipated pixel size of the CdZnTe arrays for the X-ray imager is  $50-100\mu\text{m}$  the CTIA is a desirable circuit. The CTIA is shown in Figure 11. The key feature is a high gain amplifier with a resettable integrating capacitor in the feedback path. Because of the high gain amplifier, the detector node voltage level is fixed and the detector bias voltage does not change with increasing integration time and charge buildup on the capacitor as on the SFD. Other functions such as bandwidth-limiting, and sample/hold for correlated double sampling (CDS) and simultaneous integration can be included within the unit cell to provide a better noise performance by reducing other noise sources such as  $kTC$  and  $1/f$ .

Both the SFD and CTIA area arrays have difficulty with the charge handling capability requirements imposed by x-ray imaging applications. Integrating charge from a large enough number of x-rays to yield an image which is limited by photon statistics requires an integrating capacitor which is too large to easily fit in the pixel. It is possible, however to read the array out more quickly, but that requires more outputs from the readout due to internal chip bandwidth limitations, as well as more complicated acquisition electronics. The charge handling capacity limitation is eased, however, for a linear array. Because the readout channel must be narrow in only one dimension, the channel can be made wide enough to accommodate a large integrating capacitor.

Presently, there are two commercially available linear readout arrays. EG&G Reticon produces a family of CMOS amplifier-multiplexer arrays of 64, 128, and 256 channels (RL0064/0128/0256MB) and Rutherford Appleton Laboratory produces a 128 channel CMOS charge amplifier array (RAL138/MX3). Schematically both are identical with the major differences being a larger integrating capacitor on the EG&G Reticon array, and a variable band-limiting function in each channel of the RAL array. The Reticon array uses a  $15\text{ pF}$  feedback capacitor for a charge handling capacity of approximately  $5 \times 10^8$  electrons with a noise performance of 1500 electrons and a charge conversion of  $1\mu\text{V}/100\text{e}^-$ . The RAL array uses a  $400\text{ fF}$  feedback capacitor for a charge handling capacity of approximately  $1 \times 10^7$  electrons with a noise performance of 400 to 650 electrons depending on the bandwidth selected and a charge conversion of  $26.4\mu\text{V}/100\text{e}^-$ . Both of these arrays have an adequate dynamic

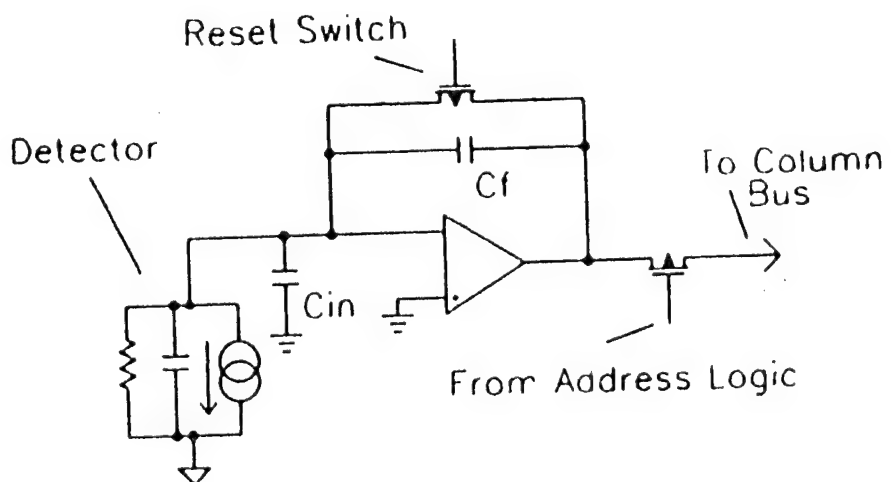
range for a prototype X-ray imager. However, the RAL array probably does not have a large enough charge capacity for photon shot noise limited images, especially at high energies.

Figure 10



Source-follower per detector (SFD) circuit.

Figure 11



Capacitive-feedback transimpedance amplifier (CTIA)

## 6.2 Fabrication Techniques and Size Limitations

The most obvious solid-state X-ray imaging system to consider is to replace the existing film unit with a two-dimensional CdZnTe array and readout electronics to generate a digital X-ray image. This approach makes use of all existing X-ray equipment with a corresponding decrease in the X-ray source intensity to make use of the high efficiency of the CdZnTe. There are however many problems with this approach. An existing diagnostic chest or orthopedic X-ray makes use of a 300 mm x 450 mm film. The 100 mm diameter CdZnTe material available will realistically produce arrays that are 75 mm on a side. This will require placing 24 of the individual 75 mm arrays in a 4 x 6 tiled grid. The photolithographic techniques are readily available today to make tiled detector arrays this size, however the cost of the detector material, at present, would be prohibitive.

Another problem with the tiled area approach is the ability to make the readout arrays. In order to design a CTIA circuit with additional processing functions such as CDS in a 50-100  $\mu\text{m}$  square unit cell requires using high density processes. Industry standard high density processes below 1.2  $\mu\text{m}$  all use step and repeat photolithography with small field of view optics to achieve the desired geometries. This limits the maximum readout die size to approximately 25 mm x 25 mm. It is not feasible with conventional flip-chip hybridization bonding to mate nine 25  $\mu\text{m}$  x 25  $\mu\text{m}$  readout arrays in a 3 x 3 tiled grid to a single 75 mm x 75 mm detector. In addition, the peripheral circuitry such as the multiplexer and output buffers take up space beyond the edge of the unit cell array such that the 4-sided butting that would be required is also not possible. Recent advances in stacked technologies where the peripheral readout circuitry is folded under the readout onto a third chip stacked beneath the readout holds promise in the future. However, this approach still requires development of tiled flip-chip hybridization to build up the larger array. The mechanical assembly requirements for this tiled array system would be prohibitively expensive even if the readout and detector bonding were possible. Use of focused X-ray systems will not improve the prospects for the area system in the near future.

The problem with the area approach can be significantly reduced by incorporating a mechanical scanner into the imaging system. In this approach, a shaped X-ray beam and a linear array of CdZnTe elements are scanned across the imaging area. It is possible to build up a 450 mm linear array with 6 overlapping 75 mm detector arrays. Then the readout size limitation is not as severe. Using 25 mm linear readout arrays in an interdigitated fashion with 9

readout arrays on each side of the detector arrays a full height scanner can be assembled by wire bonding from each pixel to the input pad on the readout array. Figure 3 is an example of this approach taken from the Reticon data sheet for the MB series of arrays. The Reticon array is especially suited for this application since they make their array in a left and right side pad configuration. For a 50 $\mu$ m pixel, the 256 channel linear array will be suitable and for a 100 $\mu$ m pixel, the 128 channel linear array can be used. While the wire bonding approach is very labor intensive, new techniques for interconnecting the detector and readout based on multi-chip module technology may provide a more direct interconnect strategy that is less labor intensive with a corresponding decrease in cost for a fieldable system. Further reductions in the size of the arrays required can be achieved with a focused X-ray system to obtain the desired X-ray coverage. This will produce a tradeoff between the increased cost of the focused system and the decreased cost of the smaller arrays.

### 6.3 Environmental Constraints

The environmental constraints are primarily concerned with the effects of the X-rays themselves on the readout electronics. In all cases that were considered the readout electronics are in close proximity to the CdZnTe detector array and thus are subject to effects of the X-rays. While mechanical shielding of the all other parts of the system other than the detector is the obvious solution there may be production cost implications and no guarantee that residual X-rays may not still affect the readout due to the close proximity of the readout to the detector. For these reasons the readout electronics should have a degree of radiation hardness built-in to insure no degraded performance. As the bulk of the readout technology had its beginnings with military IR imagers, radiation hardness was addressed in those applications. A combination of X-ray shielding of the components and radiation hardness of the array themselves through the fabrication process will be needed for the fieldable version of the X-ray imager.

### 6.4 Summary

Readout technology can support a scanning or focused scanning X-ray imaging system. A prototype imager can be designed and assembled now by utilizing commercially available readouts. Future foldable production systems will require an optimized readout design to achieve a balance between the noise and dynamic range and the addition of any other on-chip signal processing functions.

## 7. Application Examples

### 7.1 Scanned system

Linear scanned arrays are used in some existing medical radiography equipment. Assume an array is to be designed for a scanned system using a Reticon MB series multiplexer readout. The specifications for this commercial circuit are found in the data sheet in appendix B. The following requirements are assumed:

1. Spatial resolution: 10 lpm
2. DQE:  $\geq 90\%$
3. Tube voltage: 100 KVP
4. Radiation dose:  $5 \times 10^9$  photons/cm<sup>2</sup>
5. Scan speed: 2 inches/second

#### Pixel size

To resolve 10 lpm, 20 pixels per millimeter are required, i. e. 50 microns per pixel.

#### Integration time

From the data sheet, the well capacity for the specified readout is 80 pC =  $5 \times 10^8$  electrons. The calculation below of the integrated signal current shows that two reads per pixel position are required:

$$\begin{aligned} \text{Photons per pixel in image} &= 5 \times 10^9/\text{cm}^2 \times (50 \text{ microns}/10^4 \text{ microns/cm})^2 \\ &= 1.25 \times 10^5 \end{aligned}$$

$$\text{Approx. average photon energy} = 75 \text{ keV}$$

$$\begin{aligned} \text{Electrons generated per photon} &= 75,000/5 \\ &= 15,000 \text{ electrons/photon} \end{aligned}$$

$$\text{Electrons collected } (\eta = 0.5) = 9.3 \times 10^8 \text{ electrons/pixel}$$

$$\text{Well Size/Signal} = 1.9$$

The scan speed requires 1016 pixels to be integrated per second. Since two reads are required per pixel position, the integration interval will be 0.5 ms. This means the quantum statistics of the system will be based on a maximum number of photons detected per read cycle of

$$\begin{aligned} N_{\max} &= 1/2(1.25 \times 10^5) \\ &= 6.25 \times 10^4 \text{ photons} \end{aligned}$$

#### CdZnTe thickness.

From the linear absorption coefficient plot it is seen that  $\alpha(75\text{keV})$  is  $20/\text{cm}$ . The array thickness is determined from required DQE of 0.9, assuming<sup>3</sup>

$$\text{DQE} = 1 - \exp(-\alpha d)$$

The required thickness is thus 0.11 cm.

#### Minimum operating voltage

Applying the analysis of the previous section, the voltage required for 50% collection efficiency is 17 V.

#### Leakage current

From the curves calculated in Section 0, assuming the array is fabricated from the 10% alloy and operated at room-temperature, the leakage current density at the minimum voltage is  $1.5 \times 10^{-8} \text{ A/cm}^2$

$$= 4.0 \times 10^{-13} \text{ A/pixel}$$

<sup>3</sup> The Physics of Medical X-Ray Imaging, 2nd Edition, B. H. Hasegawa, Medical Physics Publishing Co., Madison, WI (1991).

$$\begin{aligned}
 &= 2.3 \times 10^6 \text{ electrons/s} \\
 &= 1150 \text{ electrons/integration interval}
 \end{aligned}$$

### Signal Current

At the specified x-ray flux, it was calculated above that the electrons collected per pixel will be  $9.4 \times 10^8$ . Half this number will be collected per 0.5 ms integration interval:

$$= 4.7 \times 10^8 \text{ electrons/integration interval}$$

### Signal to Noise

The readout noise quoted on the manufacturer's data sheet in Appendix B is 1500 electrons, and the total integrated leakage current is 1150 electrons. The sum of these is equivalent to a small fraction of one photon, therefore Poisson quantum statistics on the number of photons detected in a read cycle,  $N$ , overwhelmingly dominates other noise sources in this system. The maximum SNR can therefore be taken to be

$$\begin{aligned}
 \text{SNR} &= N_{\max}^{1/2} \\
 &= 2.5 \times 10^2
 \end{aligned}$$

### Dynamic Range

A criterion for minimum signal level required to detect *contrast* in the image is that the mean intensity  $N_{\min}$  be greater than two standard deviations of the mean  $2\sigma = 2N_{\min}^{1/2}$ .

$$\begin{aligned}
 N_{\min} &= 2N_{\min}^{1/2} \\
 N_{\min} &= 4.
 \end{aligned}$$

That is, it is assumed at 4 counts per pixel = 160,000 counts per  $\text{cm}^2$  visible contrast will be discernible in a clinical image. The dynamic range for this system can therefore be estimated as

$$(N_{\max})/(N_{\min}) = 1.6 \times 10^4$$

which is a two order of magnitude improvement over film-screen systems.

In this example the dark current calculated is insignificant, meaning the array performance will be relatively insensitive to variations in temperature or bias voltage. An example follows of a system which is dark current limited.

## 7.2 Focused system

A practical, field-portable focused x-ray imager can be developed for trauma care. Such an instrument could be based on the system described recently in the paper included as Appendix C of this report. The appended paper from the Journal of Electrocardiology describes a novel x-ray imager based on a focusing collimator which is currently under development for surgical fluoroscopy by Cardiac Mariners in Los Gatos, California. The present design employs a single, one inch diameter scintillator/PSPMT combination detector having pixels limited to pitch greater than 1 mm, resulting in spatial resolution of 2 lpm. A sub-millimeter CdZnTe pixel array would easily double the spatial resolving power of the current design imager to 4 lpm, which is the current standard for general use fluoroscopy systems. Higher resolution is achievable with new collimator designs.

Assume Cardiac Mariners has approached Digirad to assess the viability of using  $Cd_{1-x}Zn_xTe$  detector arrays in such a focusing system for general radiography, using the an ASIC readout with the characteristics of the Reticon MUX of Appendix B. Requirements are:

1. Pixel size: 0.75 mm
2. DQE: > 90%
3. Tube Voltage: 100 KVP
4. Radiation dose:  $5 \times 10^9$  photons/cm<sup>2</sup>
5. Number of Collimator holes:  $10^4$
6. Number of pixels: 64 x 64
7. Scan time: 5 seconds
8. Scanned area: 8" x 8"

Requirements 2 - 4 are the same as those of the previous example, so the well size, thickness, bias voltage and leakage current density are all the same.

### Integration time

For this system the maximum integration time is determined by the scan time and number of collimator positions:  $5 \text{ s} / 10^4 = 0.5 \text{ ms}$ .

### Leakage current

The larger pixels will result in increased leakage current.

$$\begin{aligned} &= (1.5 \times 10^{-8} \text{ A/cm}^2) \times (0.075 \text{ cm})^2 \\ &= 8 \times 10^{-11} \text{ A/pixel} \\ &= 5.3 \times 10^8 \text{ electrons/s} \\ &= 2.5 \times 10^5 \text{ electrons/ integration interval} \end{aligned}$$

### Signal current

The scanned area is  $413 \text{ cm}^2$ , having a total dose of  $2 \times 10^{12}$  photons, distributed among  $10^4$  pencil beams from the collimator. The beams are further distributed among the  $64 \times 64$  pixels on the detector array, resulting in

$$\begin{aligned} N_{\max} &= 5 \times 10^4 \text{ photons/pixel} \\ &= 7.5 \times 10^8 \text{ electrons generated / pixel} \\ &= 3.8 \times 10^8 \text{ electrons collected / pixel } (\eta=0.5) \end{aligned}$$

### Signal to Noise

In this system the integrated dark current is equivalent to about 33 x-ray photons. This is still small in comparison to the variance of the maximum signal level, thus

$$\begin{aligned} \text{SNR} &= N_{\max}^{1/2} \\ &= 224 \end{aligned}$$

### Dynamic Range

The minimum detectable contrast in this system will result for photon flux exceeding the photon equivalent of  $2\sigma$  for the integrated dark current,  $N_{\min} \sim 12$

$$(N_{\max} / N_{\min}) = 8 \times 10^3$$

which is much higher than film-screen systems, but is dark current limited. Note that since dark current is thermally activated, the performance of this system will be sensitive to temperature. This problem could be addressed by using a higher resistivity alloy, reducing the pixel size or cooling.

## 1. Conclusions

The Phase I goals were achieved. It has been demonstrated that monolithic  $Cd_{1-x}Zn_xTe$  detectors produce direct electronic x-ray images with spatial resolution, signal-to-noise ratio, dynamic range and detective quantum efficiency superior to film-screen combinations currently in use for medical radiography.

For low x-ray energies useful for imaging soft tissue such as the breast, 50  $\mu m$  spatial resolution with virtually 100% detection efficiency was demonstrated, while for higher energy x-rays, where fluorescence dominates the signal spreading, 100 - 200  $\mu m$  spatial resolution was demonstrated. Dynamic range for 50  $\mu m$  pixel arrays is estimated to be two orders of magnitude greater than film-screen systems.

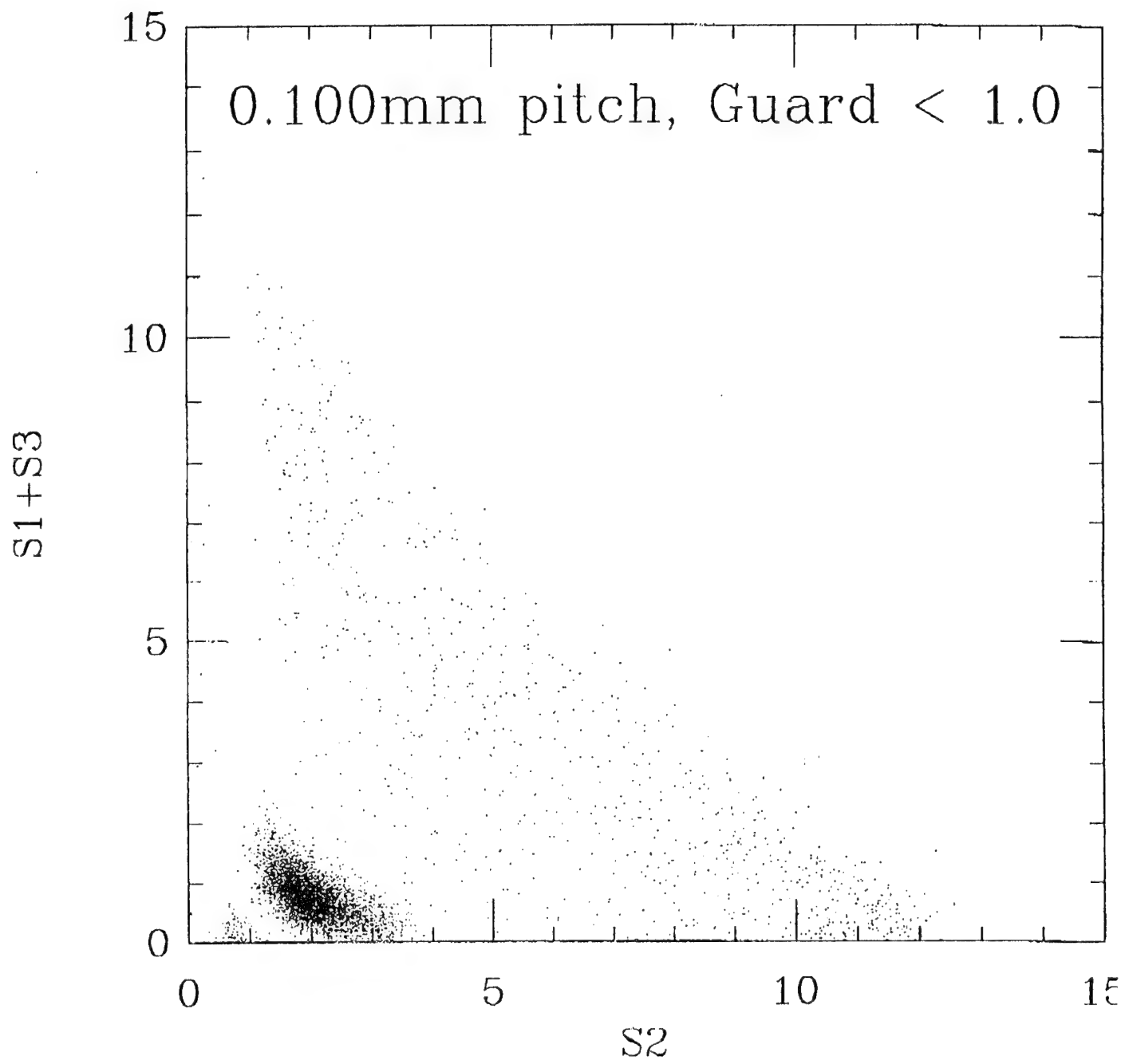
Array processing was shown to be insensitive to variations in material quality. Relatively low quality material was used to produce monolithic array structures with useful characteristics for x-ray imaging. The results obtained with these arrays are representative of those achievable in high volume production.

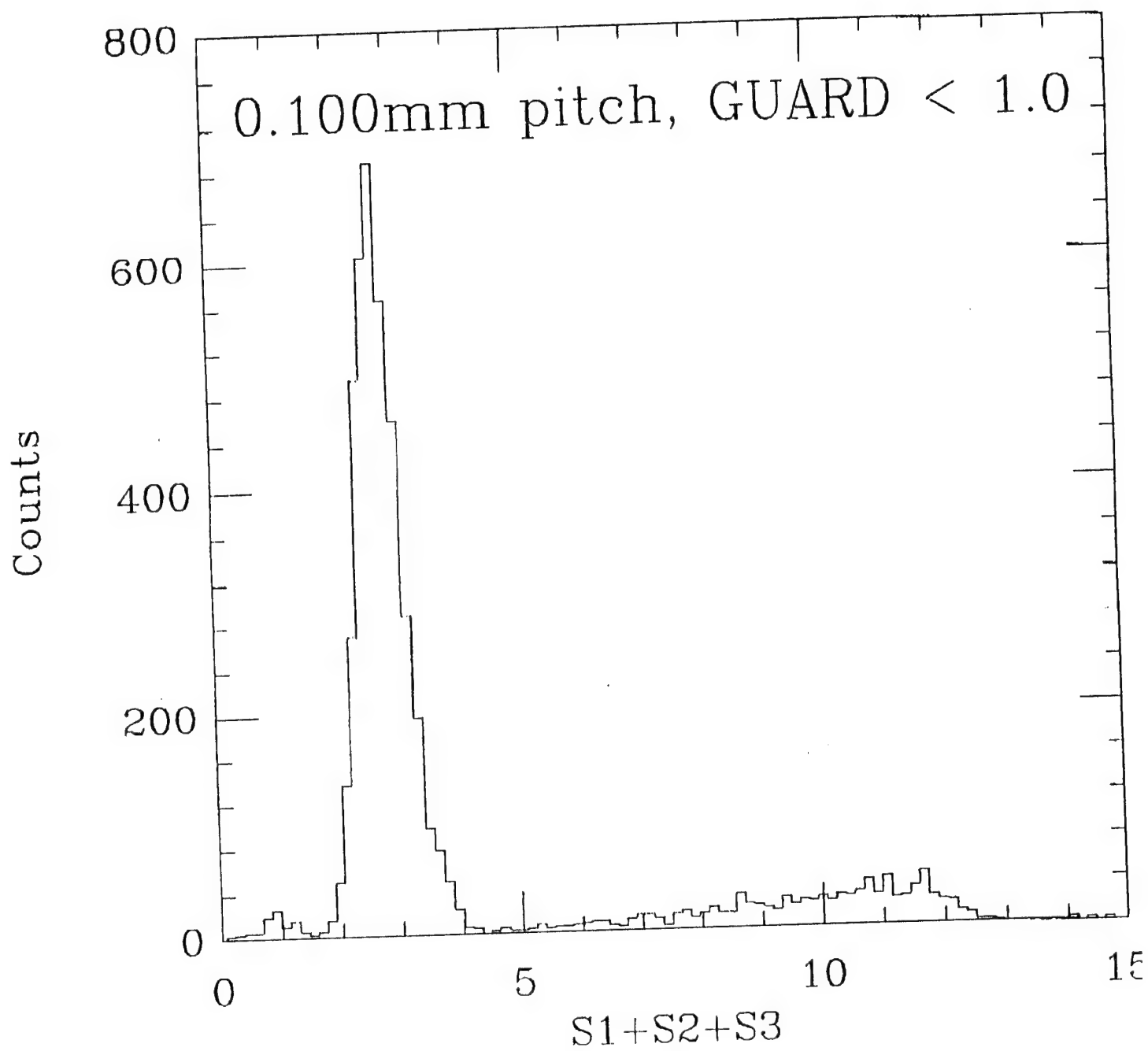
The Phase I data support electron trapping rather than lateral charge diffusion as the chief mechanism for signal spreading within the semiconductor under conditions of low bias. Using results of the multichannel pulse height spectroscopy measurements, a design basis model has been developed for  $Cd_{1-x}Zn_xTe$  imaging arrays for radiography applications.

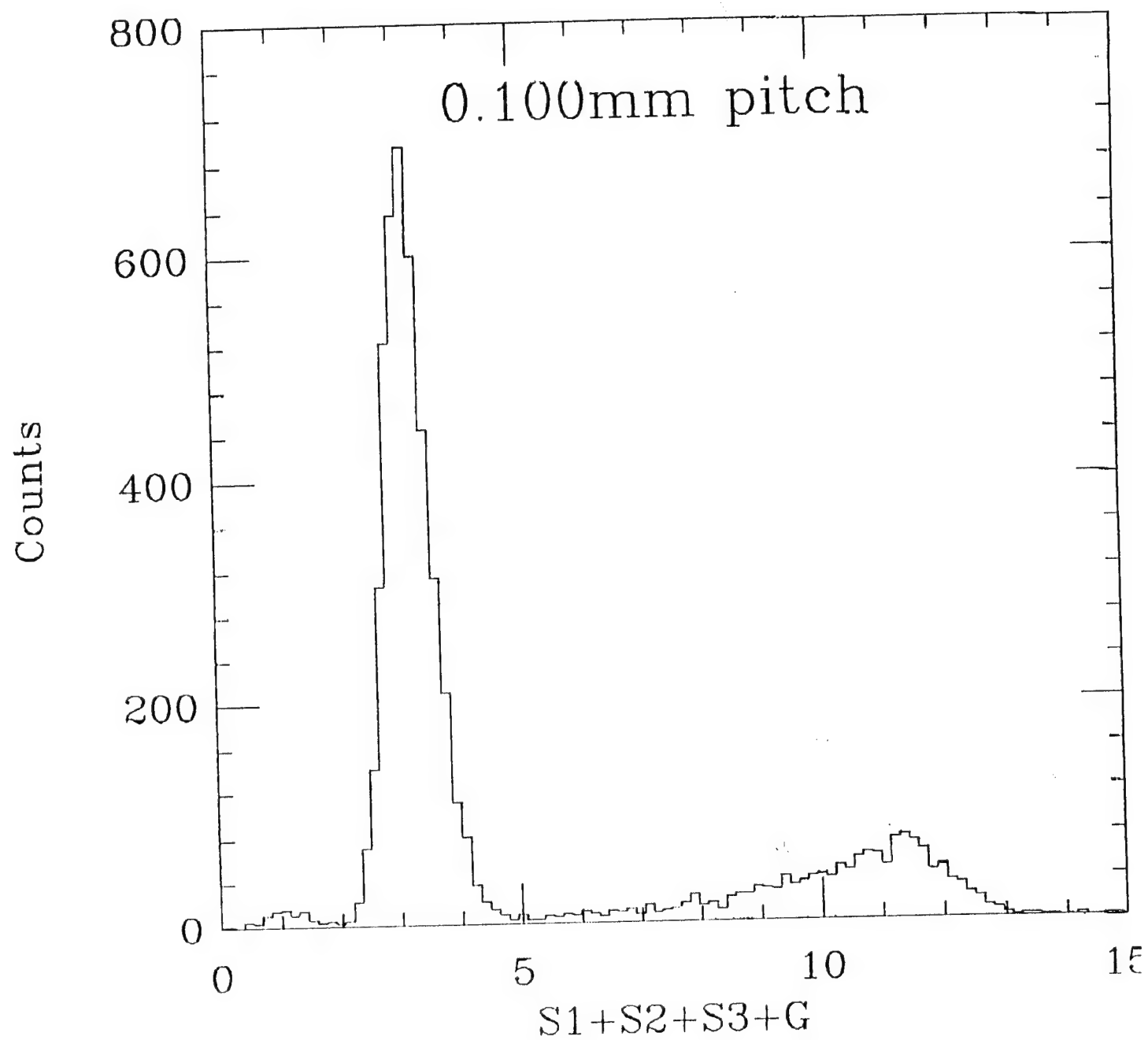
Available readout technologies have been surveyed and, example detectors have been designed for current-mode imaging using a commercial multiplexer readout. The existing technology can support scanning or focusing X-ray imaging systems, similar to currently using scintillation detectors.

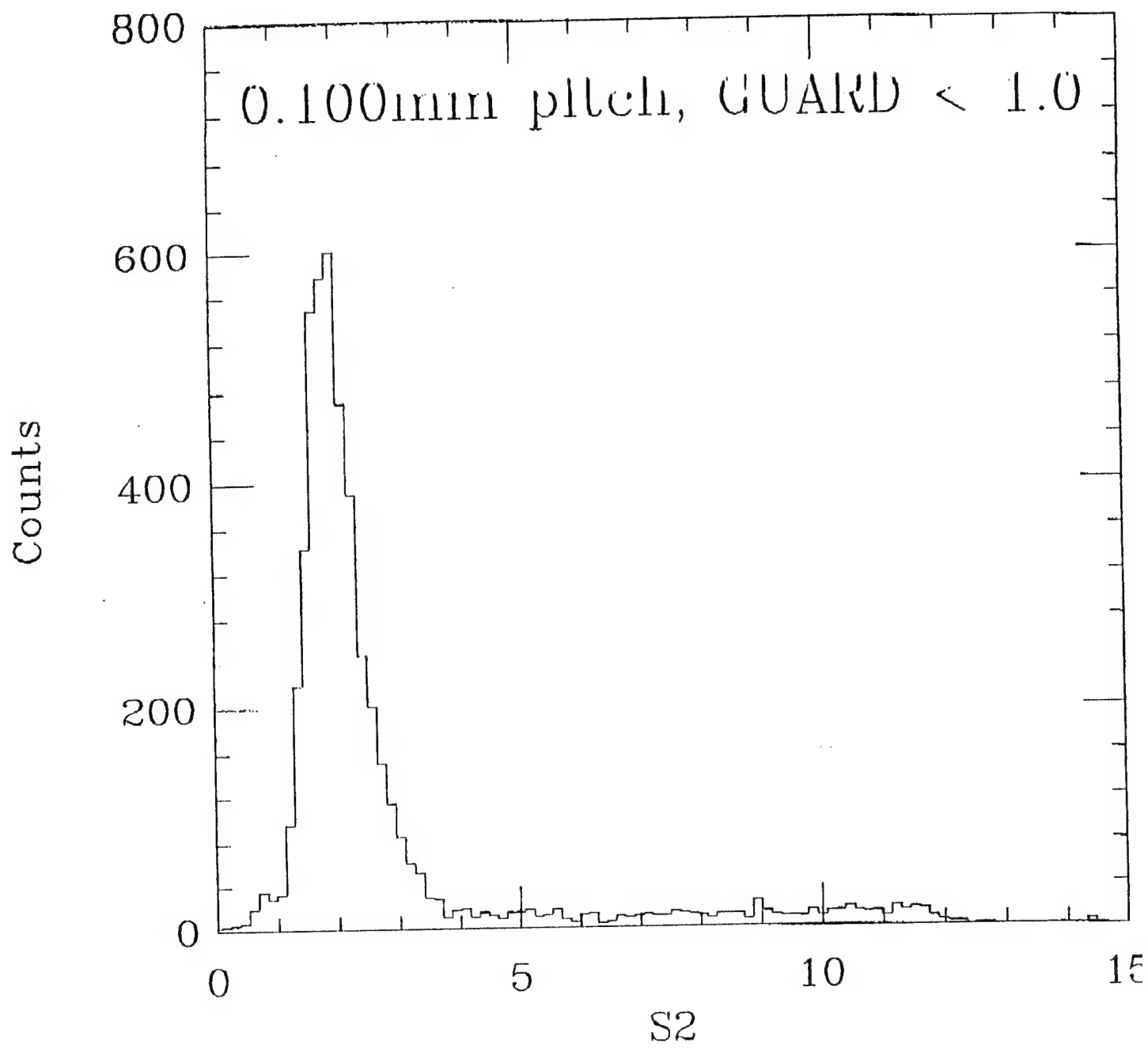
Two potential Phase II system designs were developed, based on challenging but realistic requirements of existing medical radiography equipment. The performance expected from these designs is superior to film-screen and scintillator detectors currently in use for these applications. It is concluded that CZT imagers are presently both technically and economically feasible.

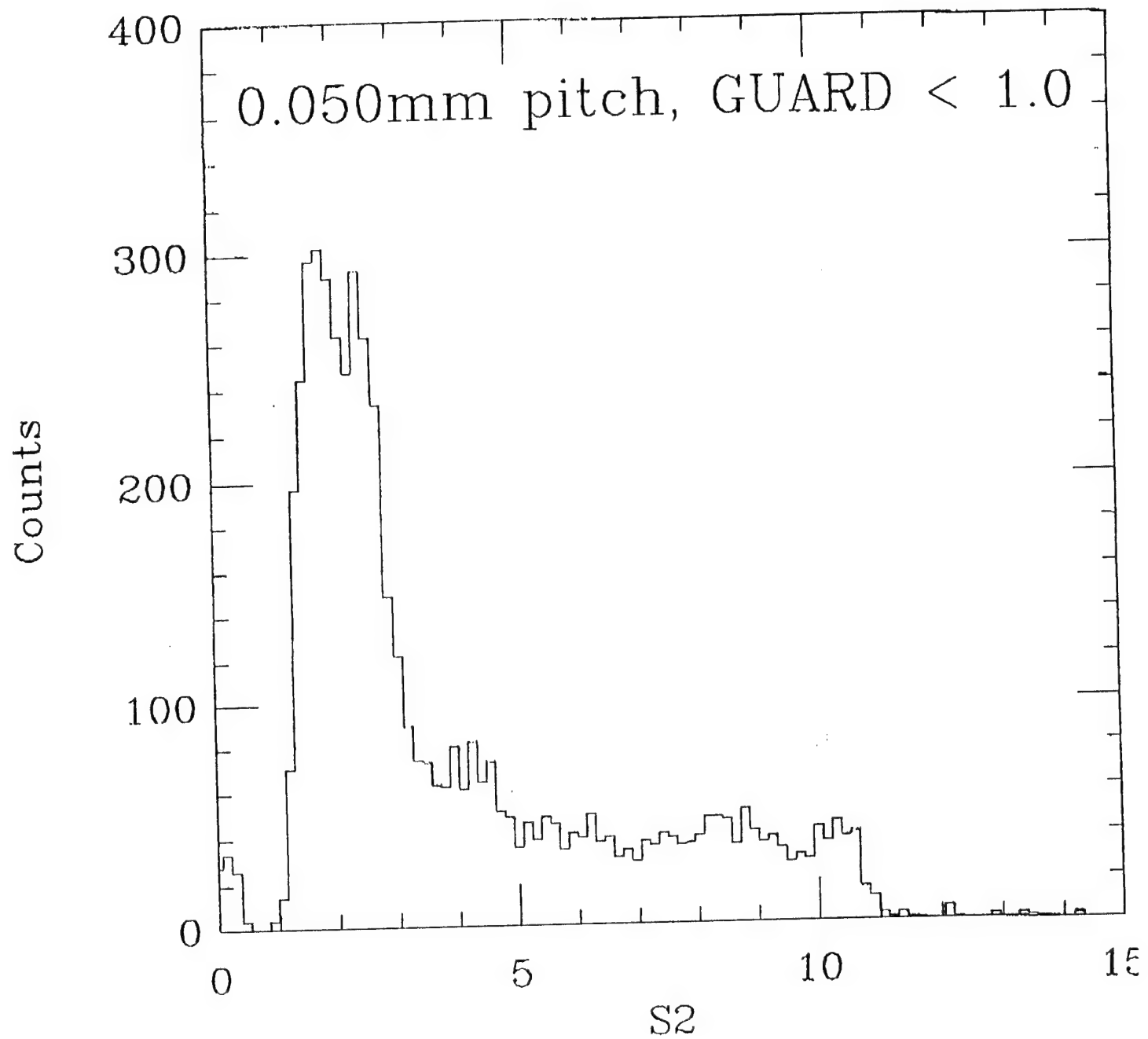
## **9. Appendix A: Raw Data**

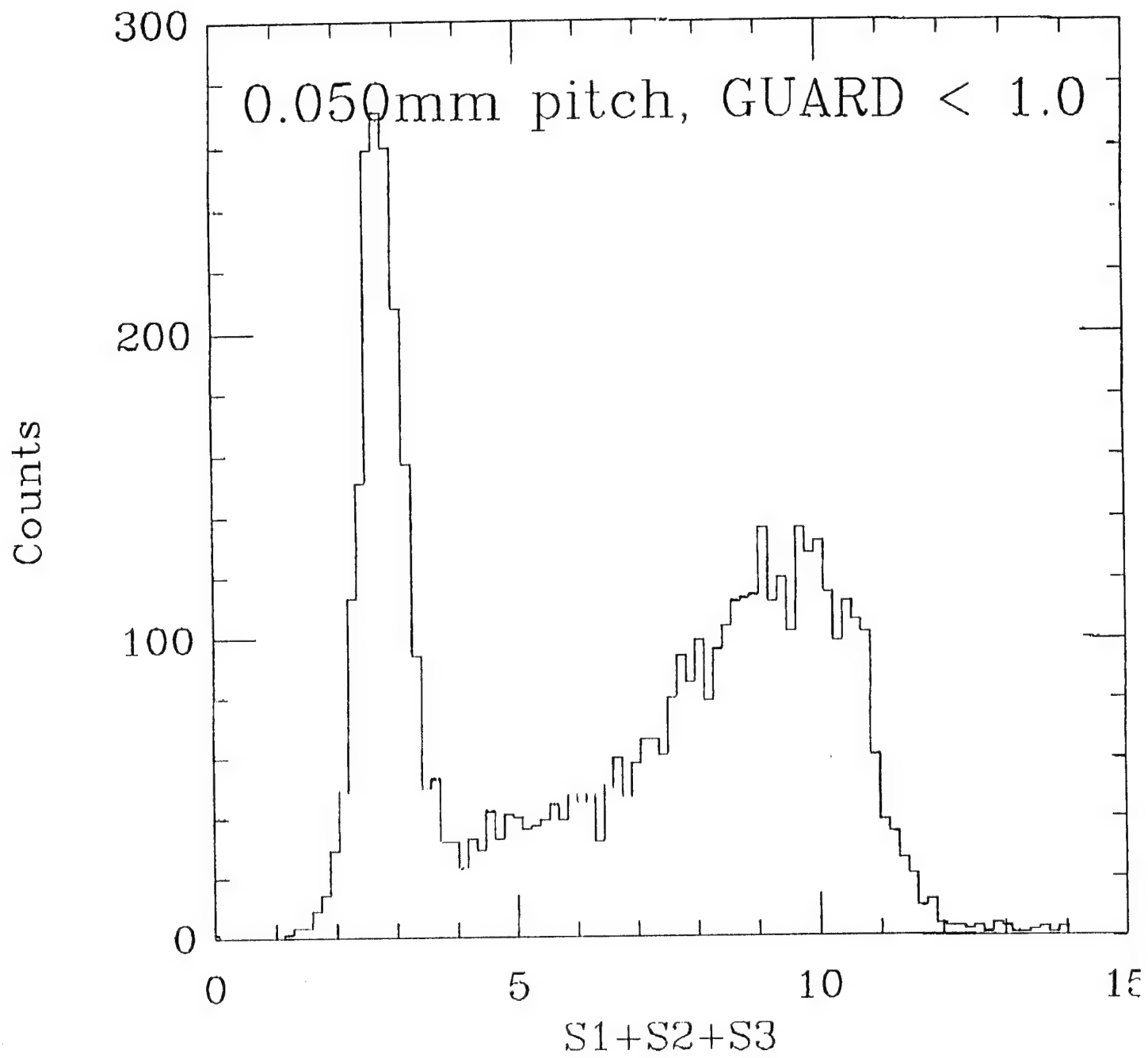


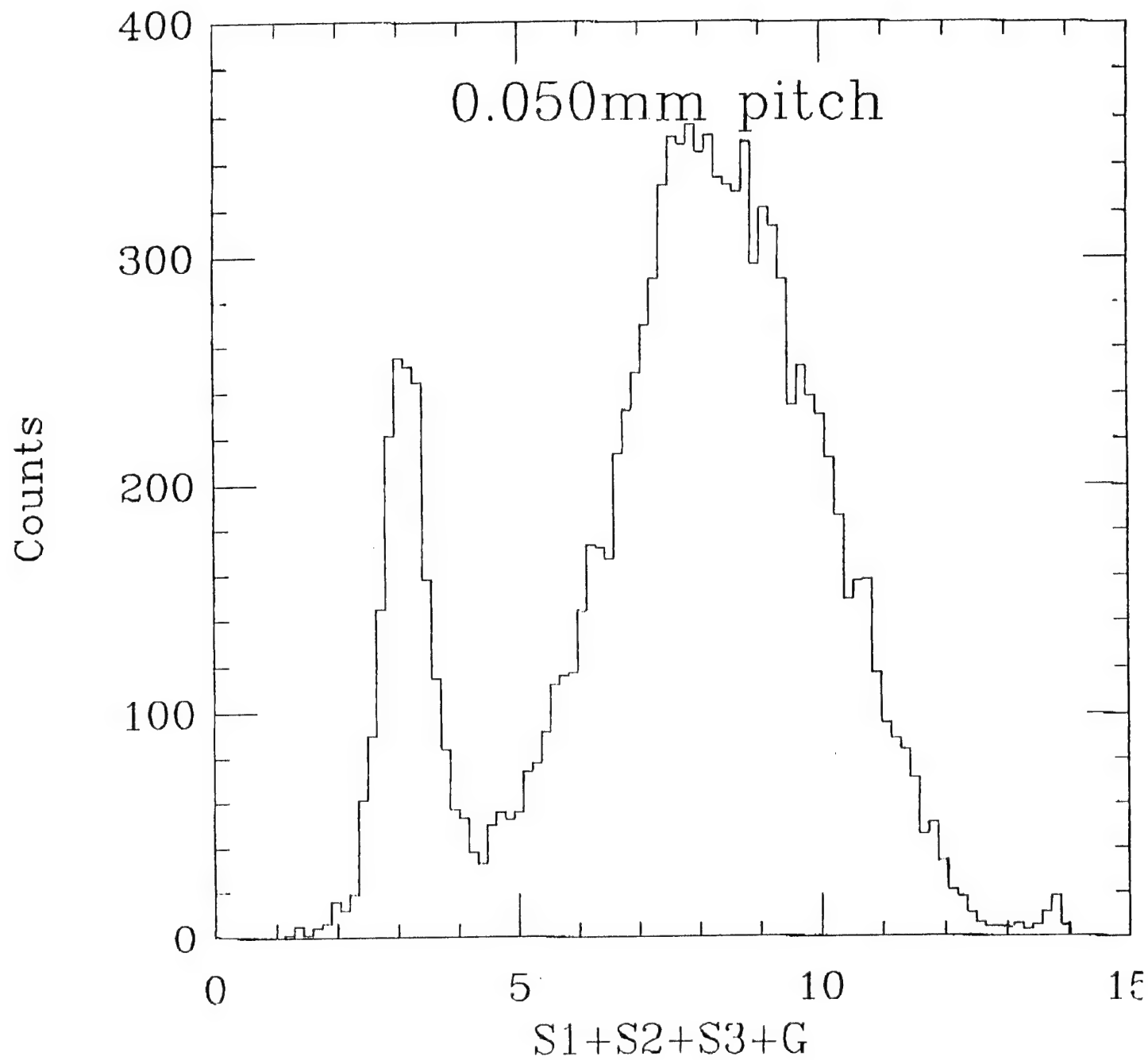


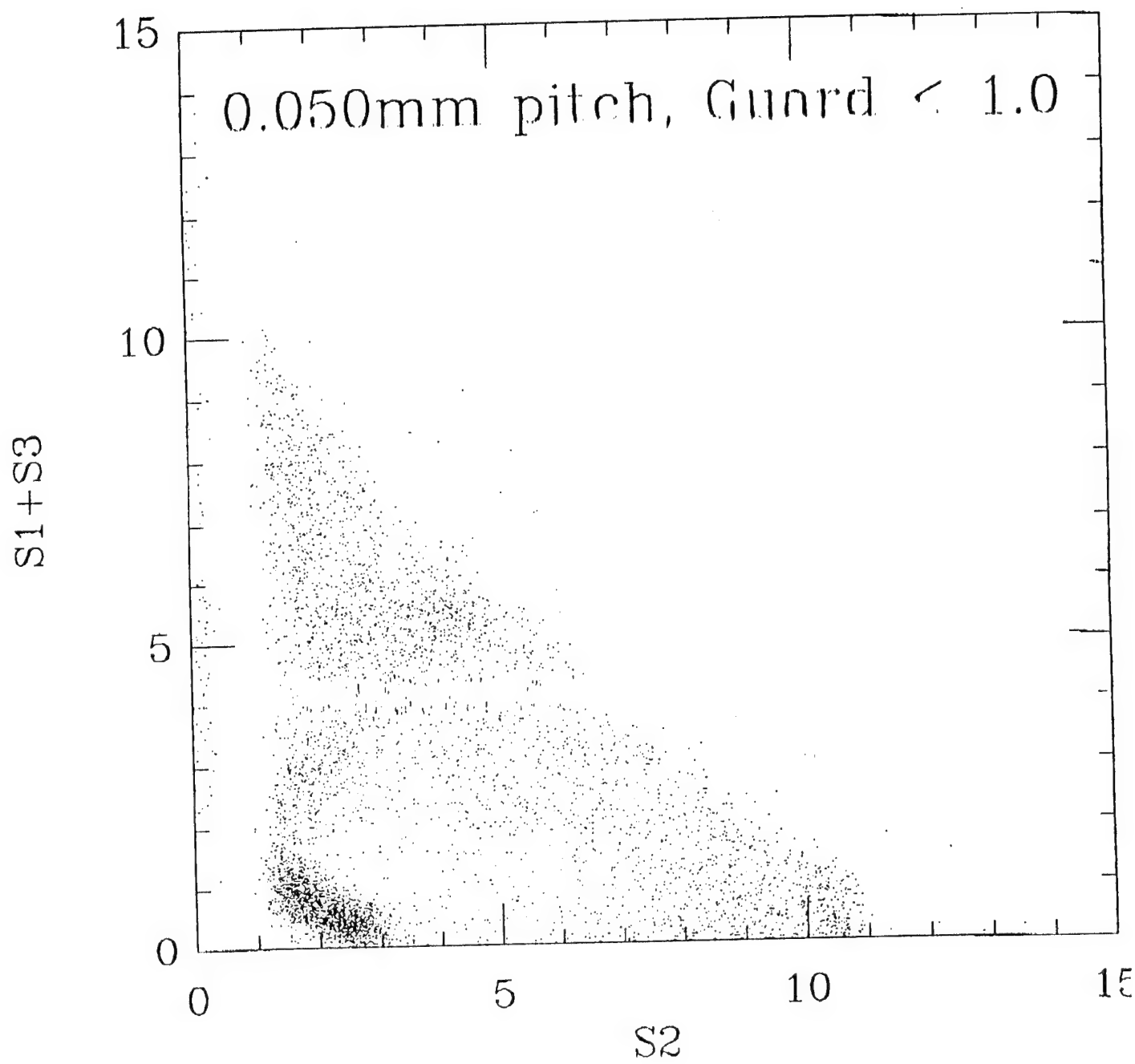






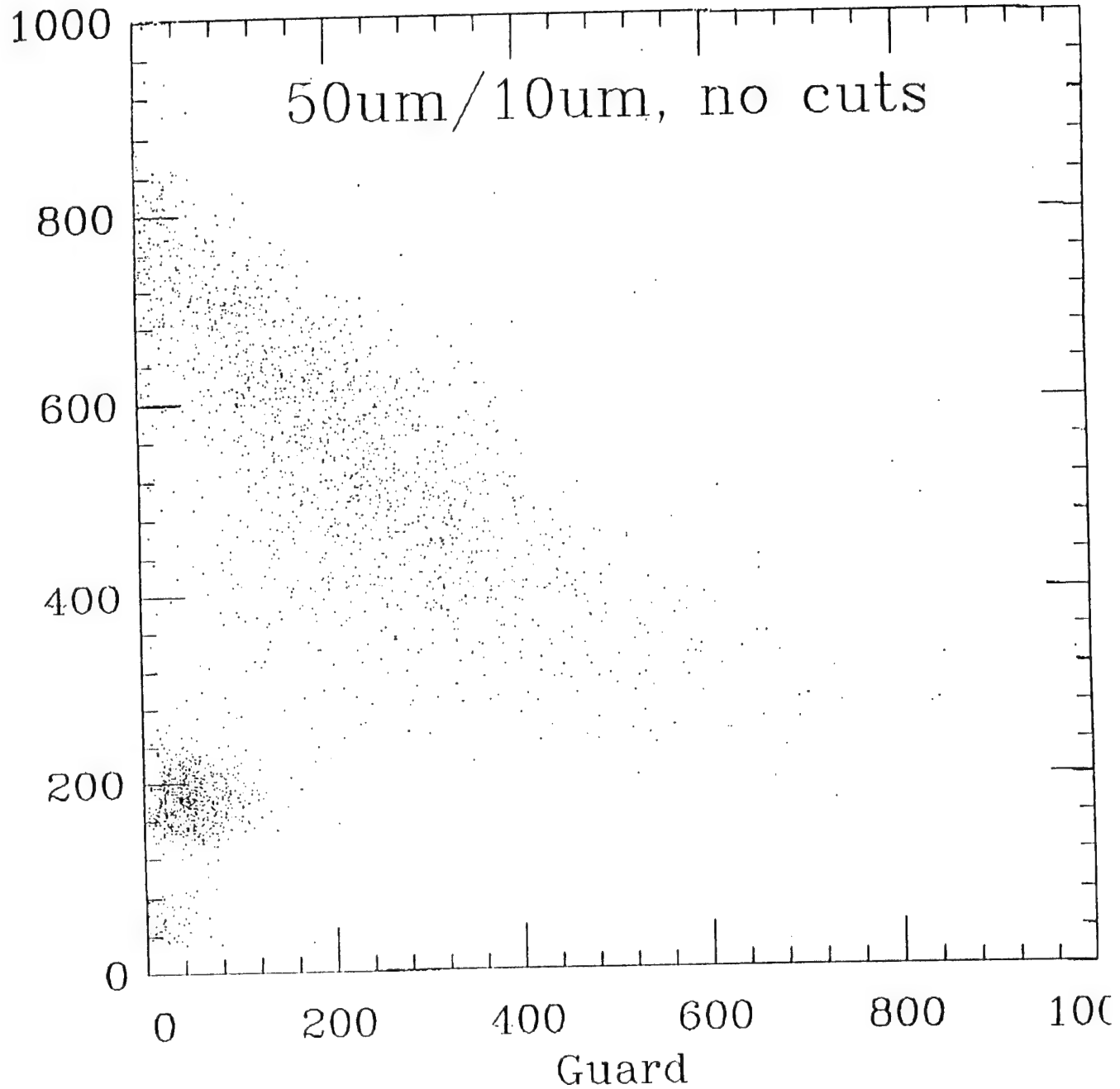


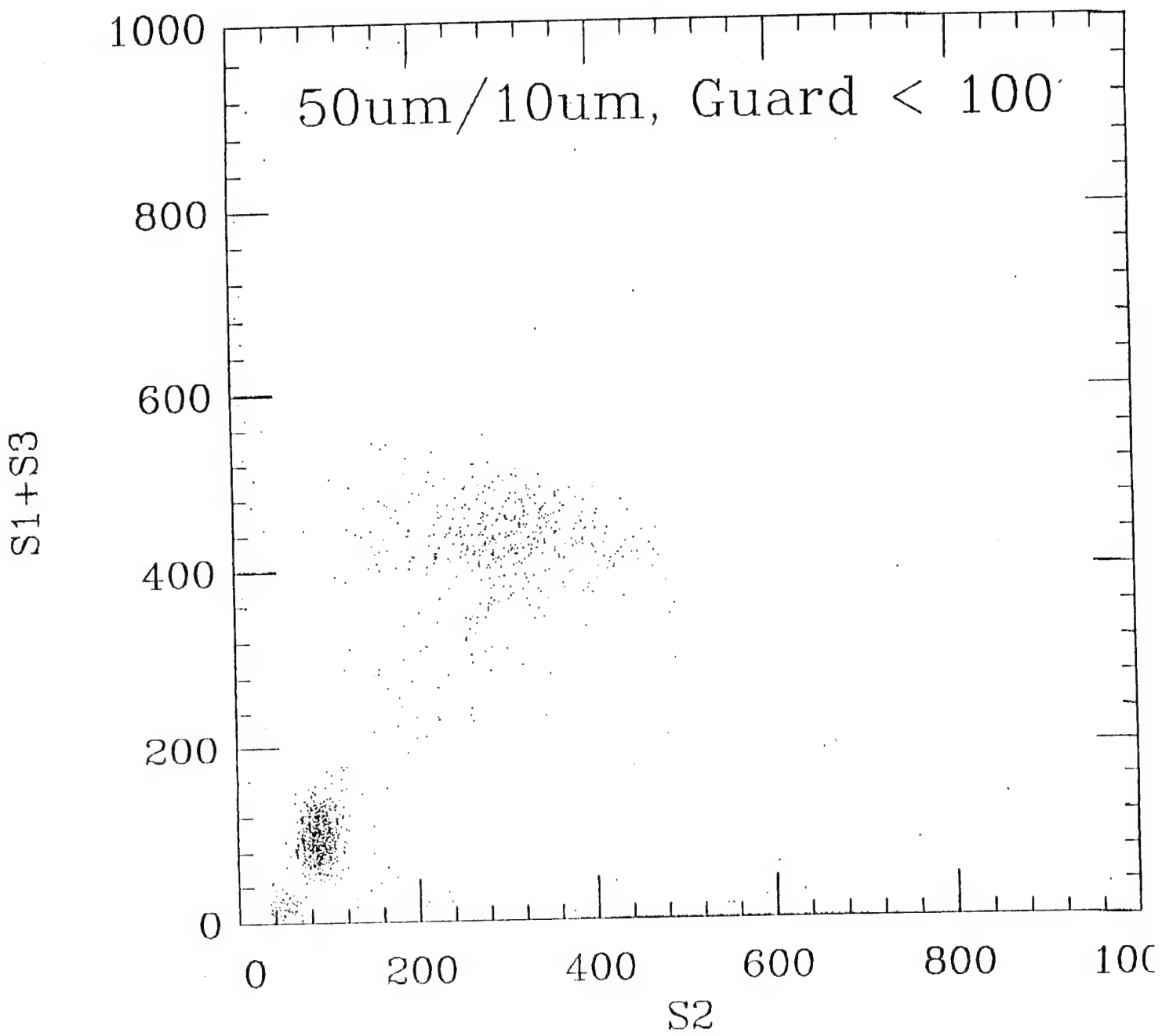


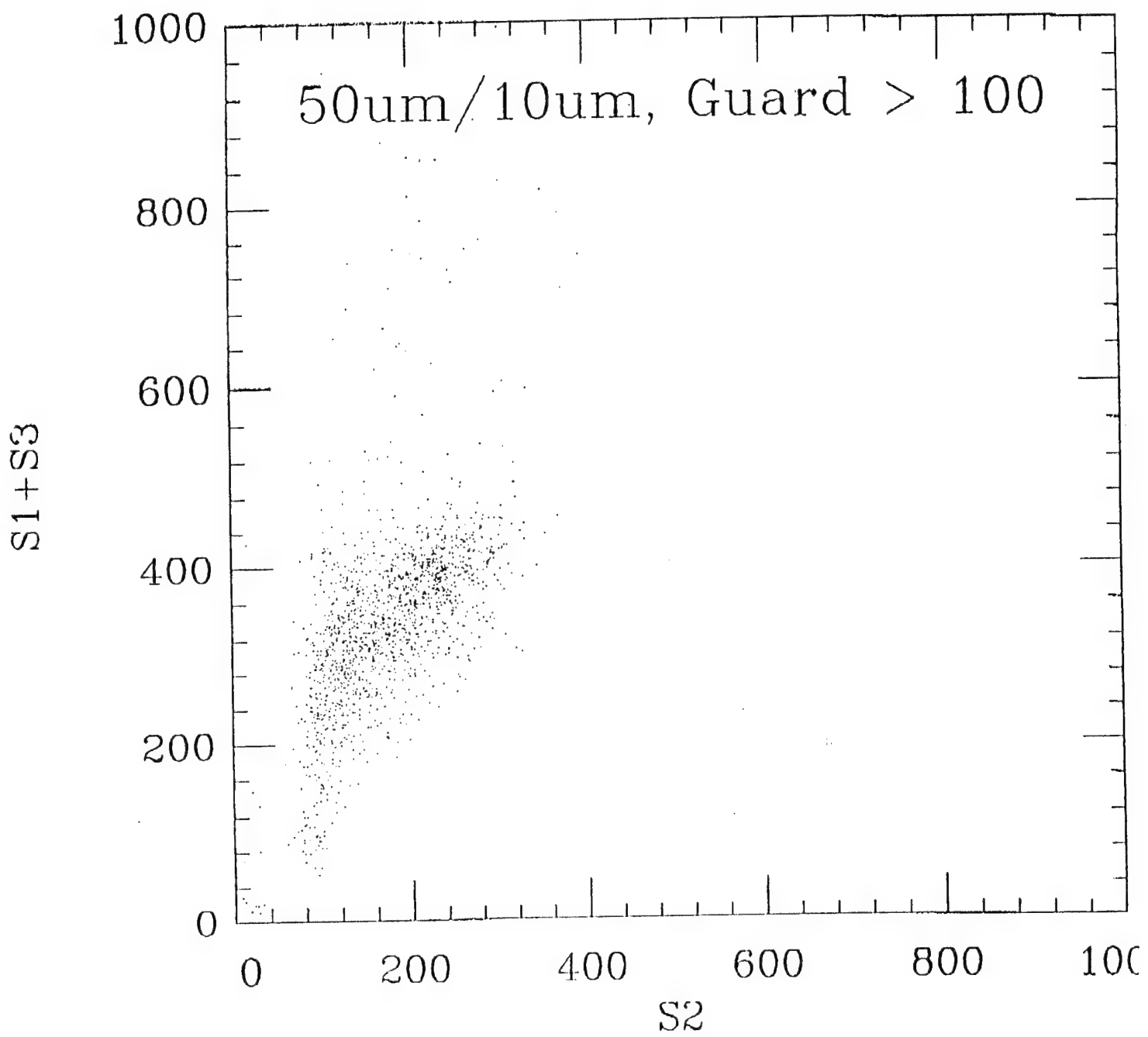


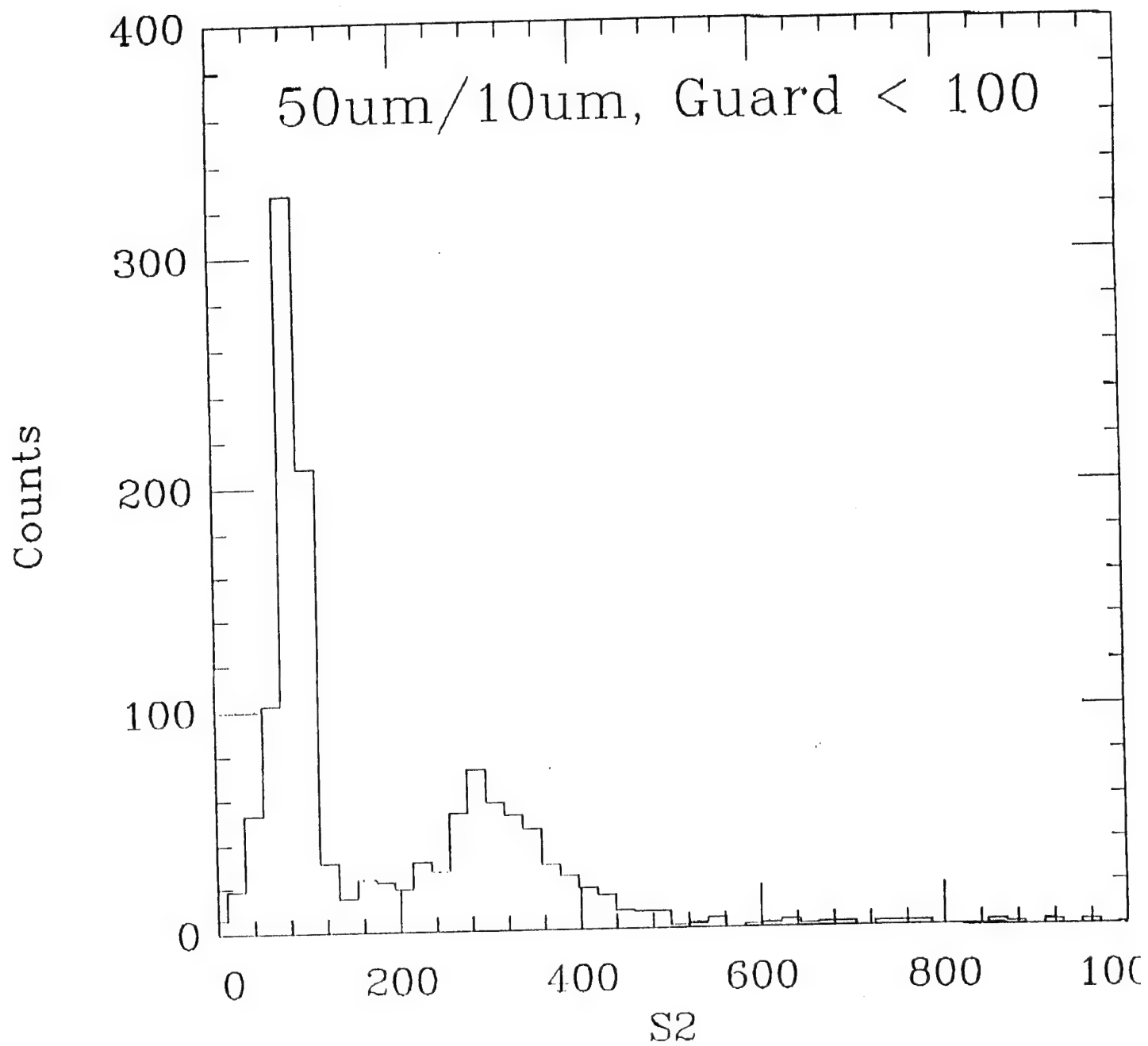
Post-It® Fax Note	7671	Date	# of pages
To	Patrick Doty	From	Paul Highe
Co/Dept.	Digirad	Co.	Wash U
Phone #		Phone	(314)935 7576
Fax #	(619)549-7714	Fax #	

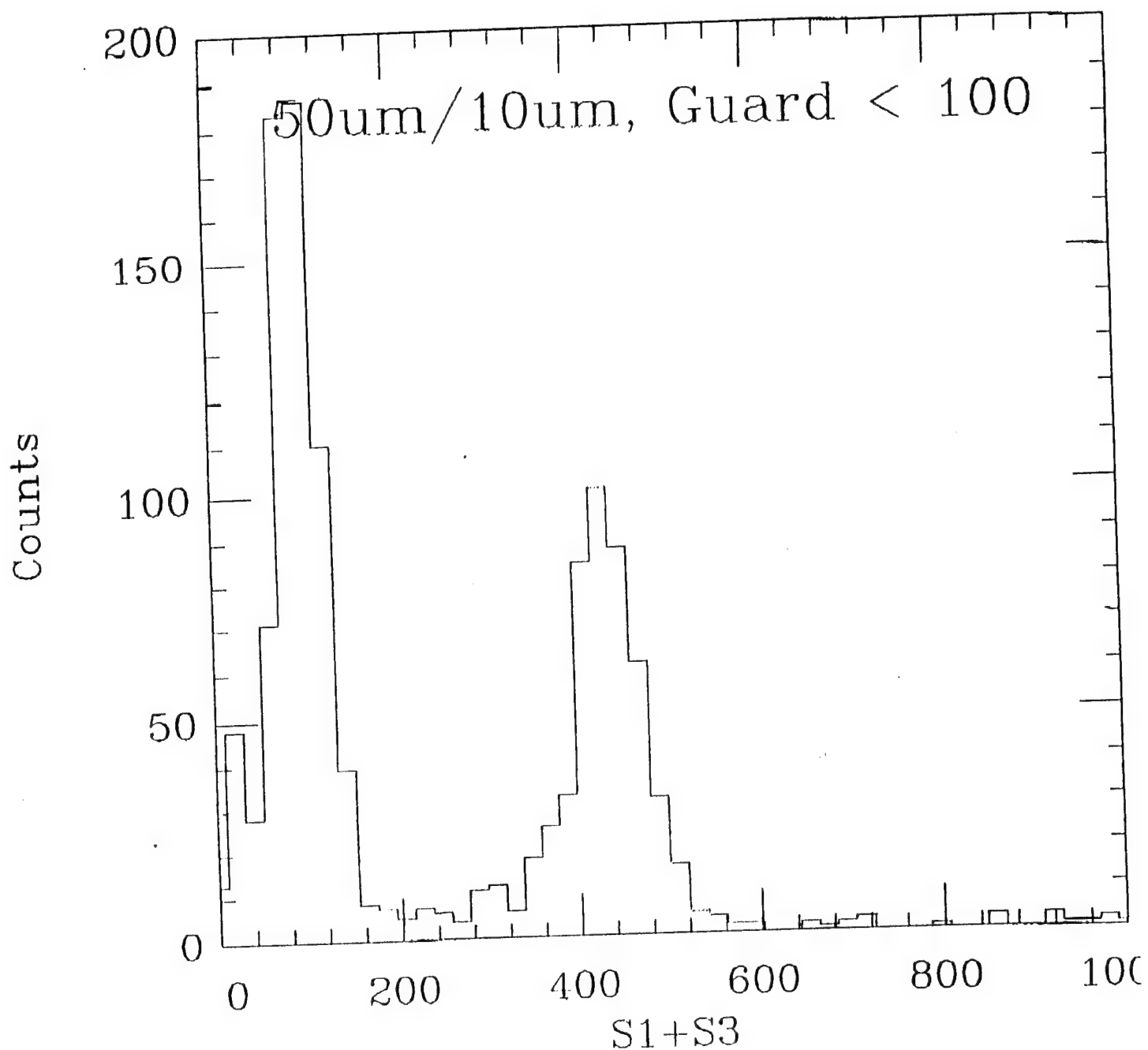
S1 + S2 + S3

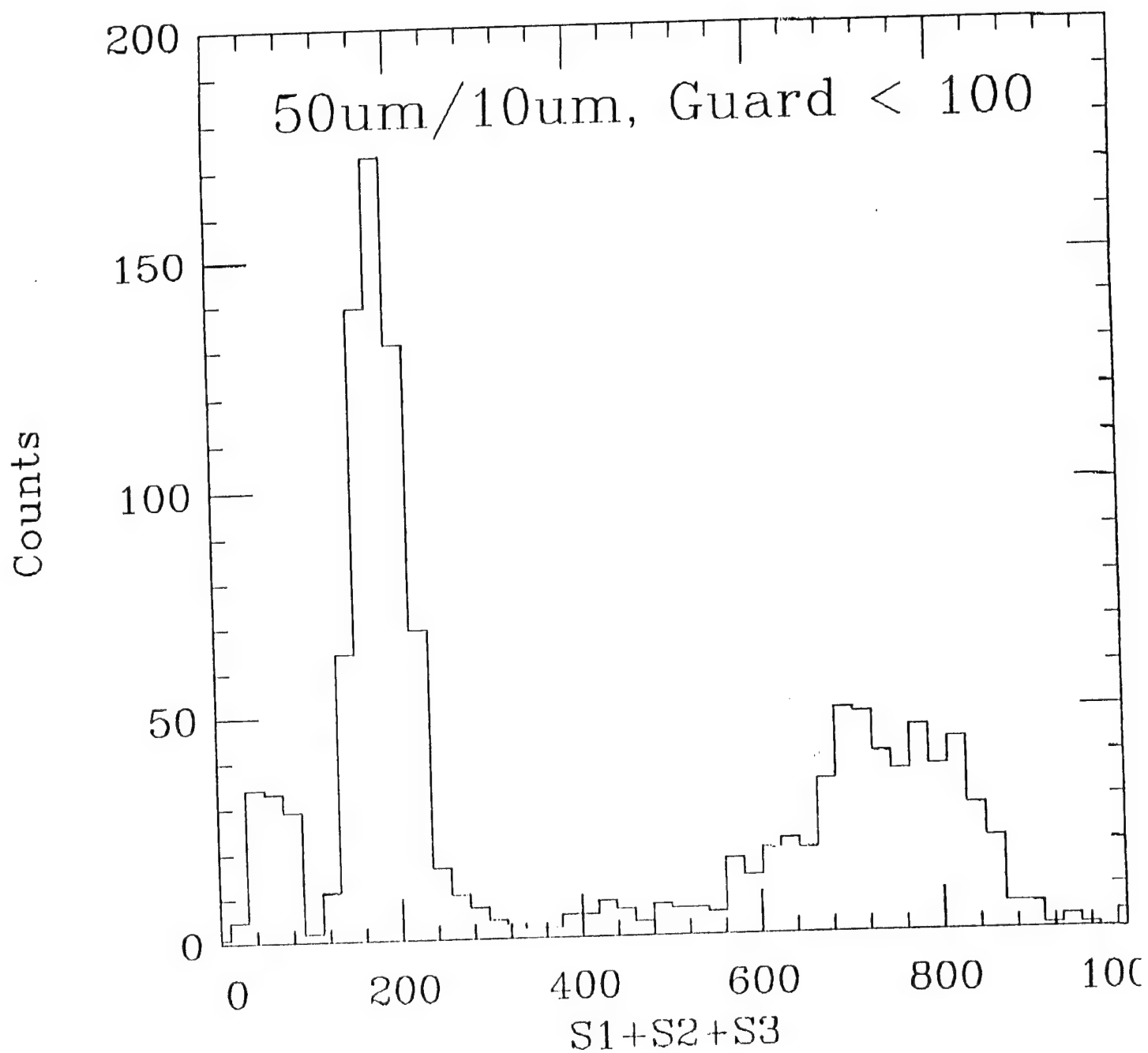




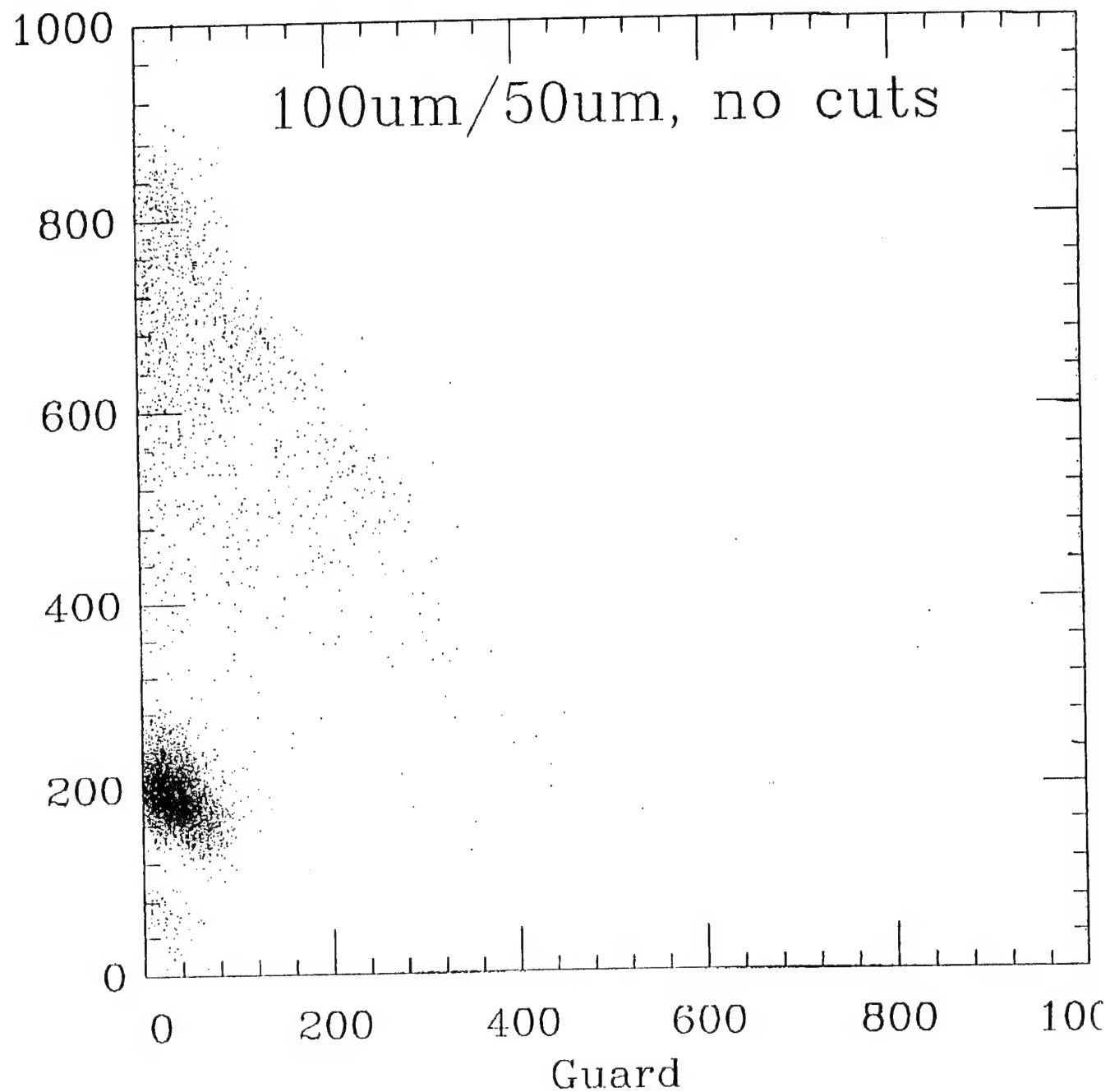




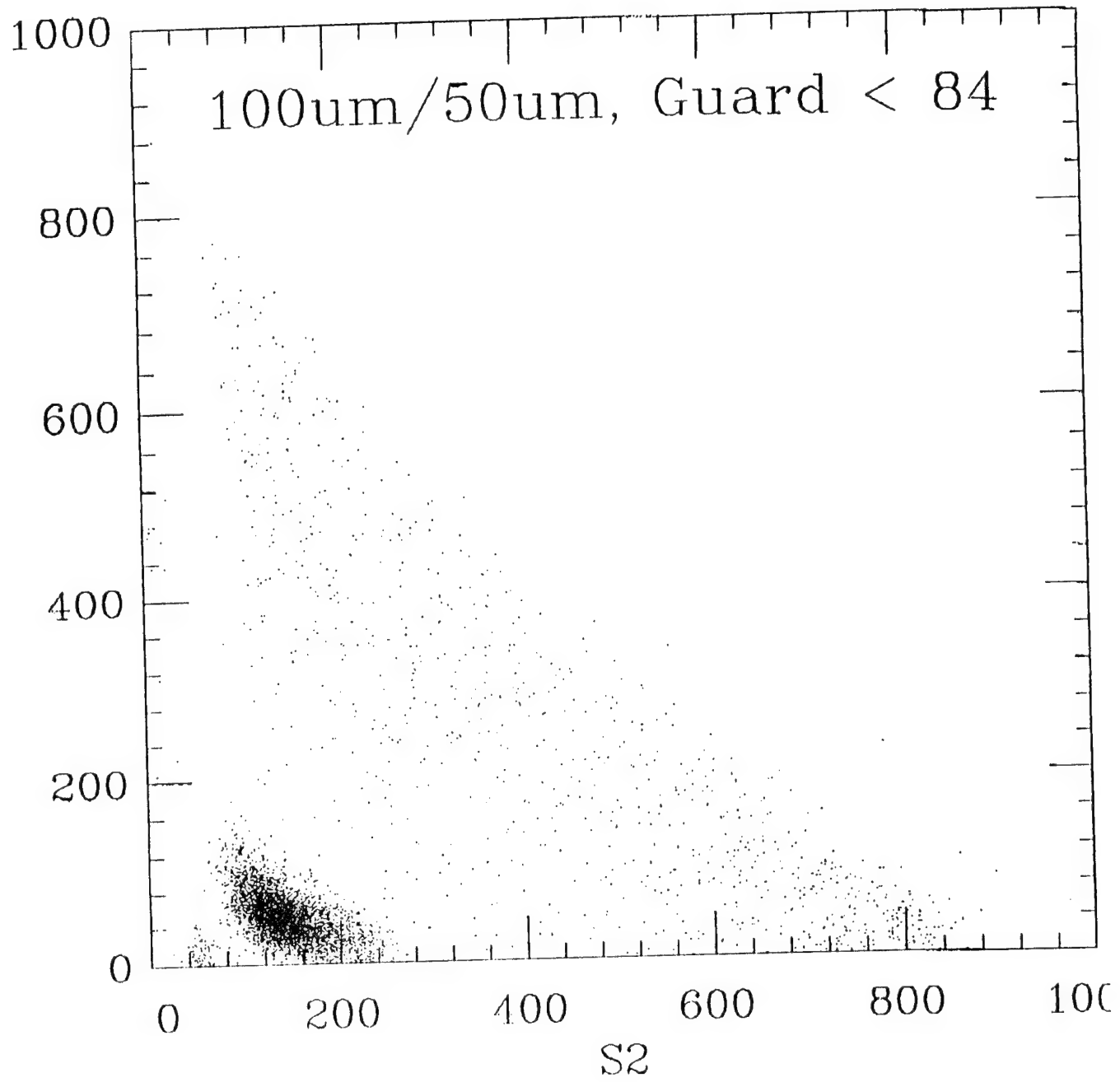




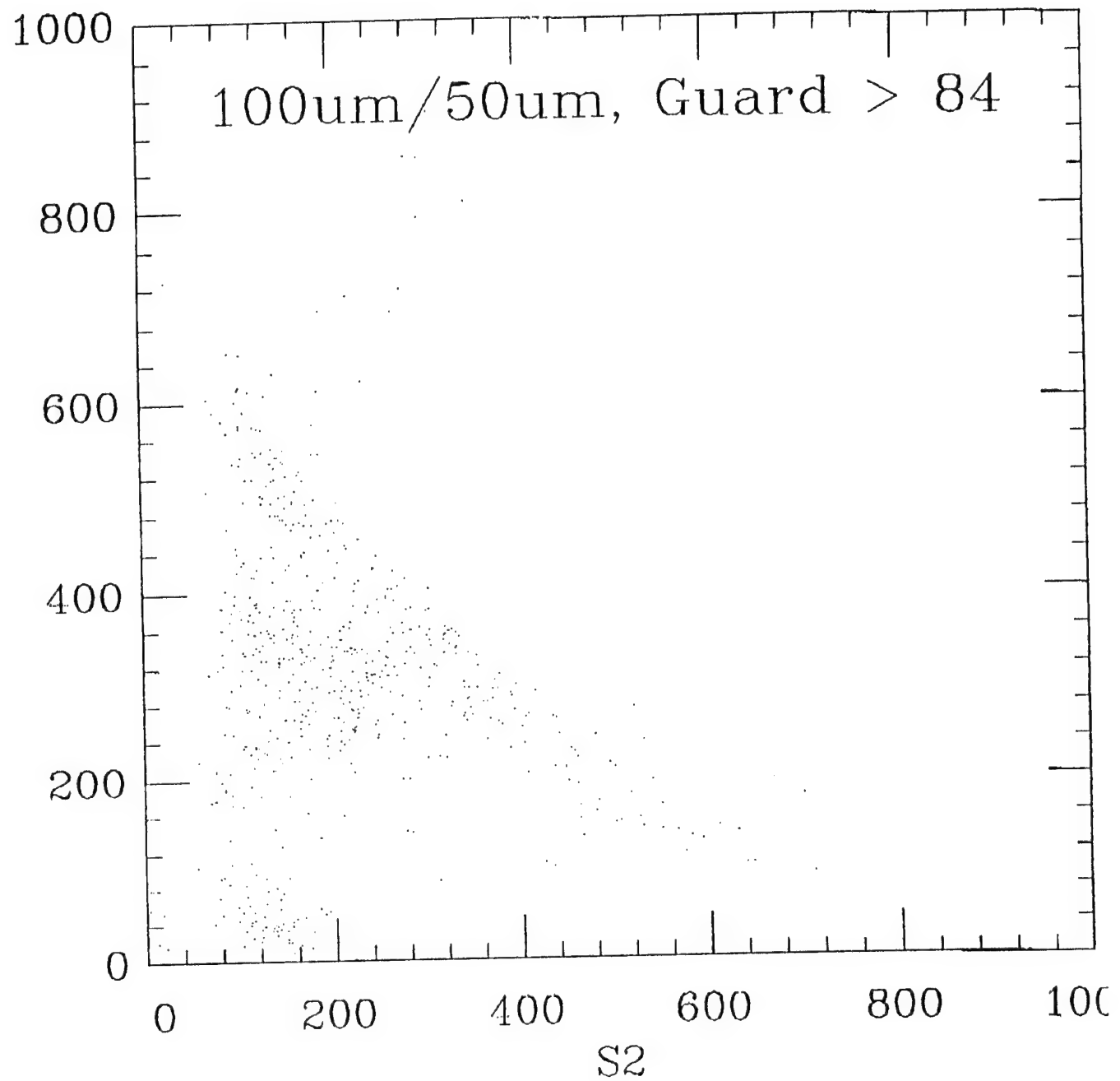
S1+S2+S3

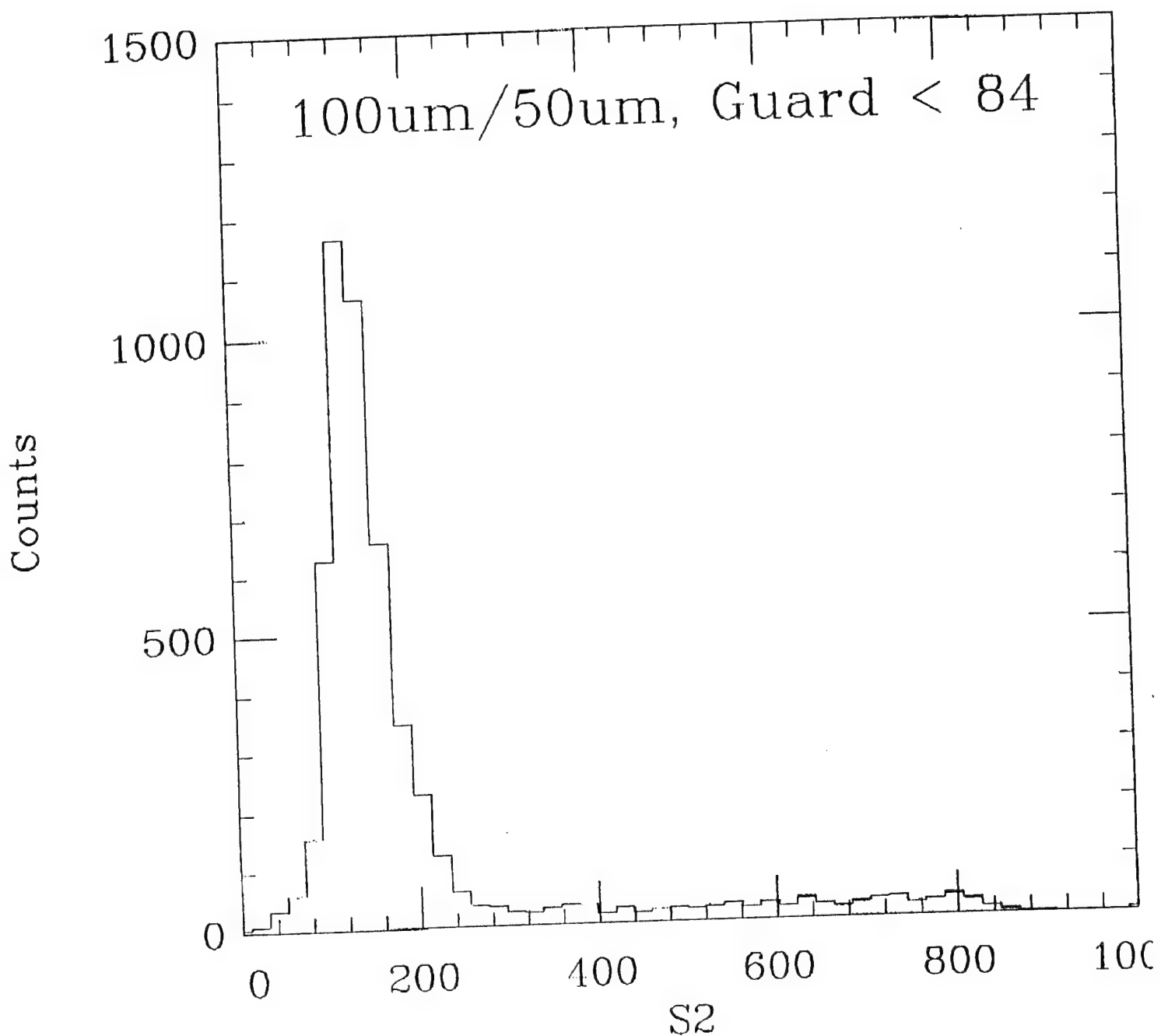


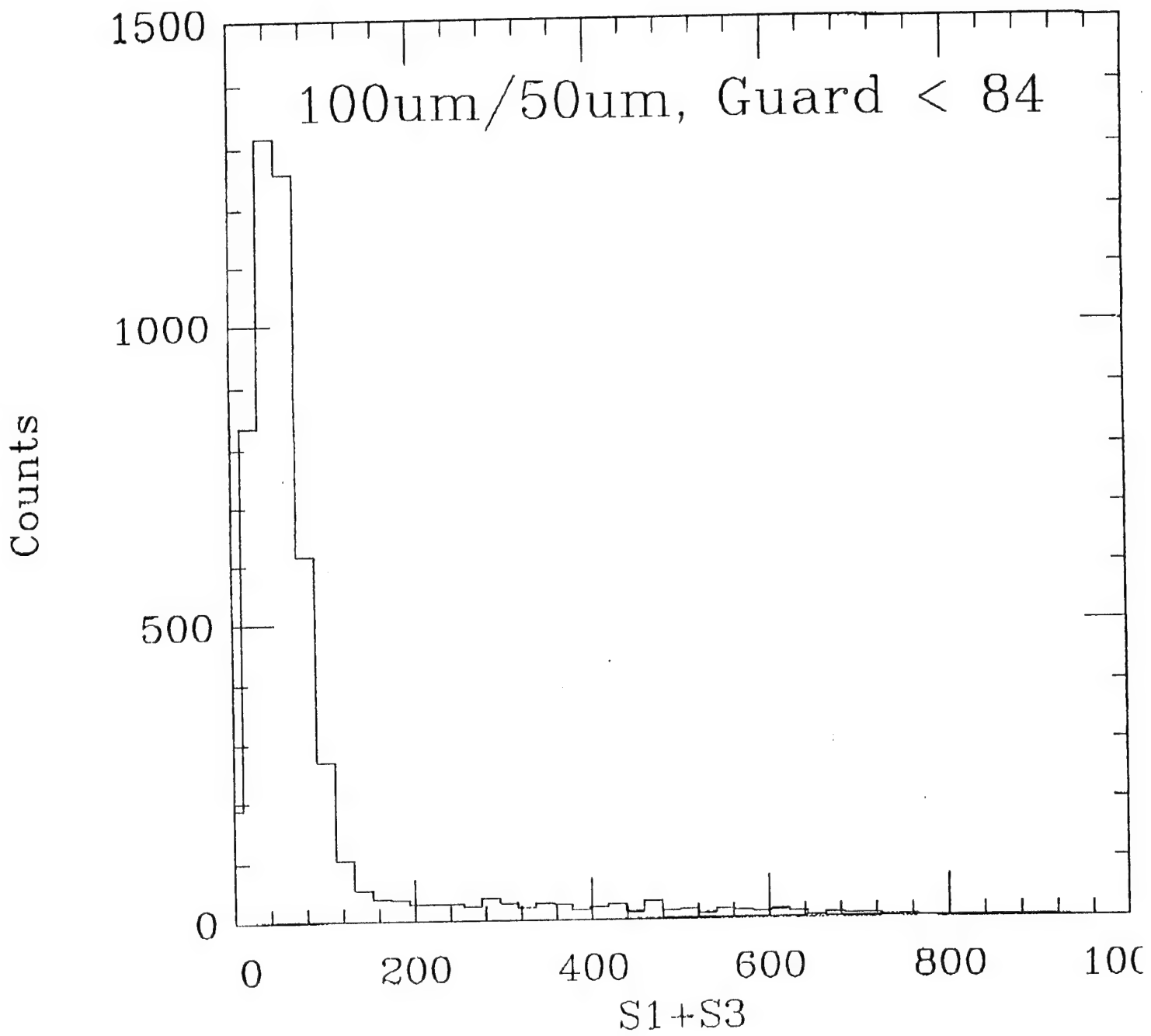
S1+S3

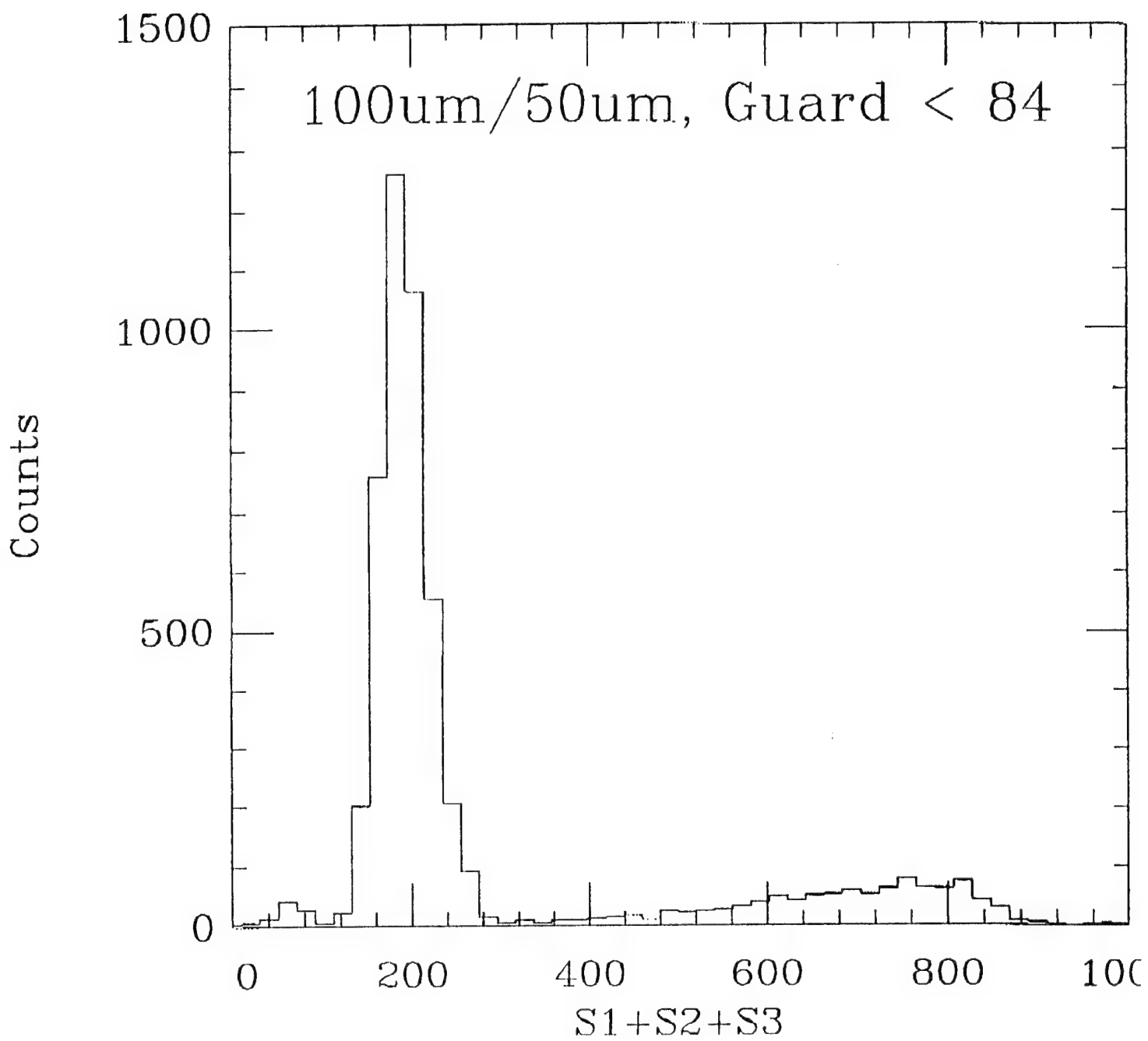


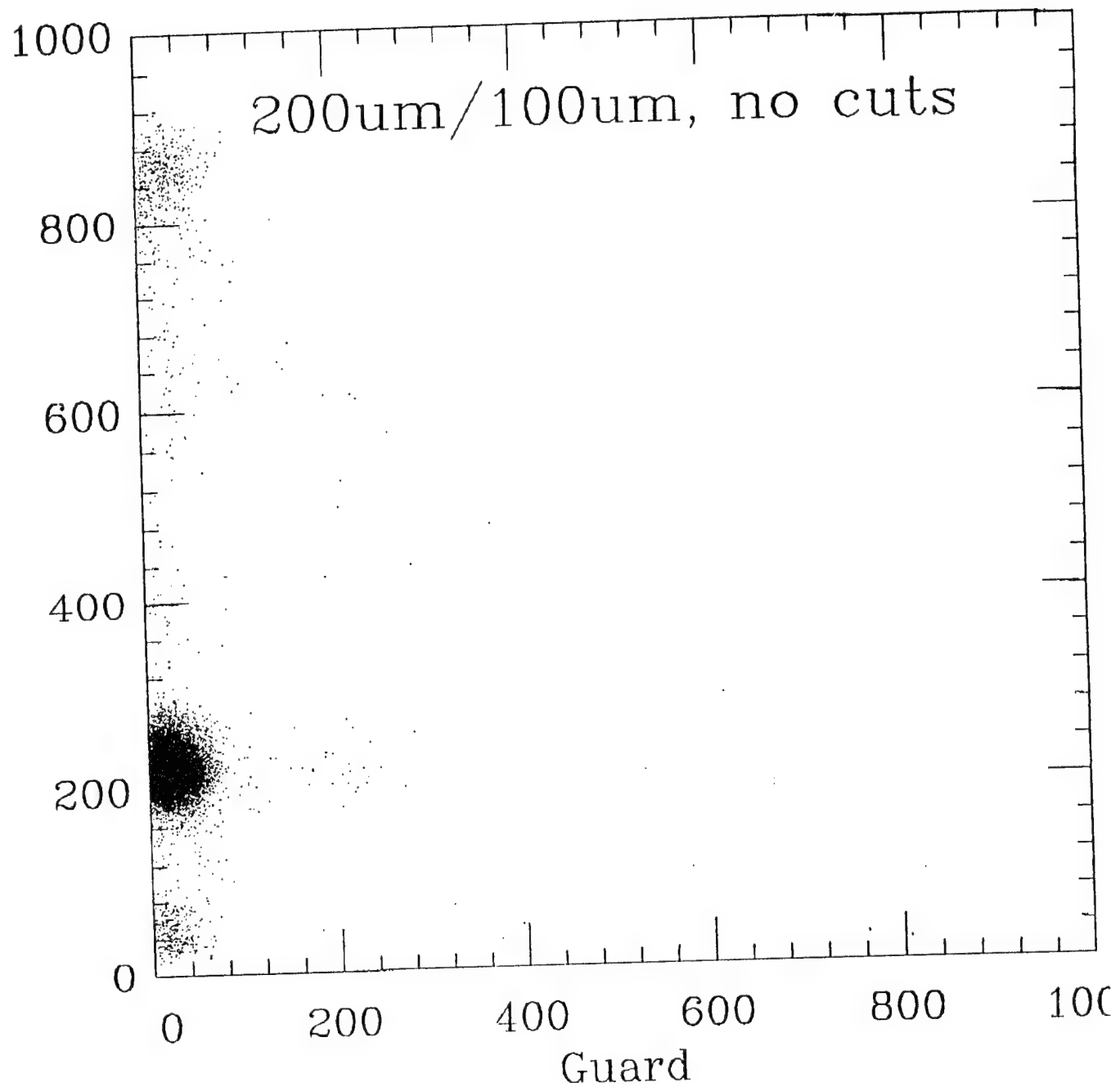
S1+S3



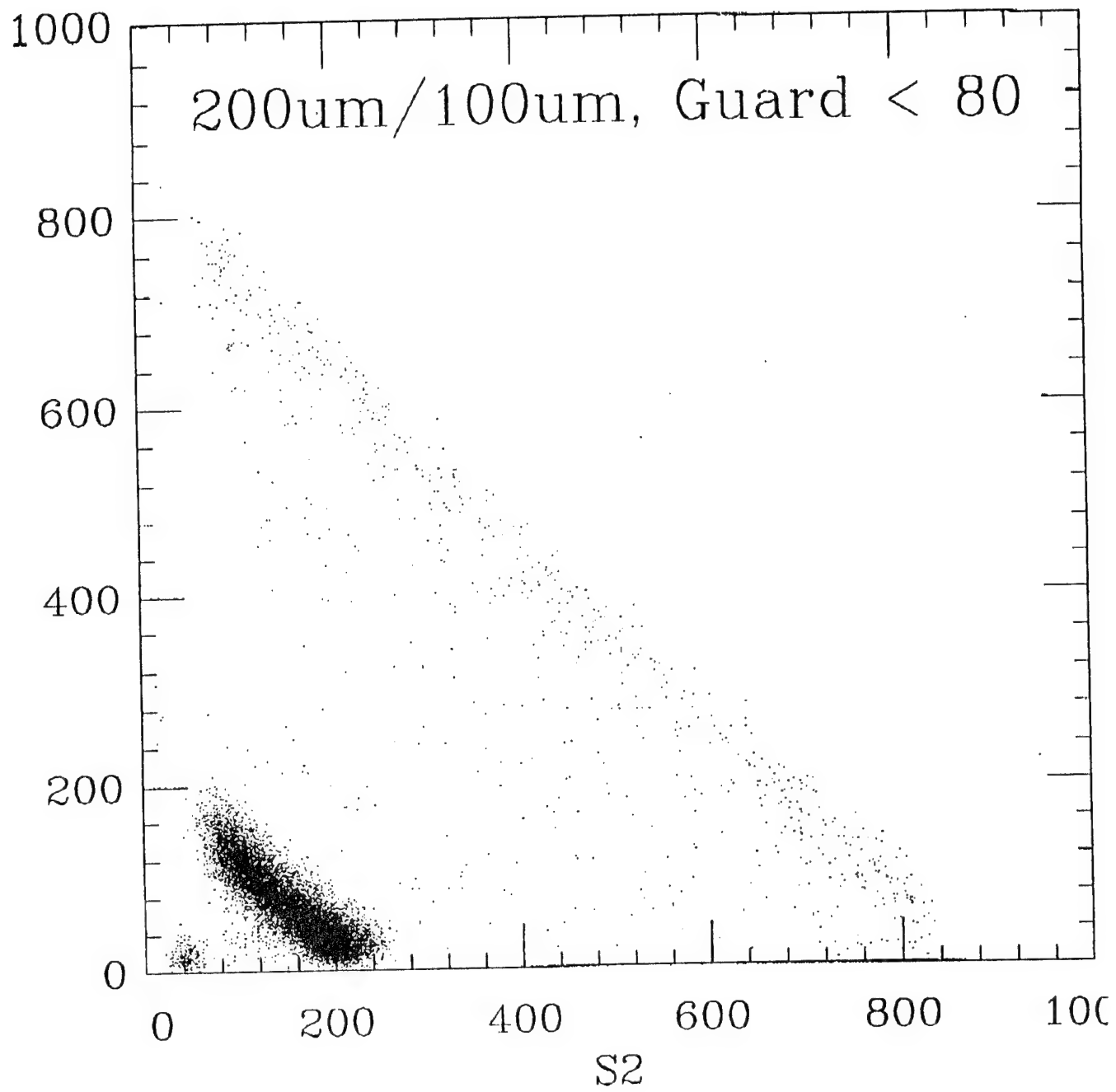


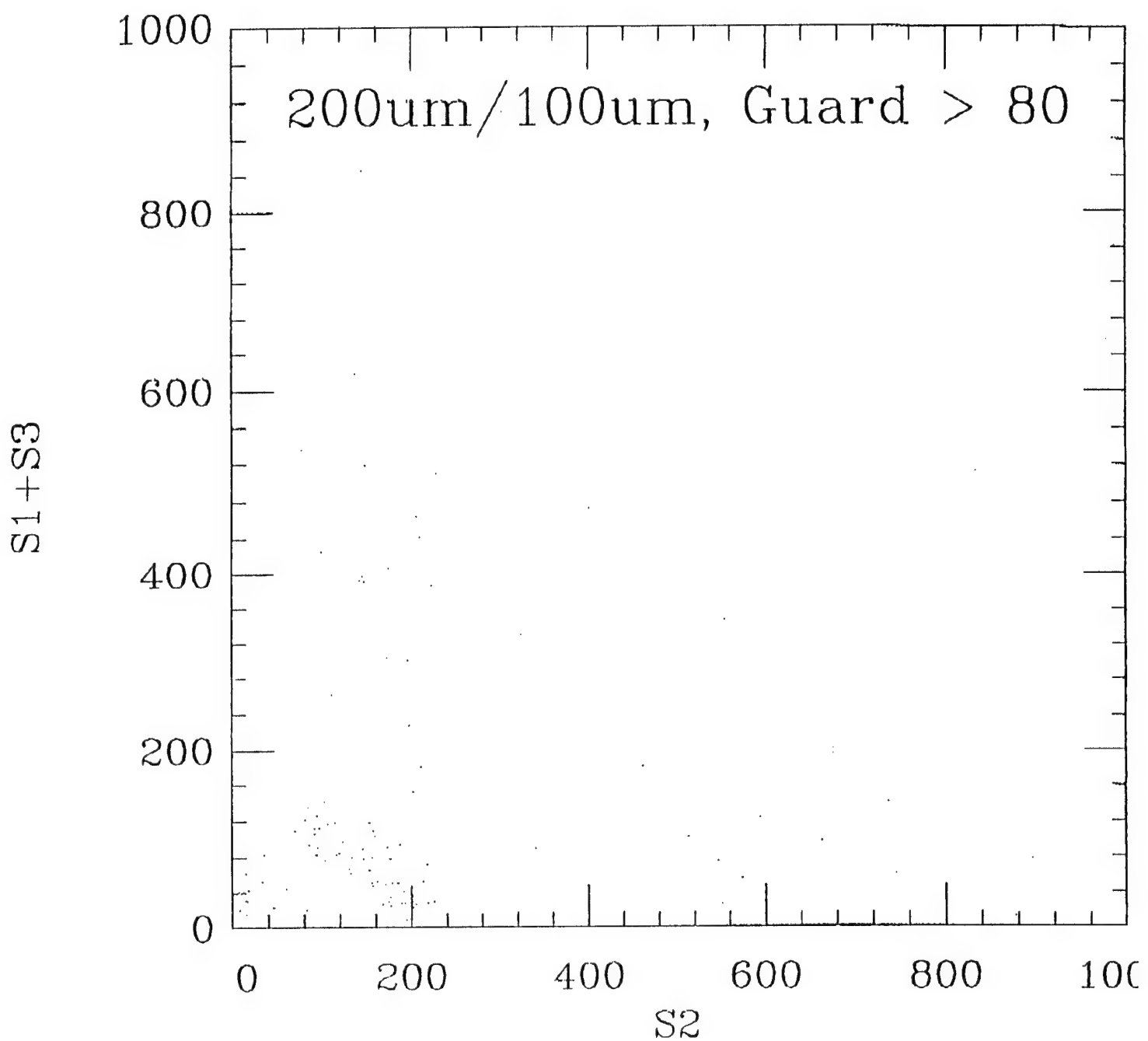


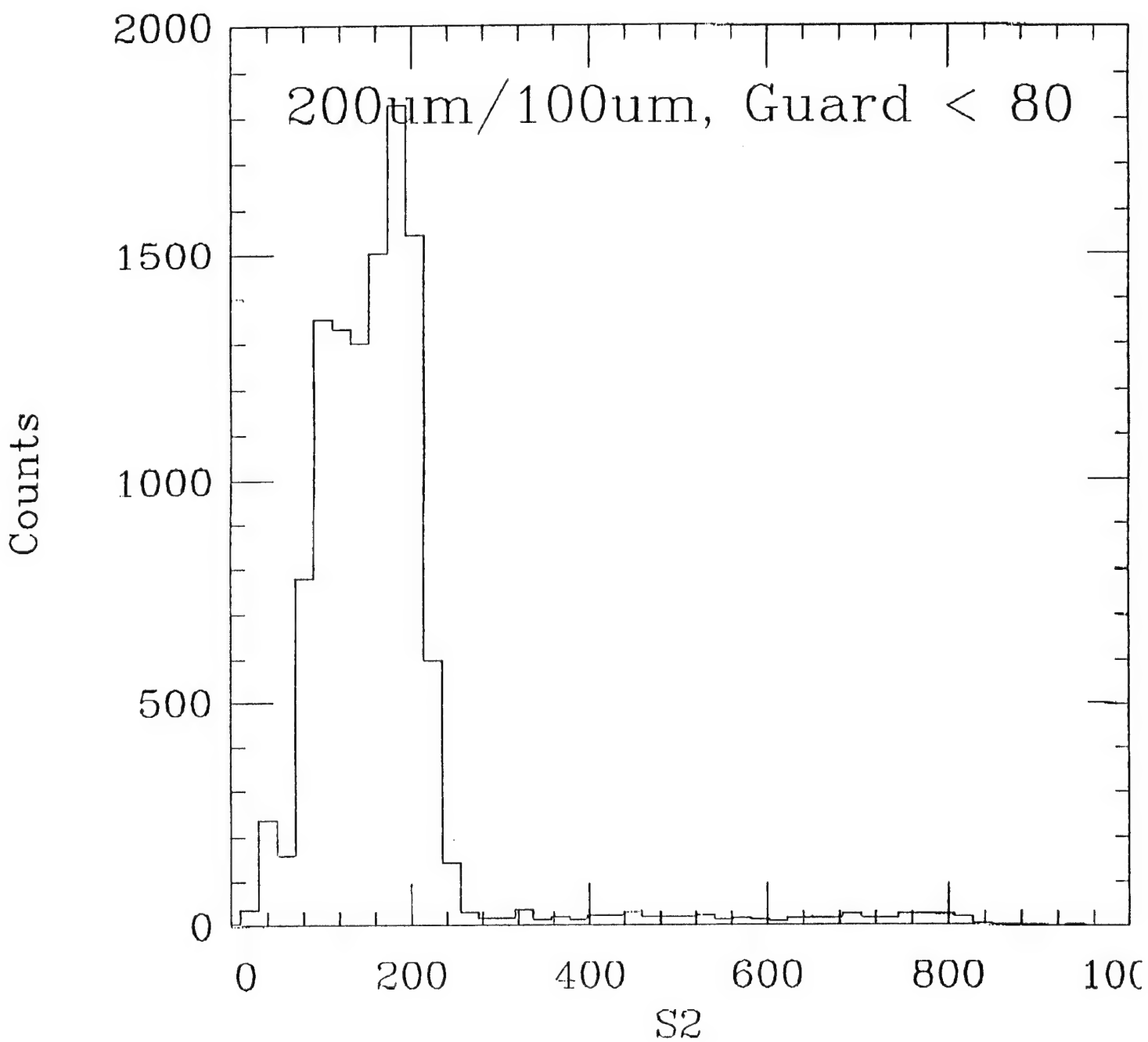


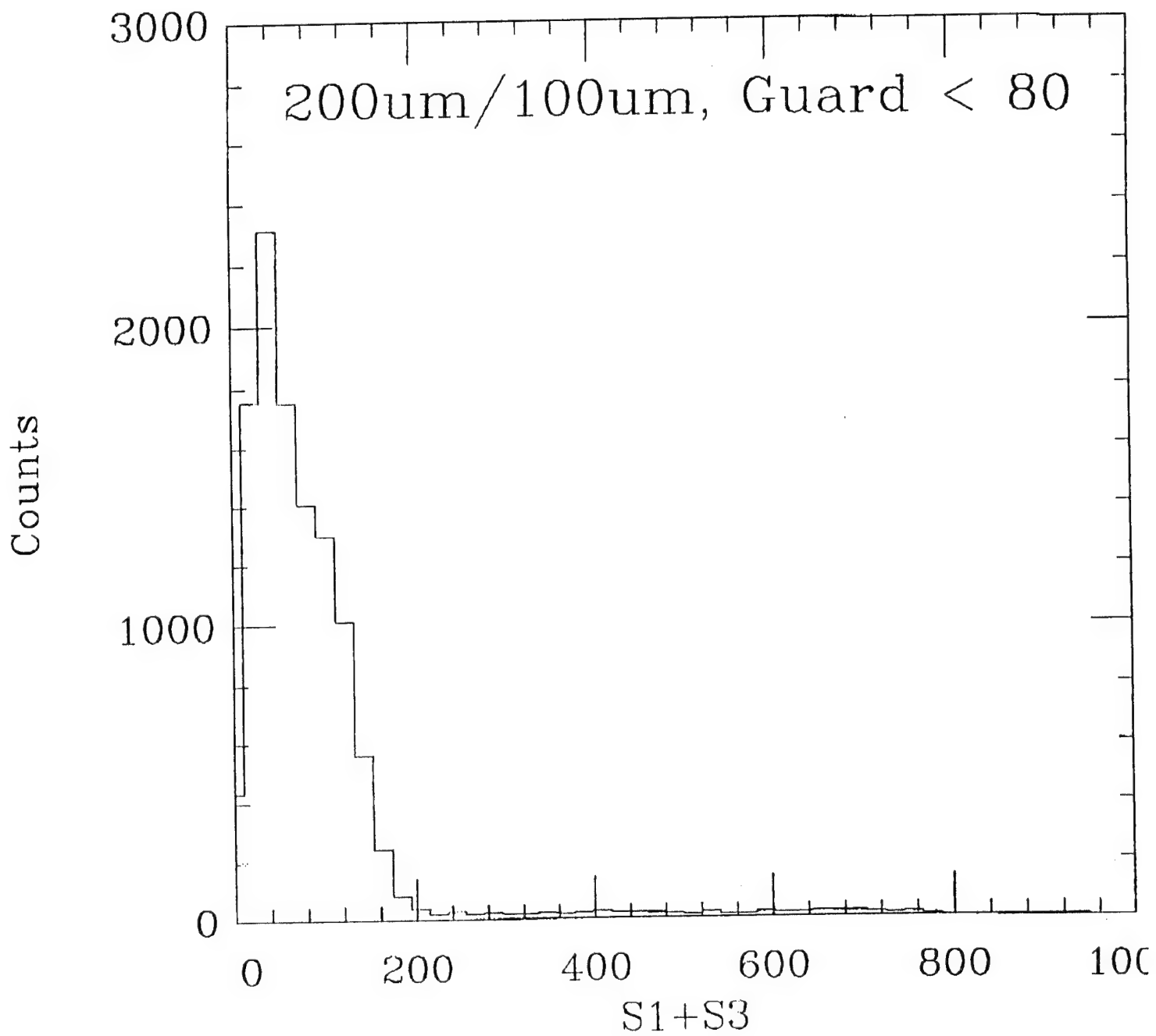


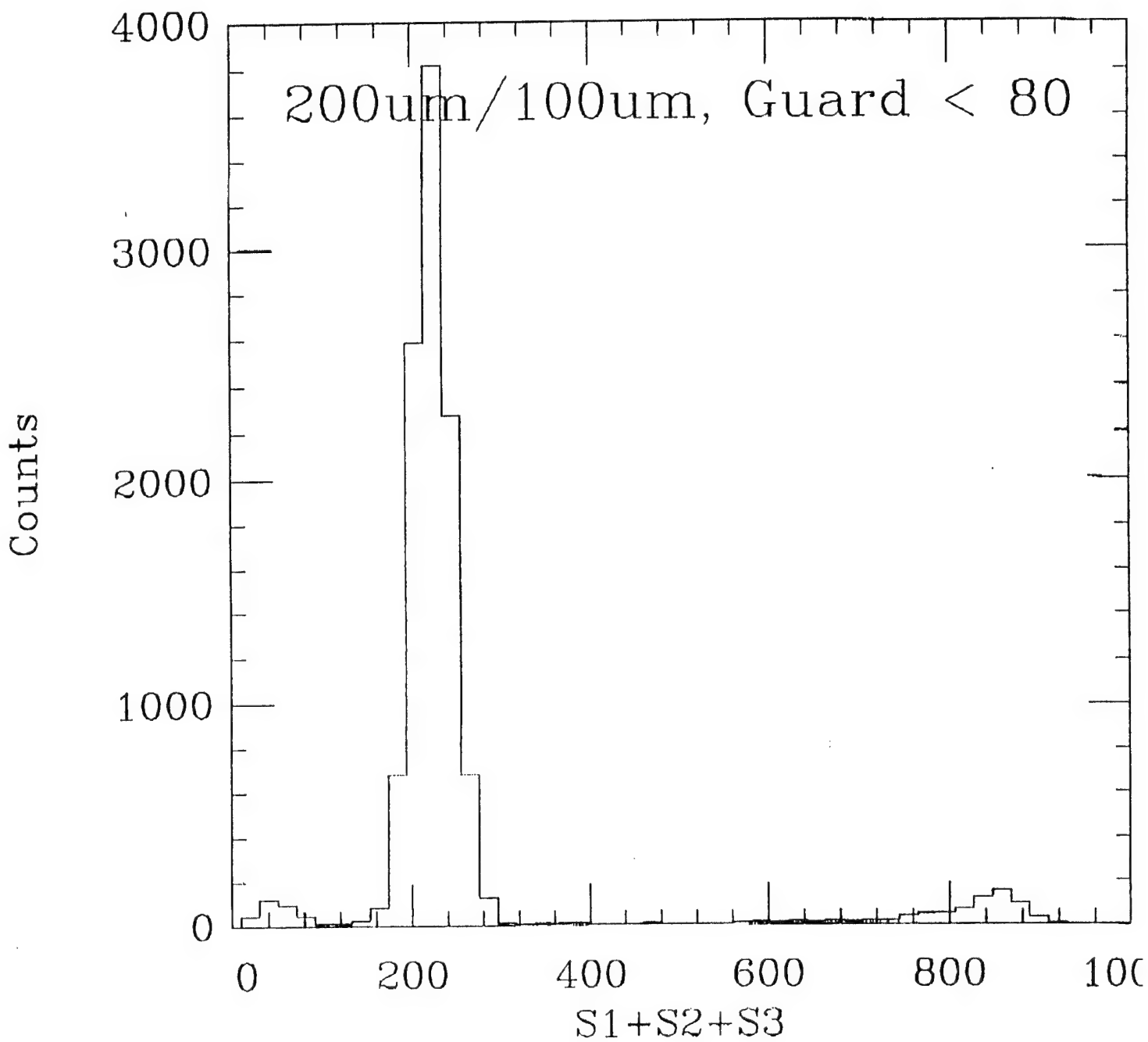
S1 + S3

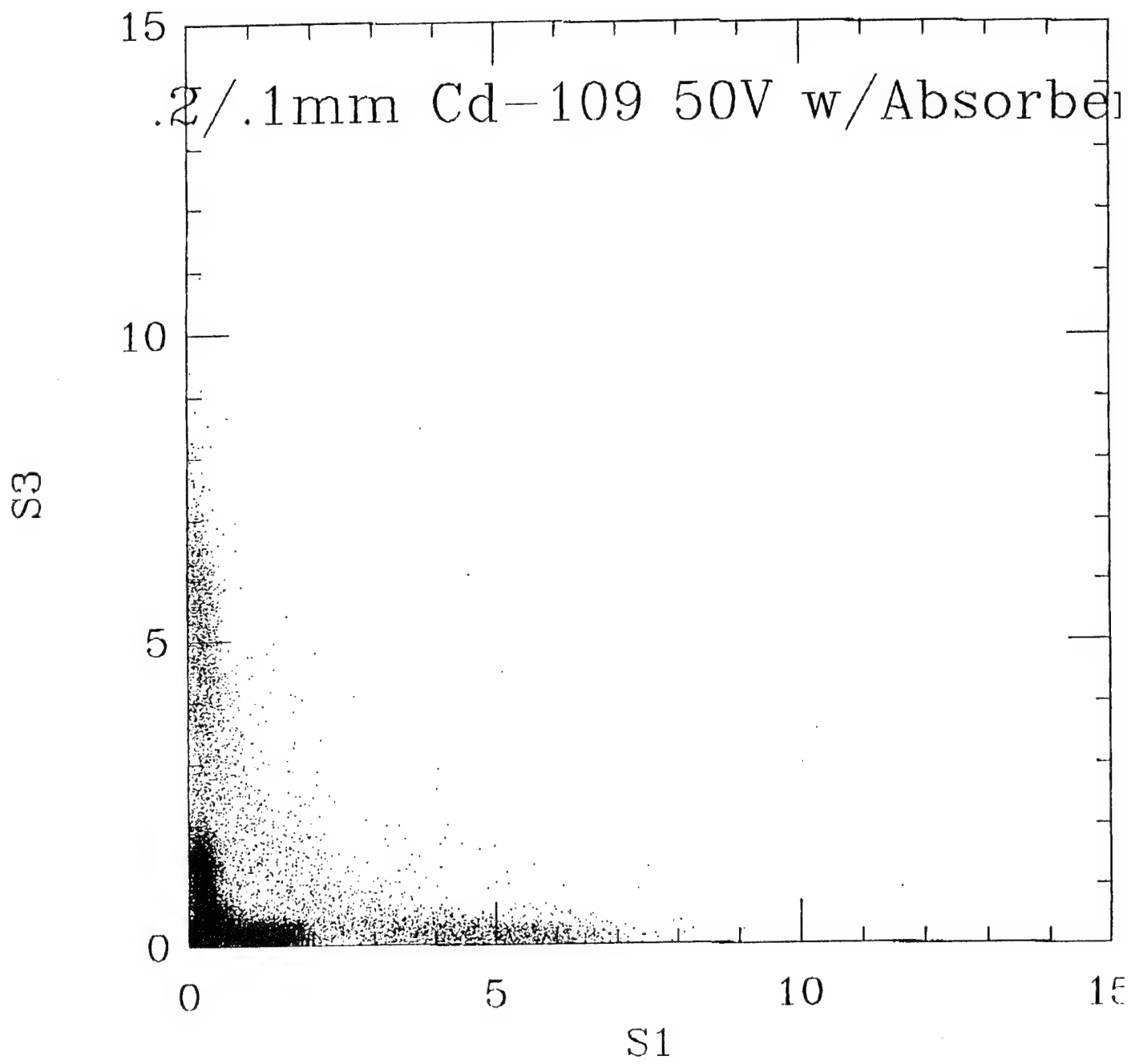


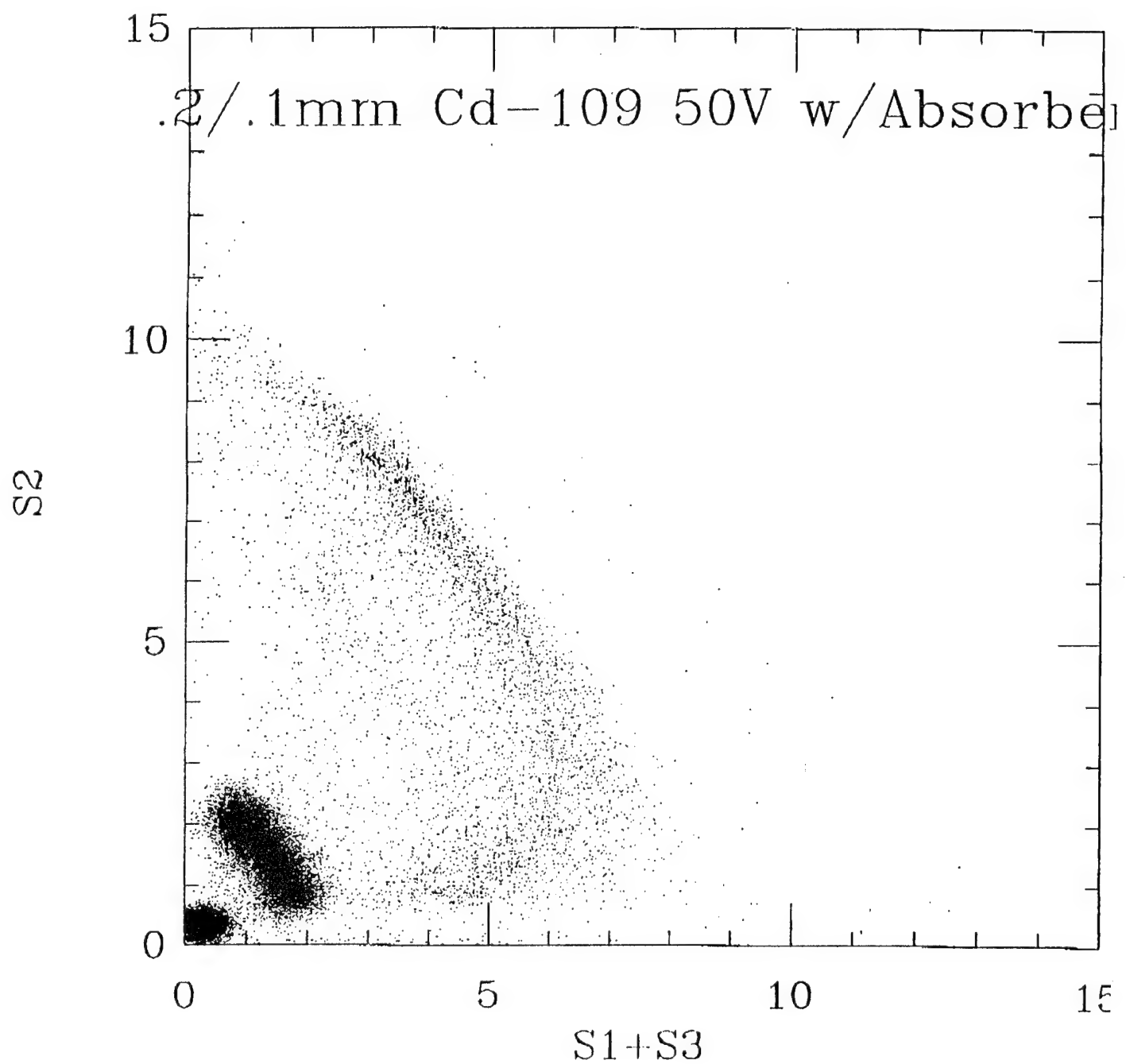


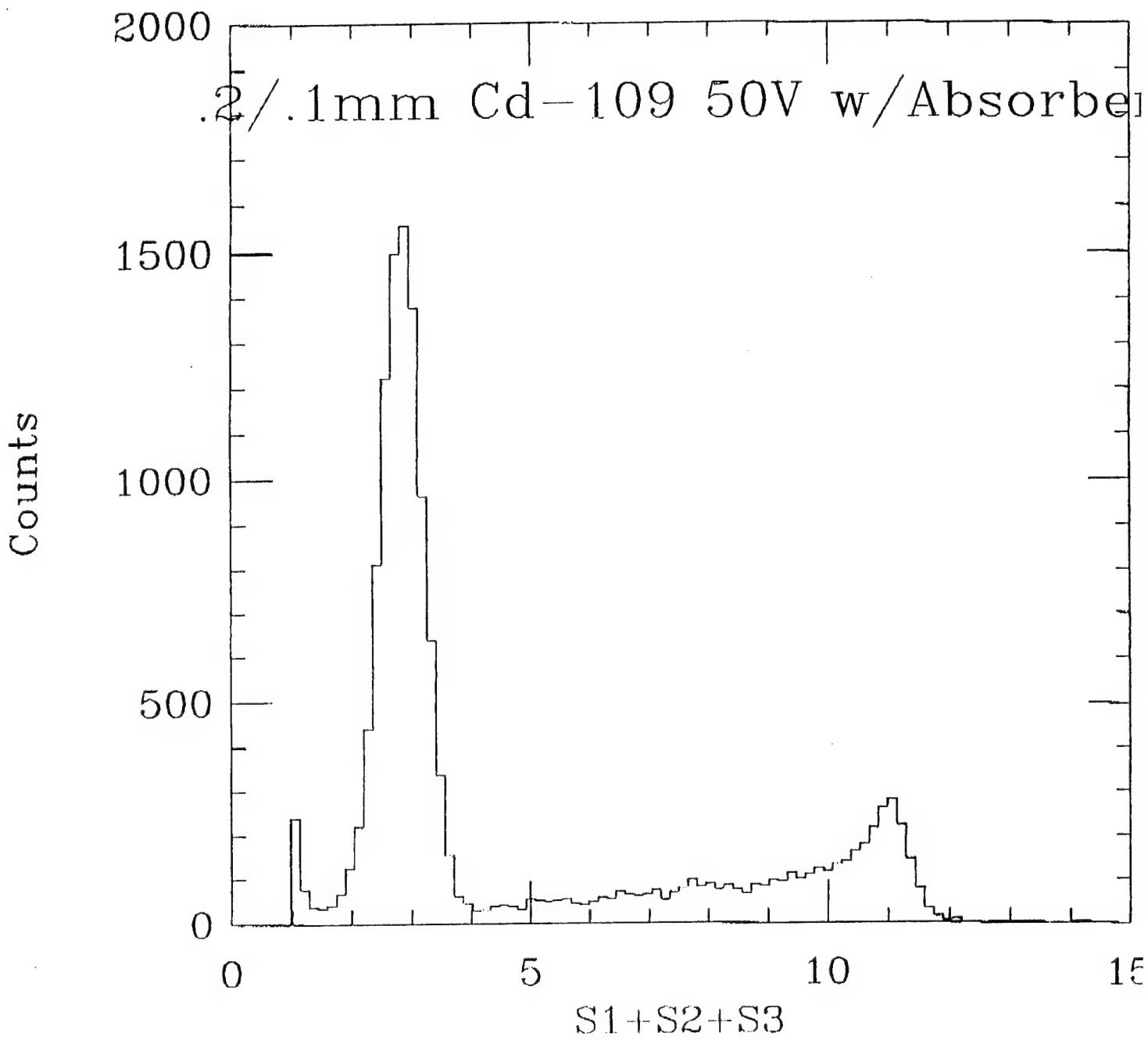


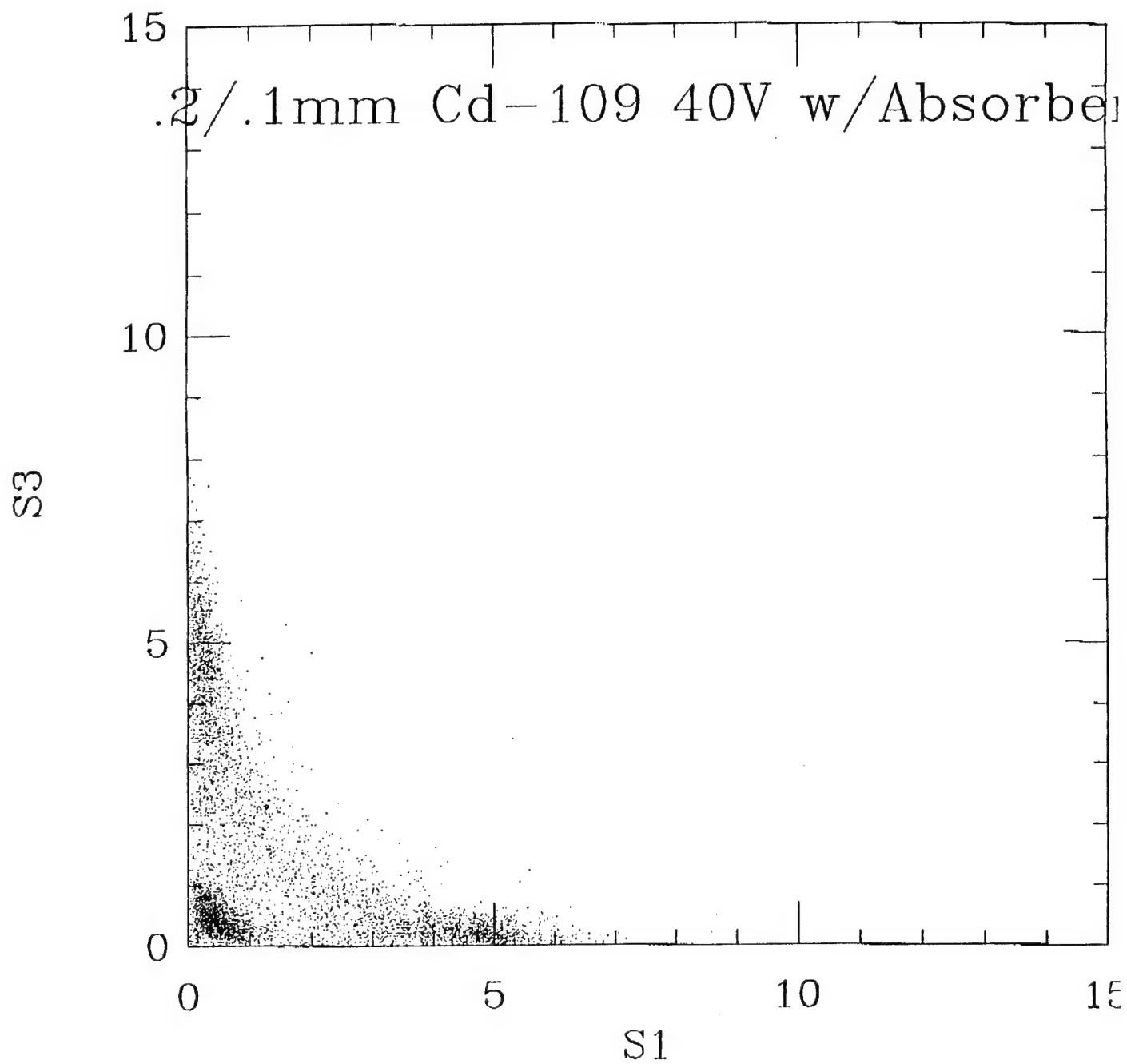


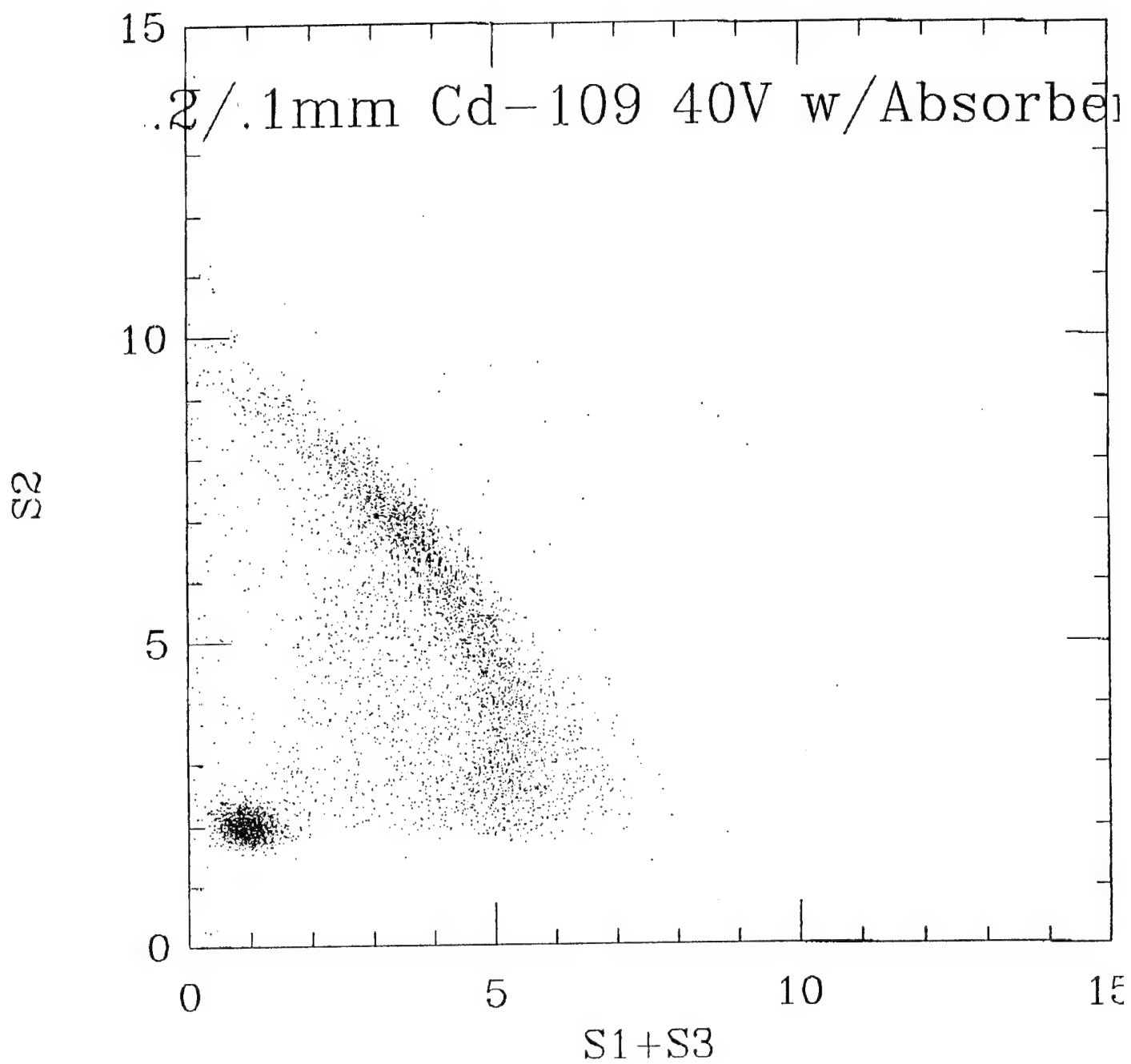


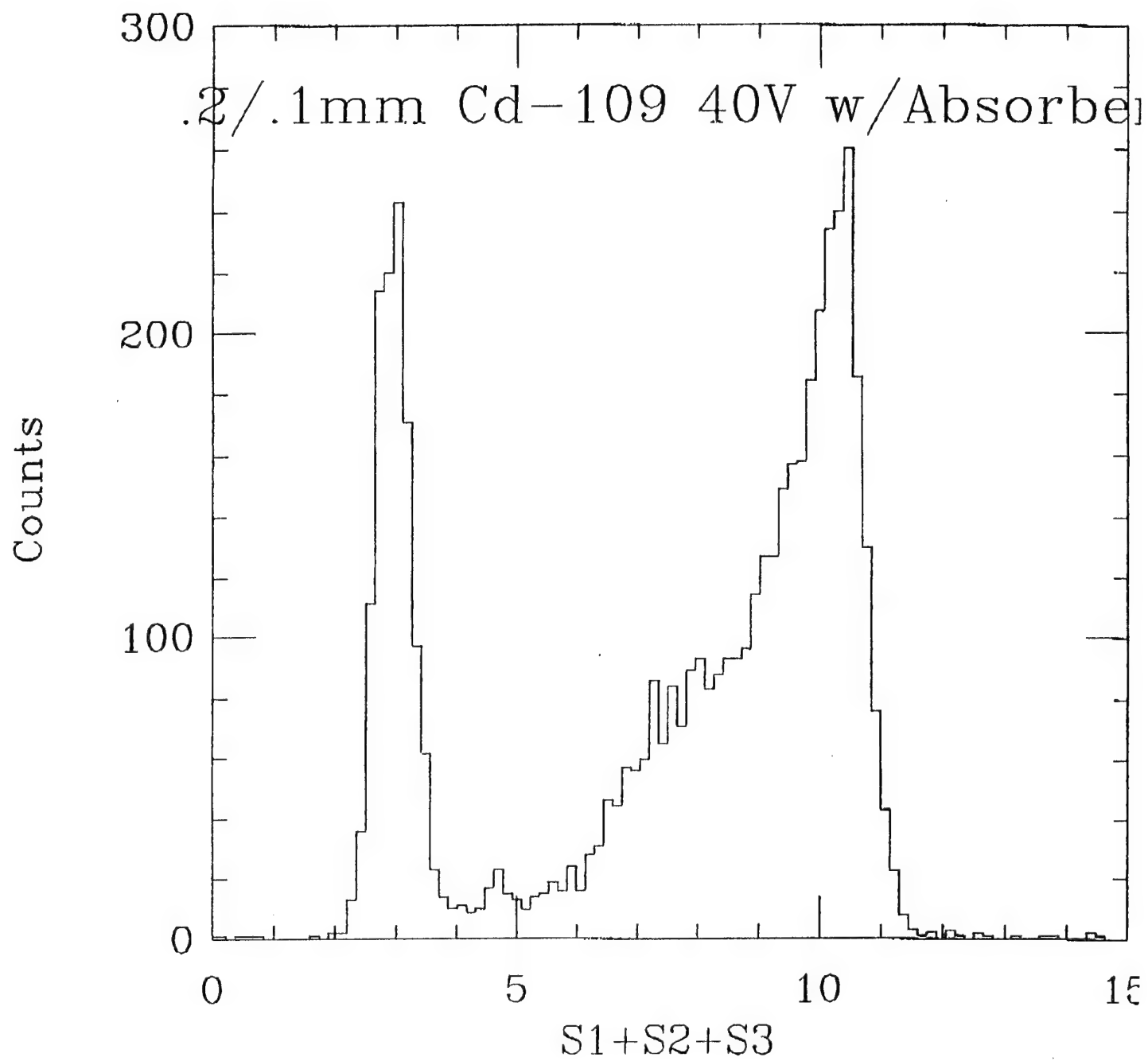


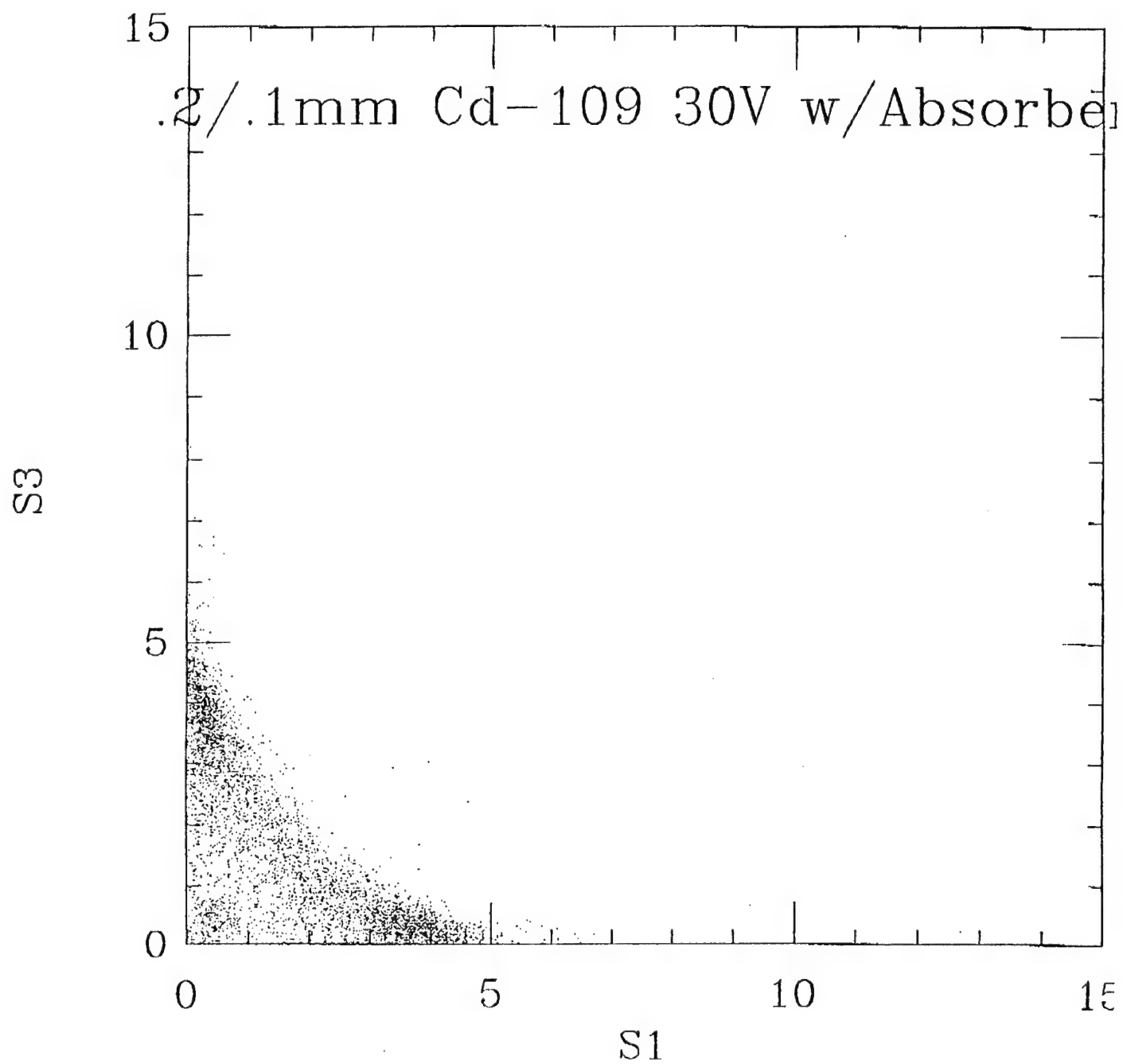


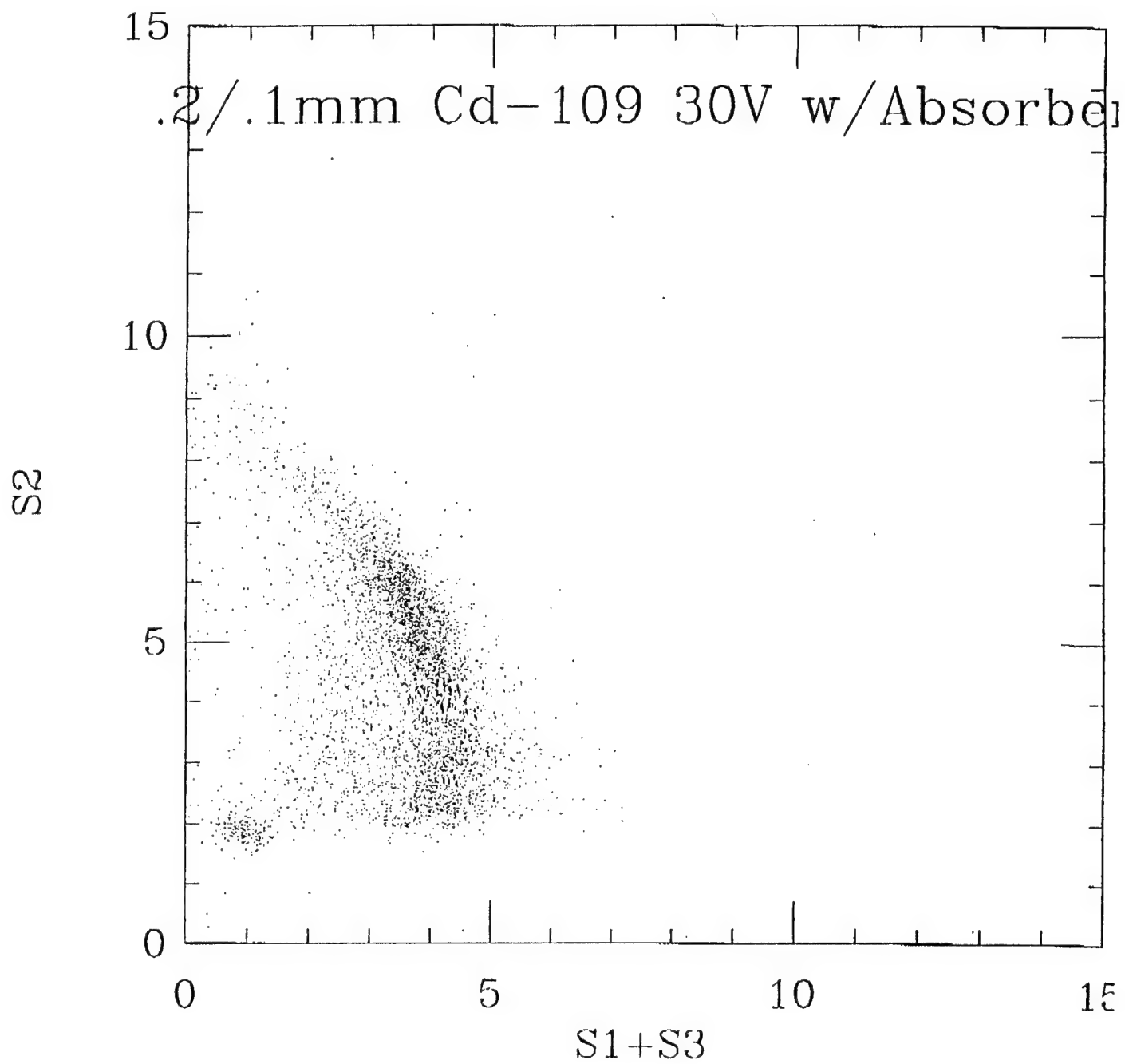


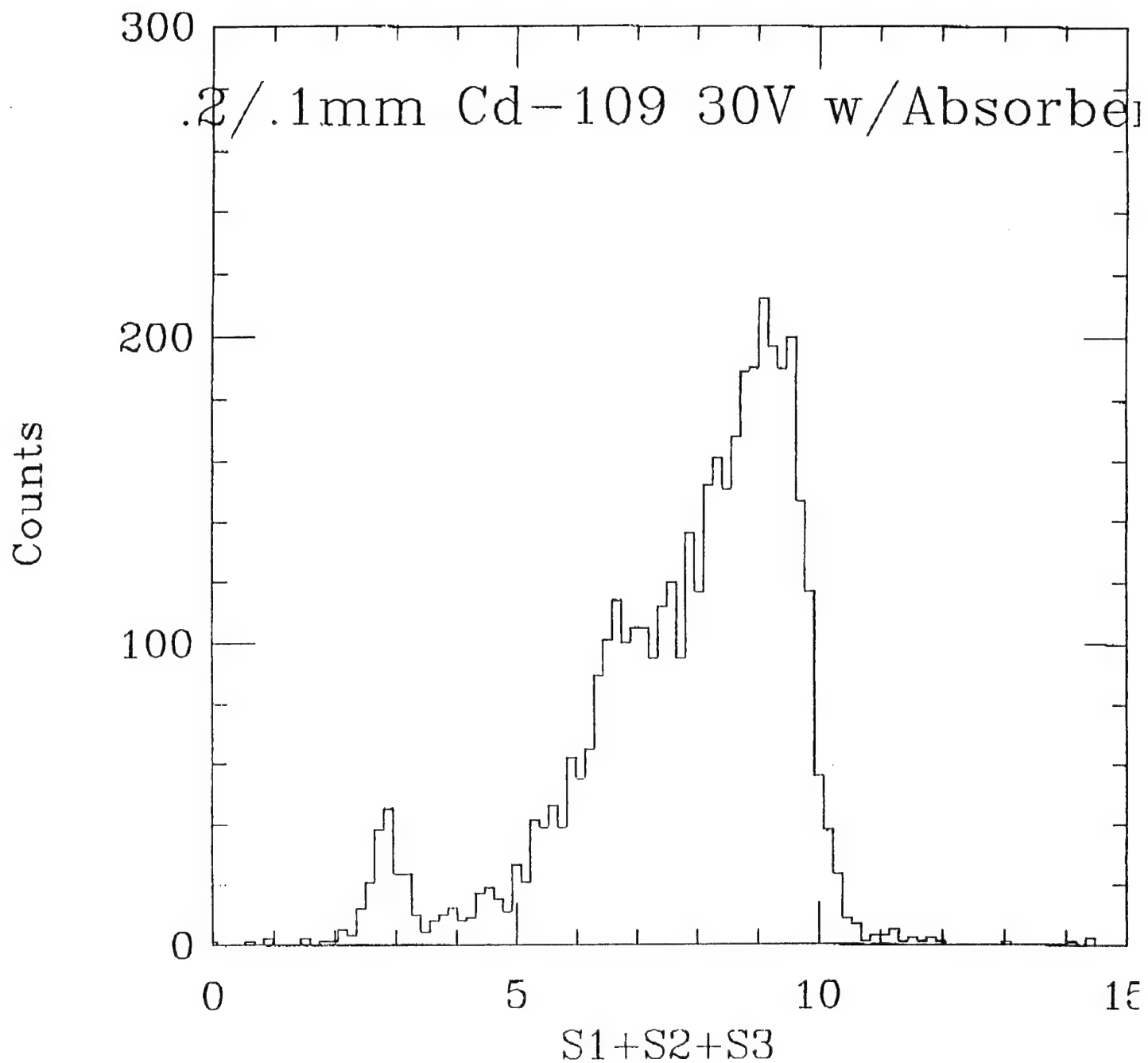


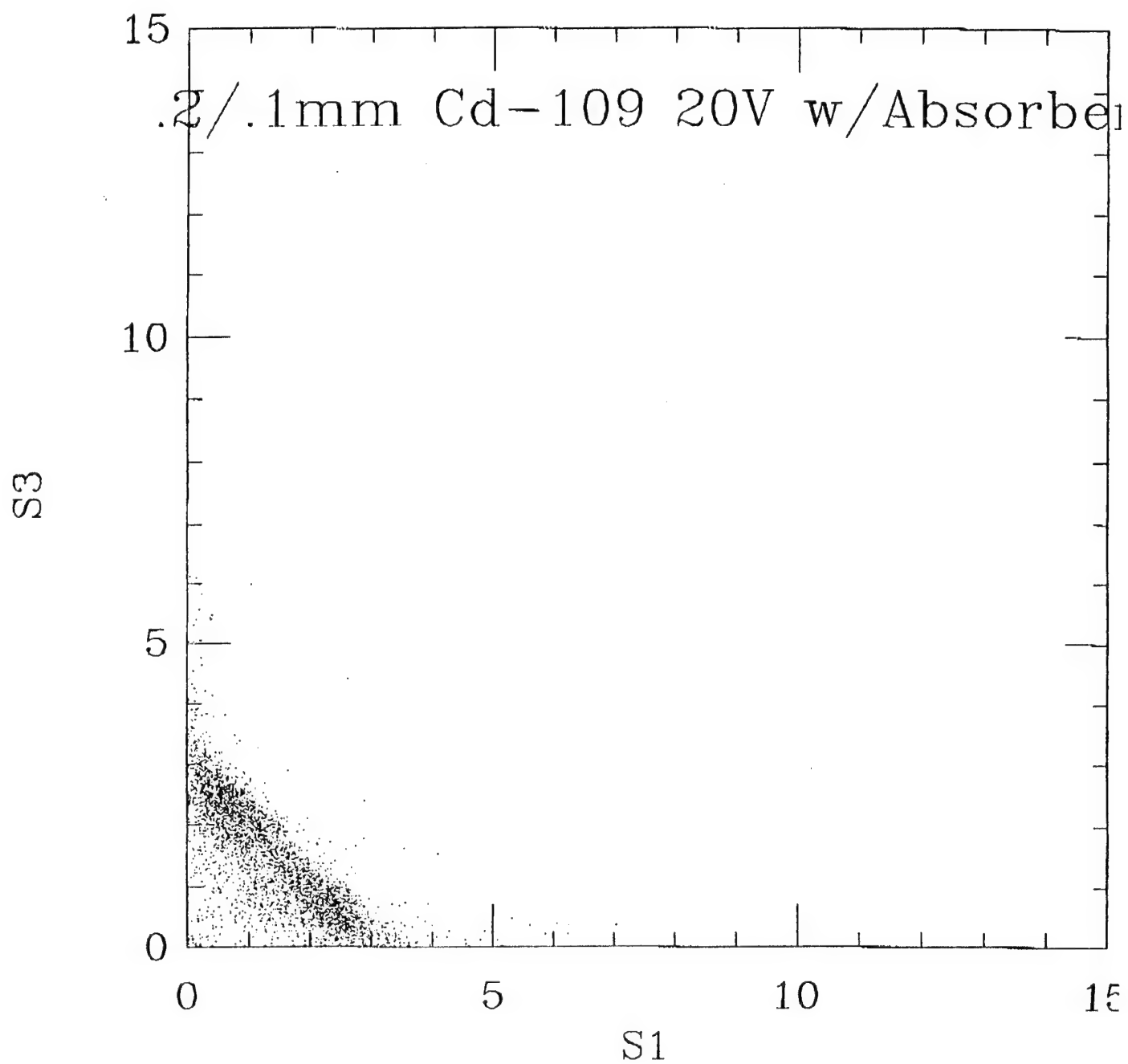


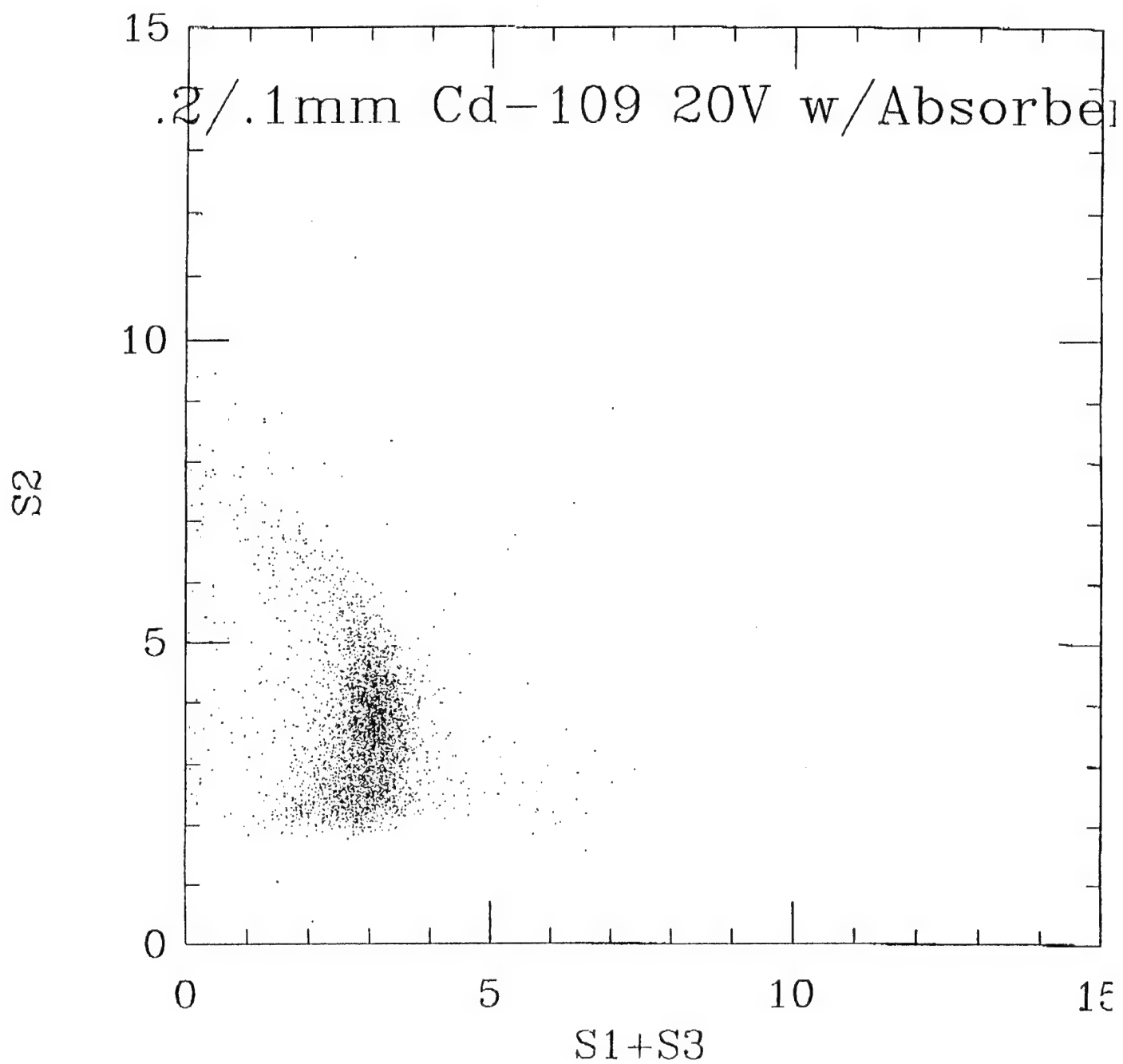


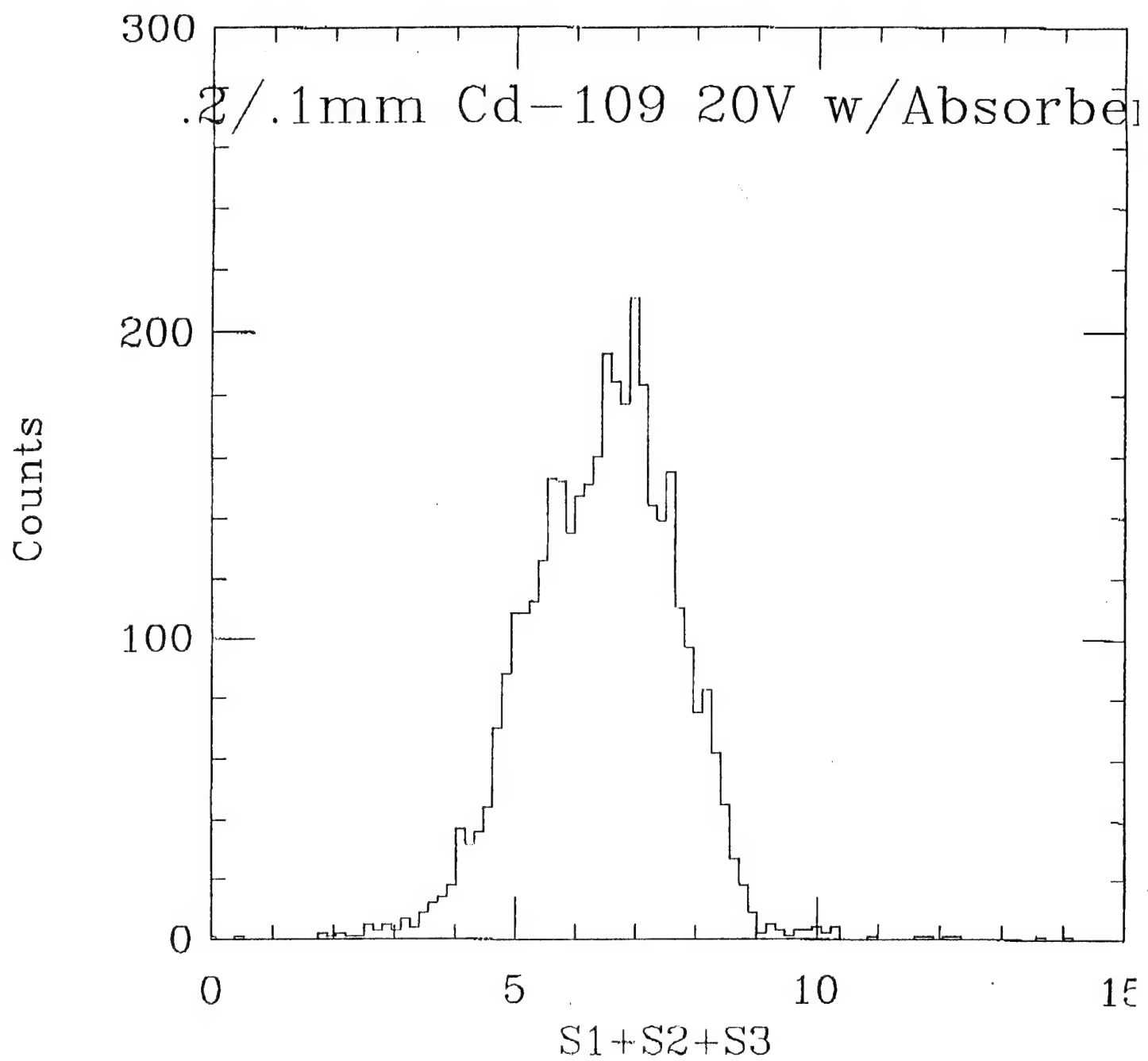


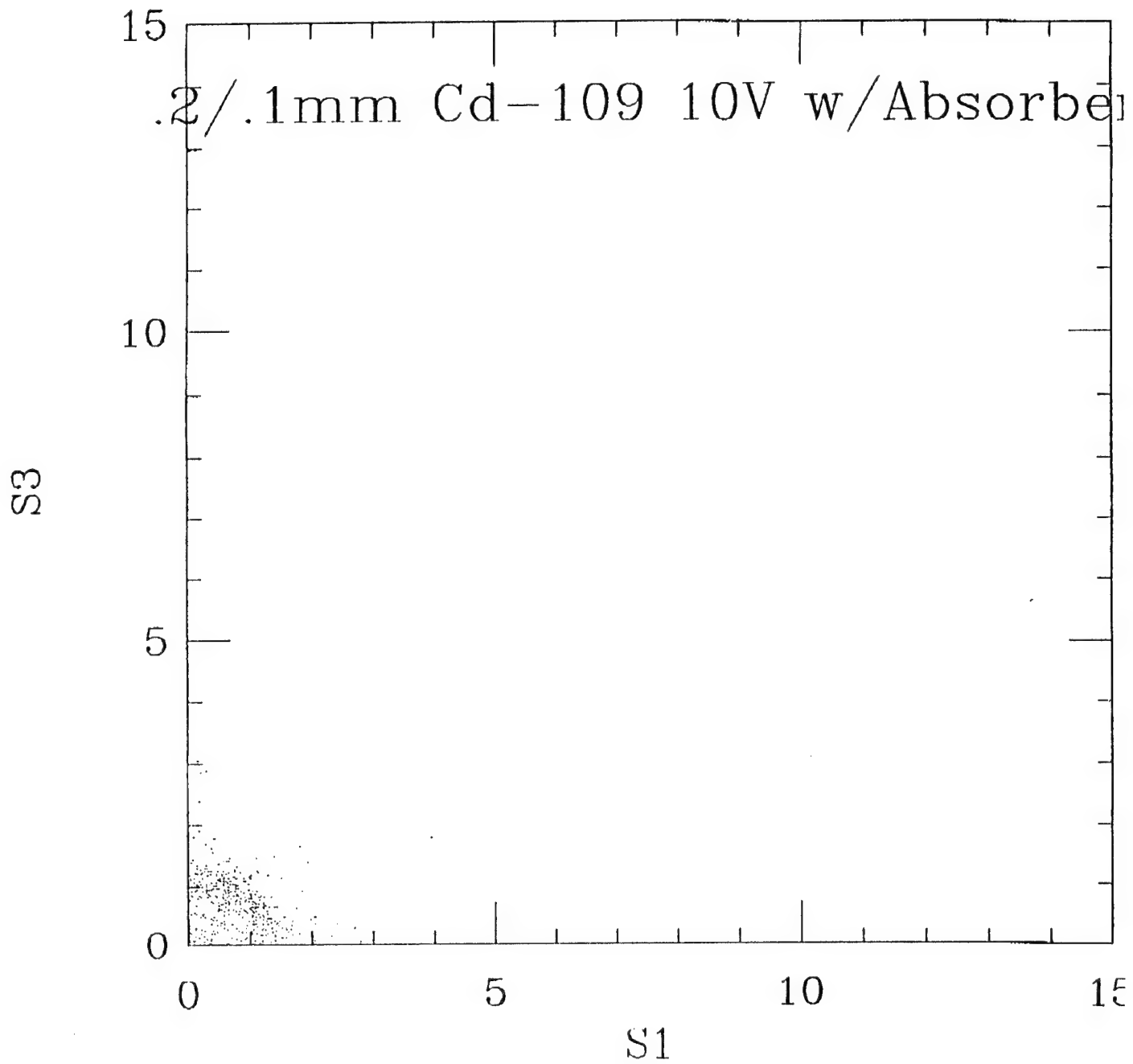


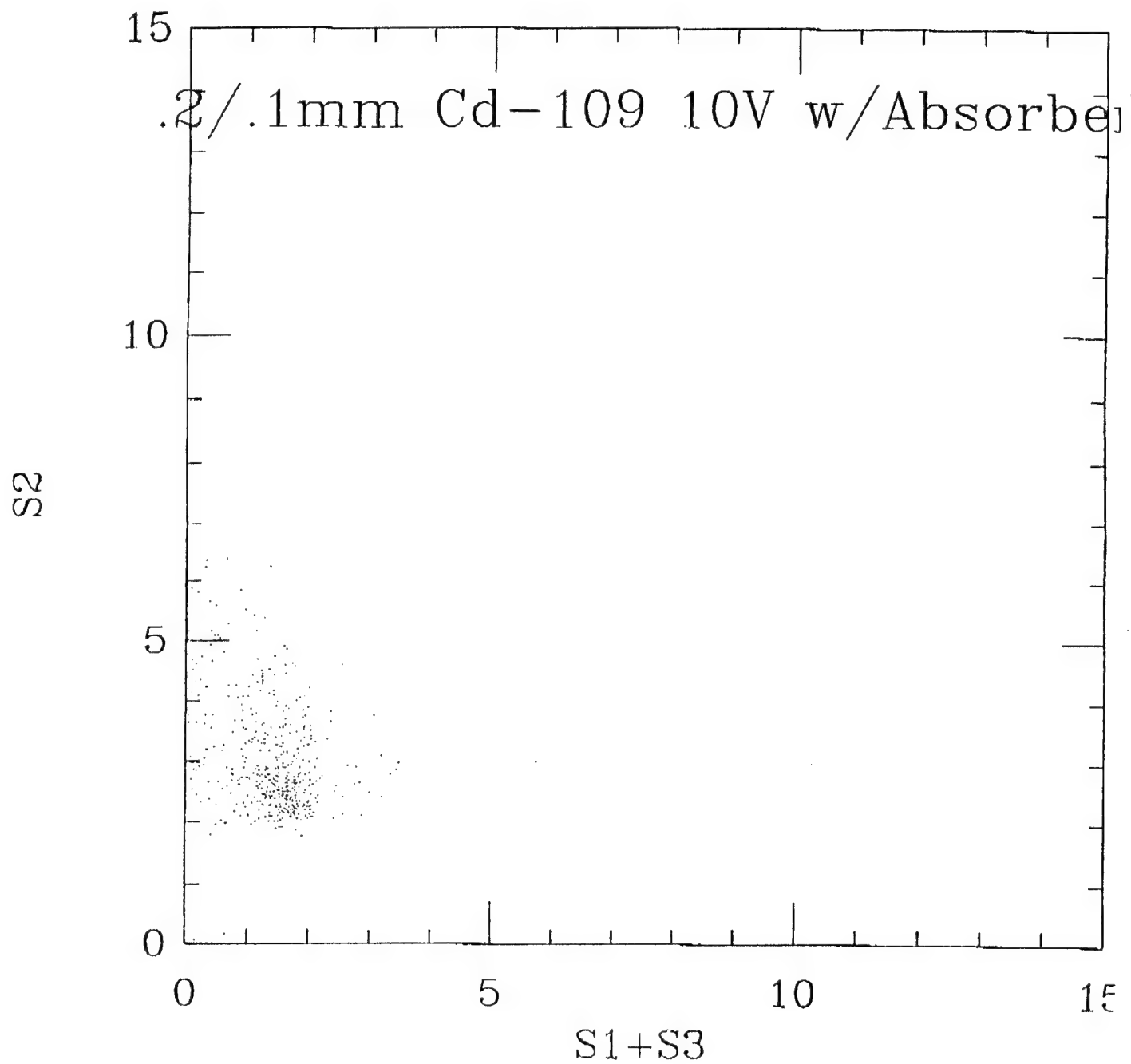


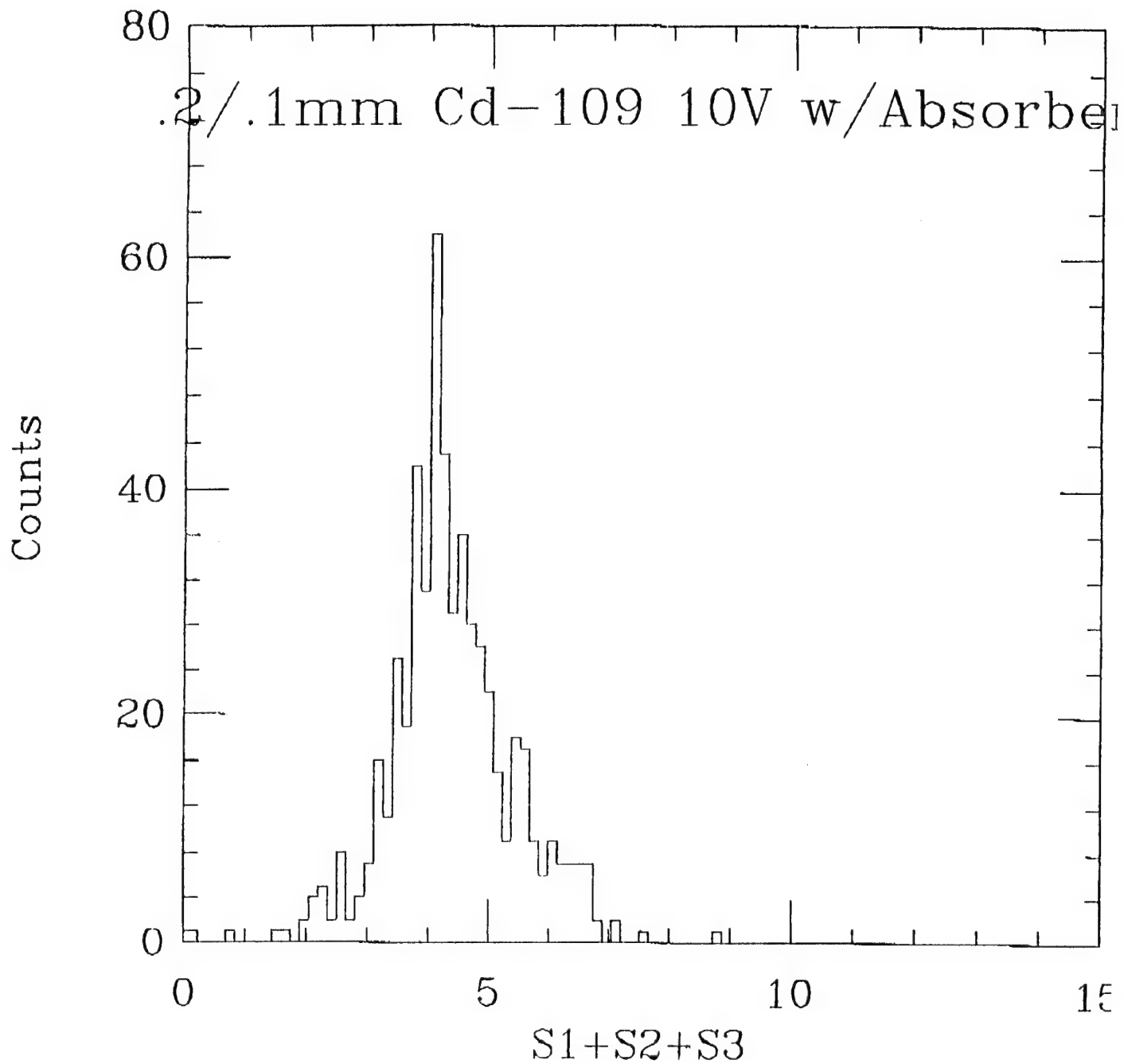




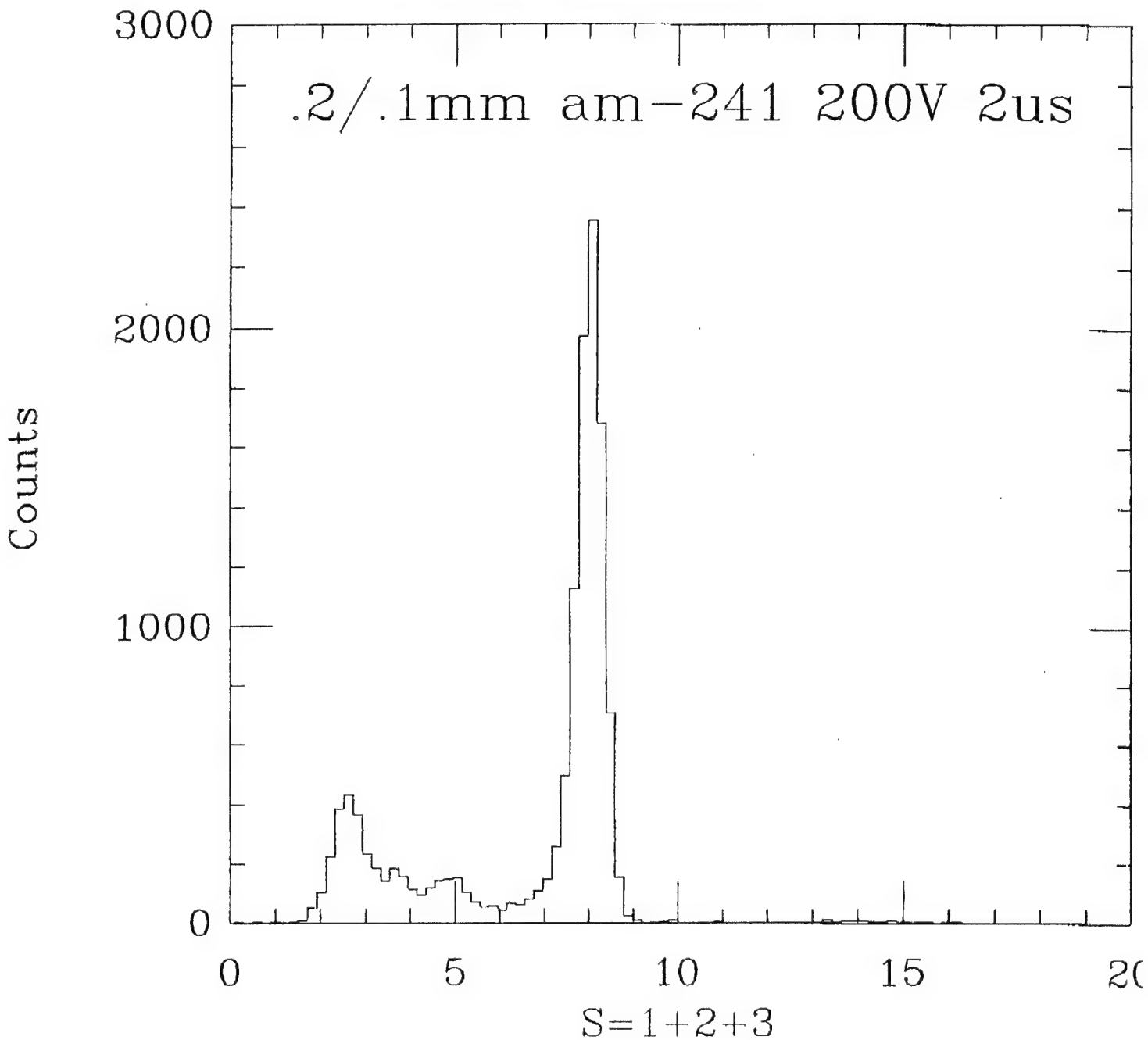


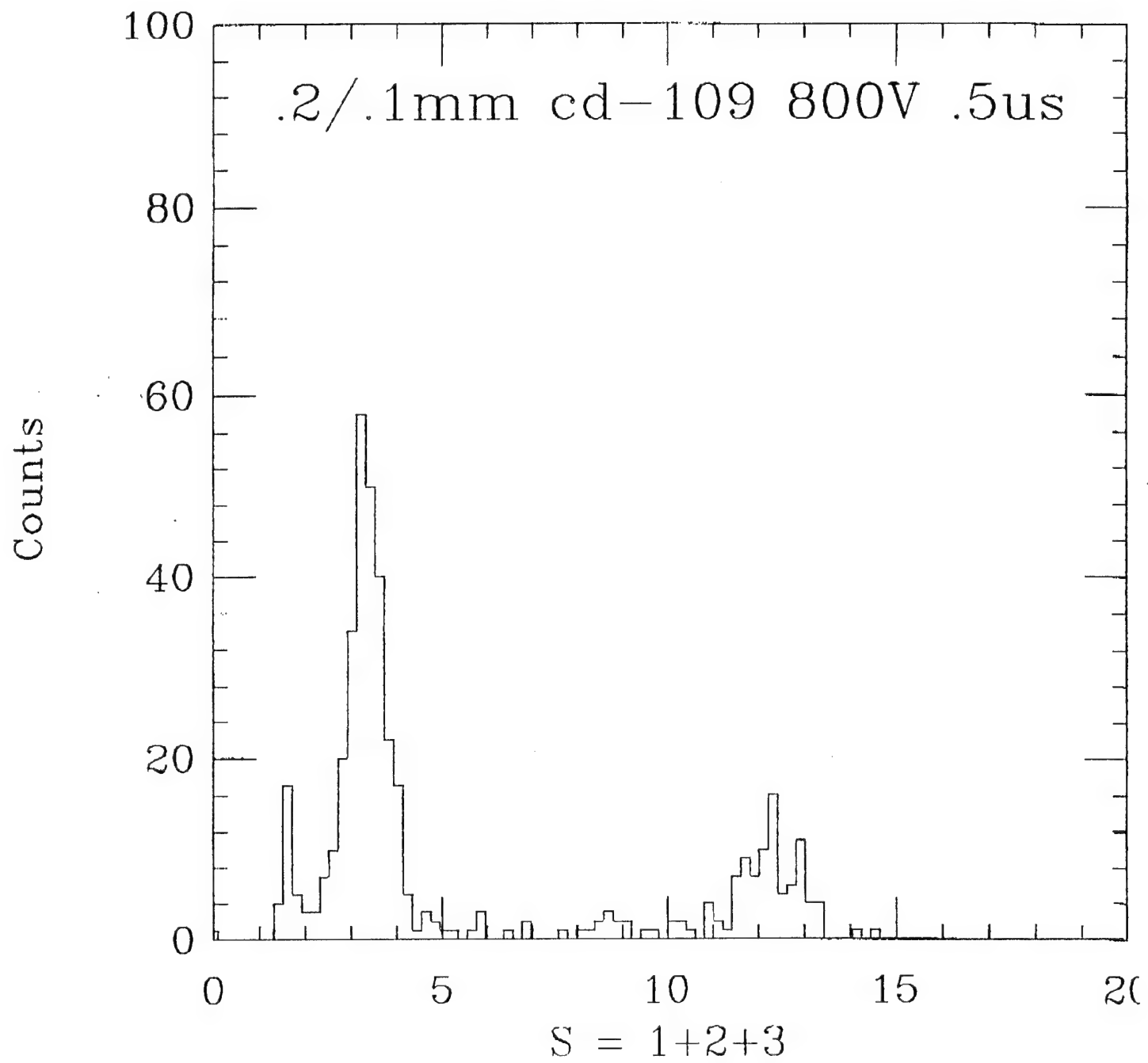


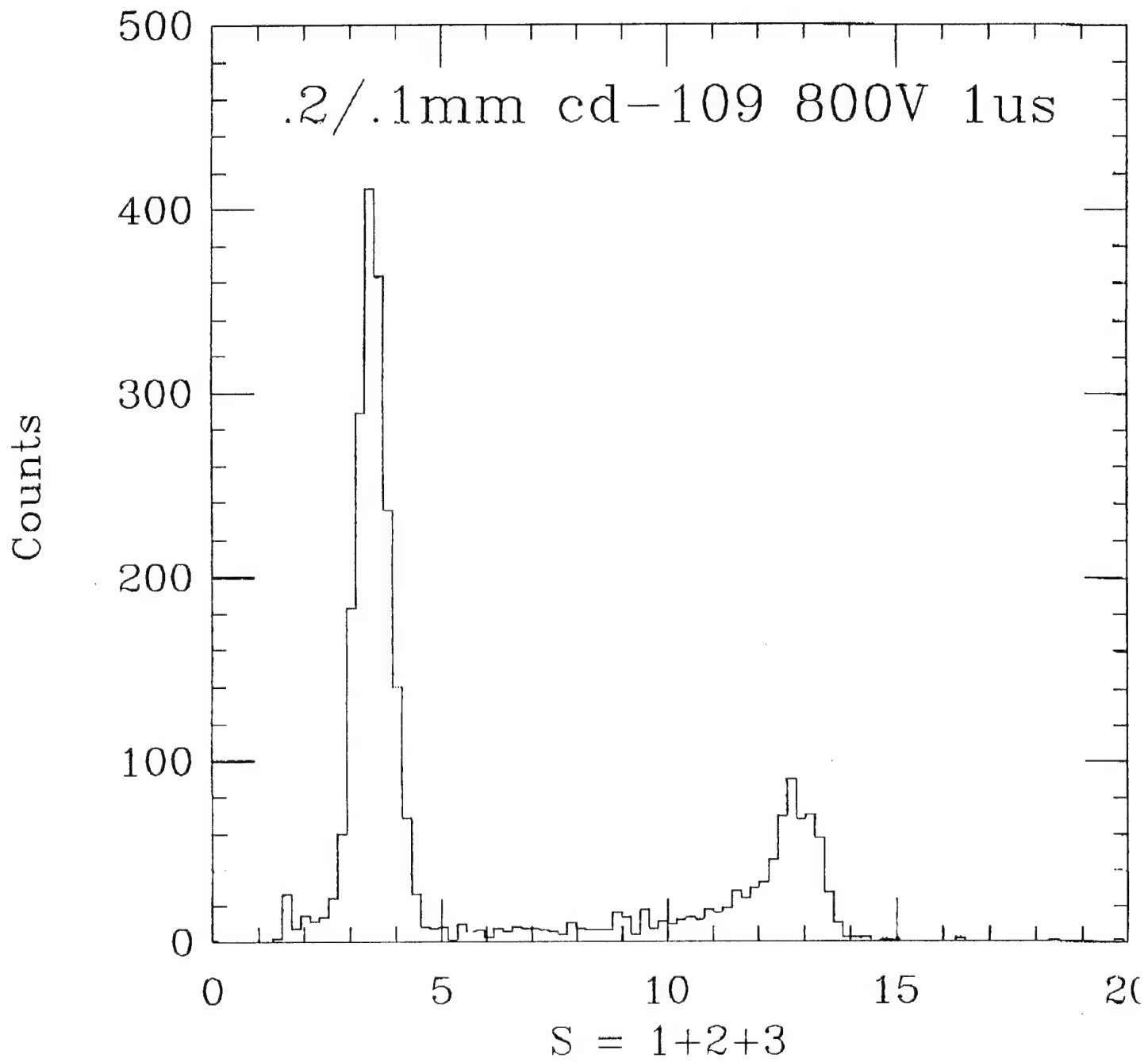


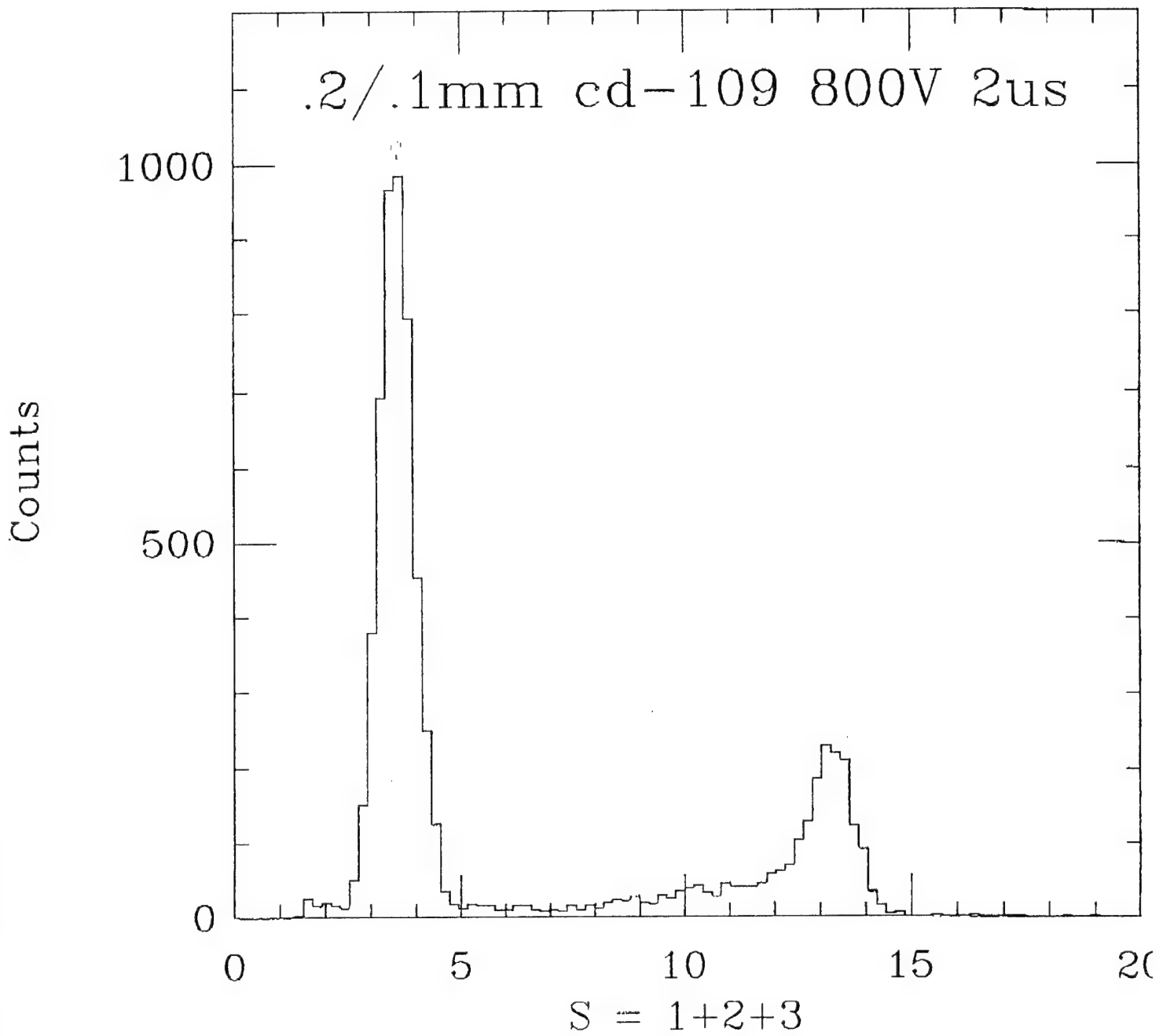


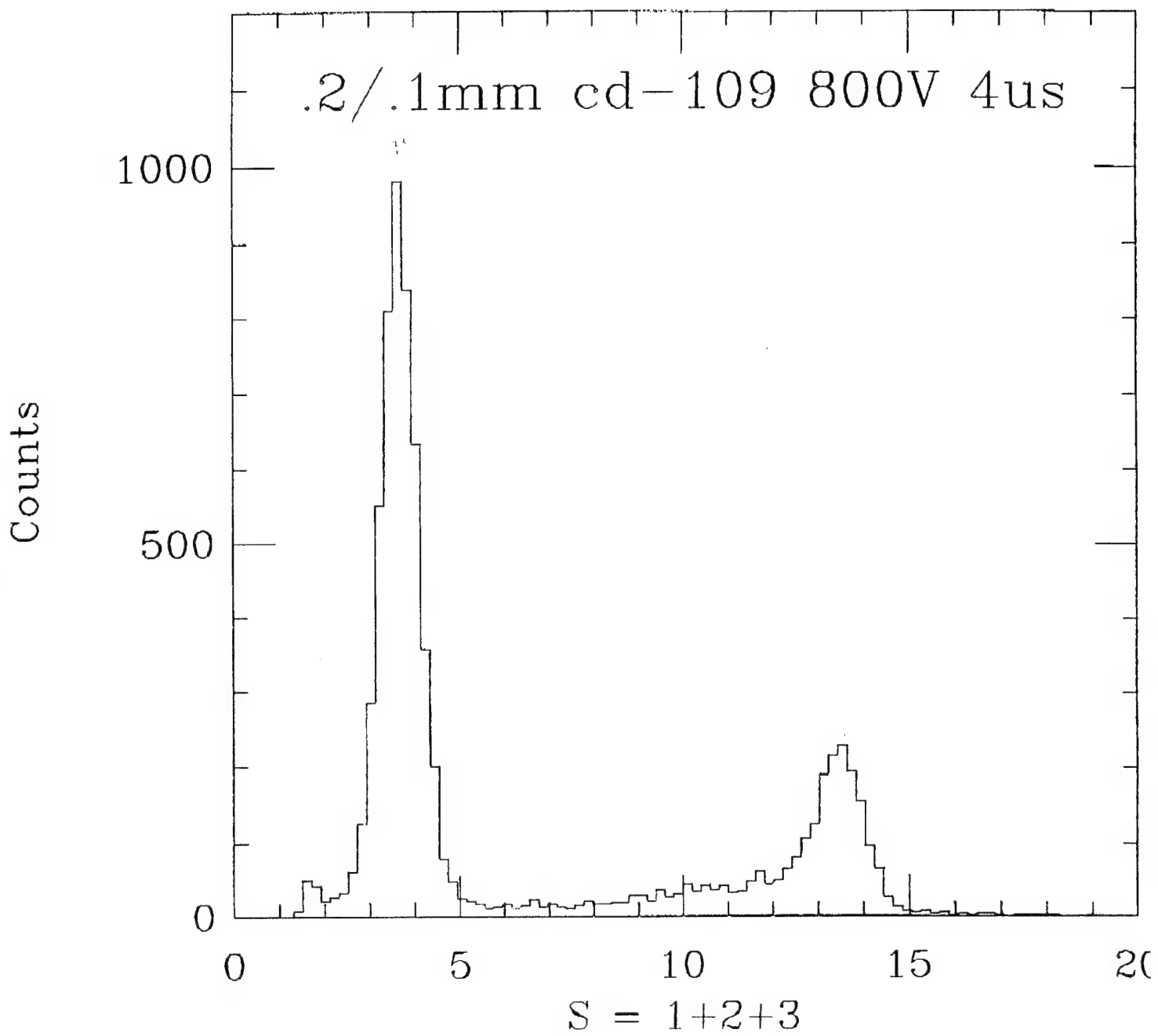
Post-it® Fax Note	7671	Date	# of pages
To	Patrick Doty	From	Paul Highe
Co/Dept.	Digirad	Co.	Wash U
Phone #		Phone	(314)935 7576
Fax #	(619)549-7714	Fax #	

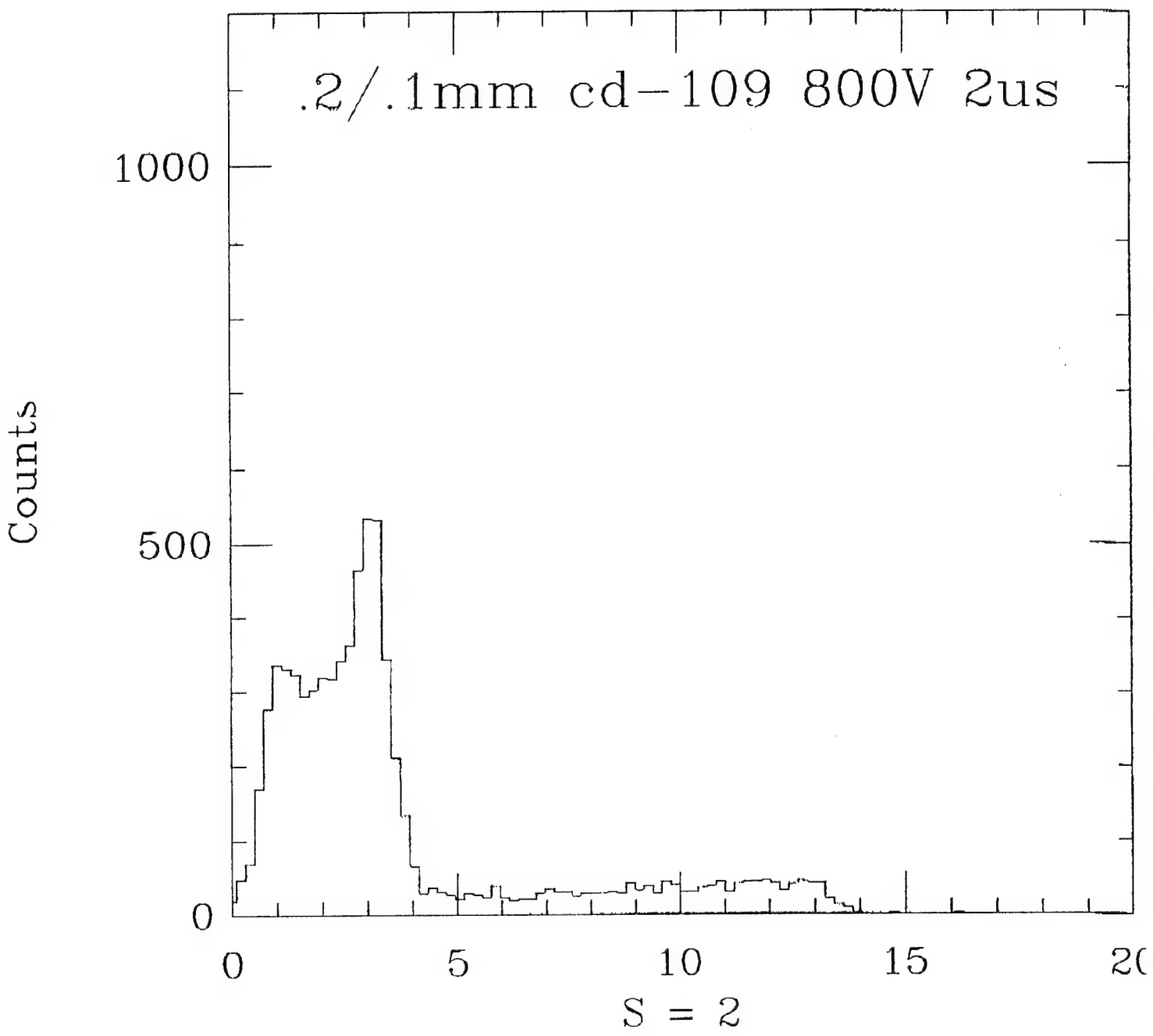


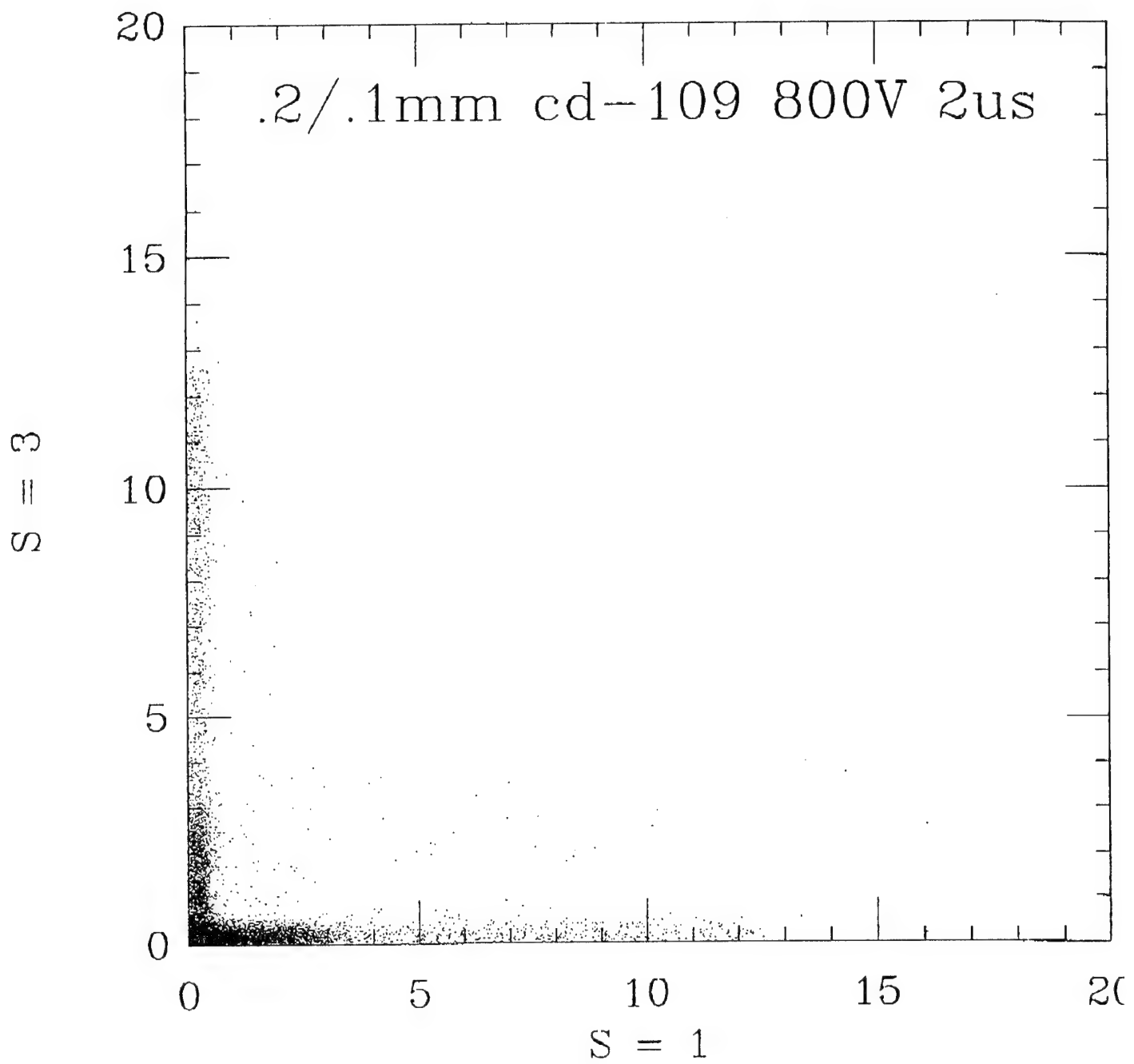


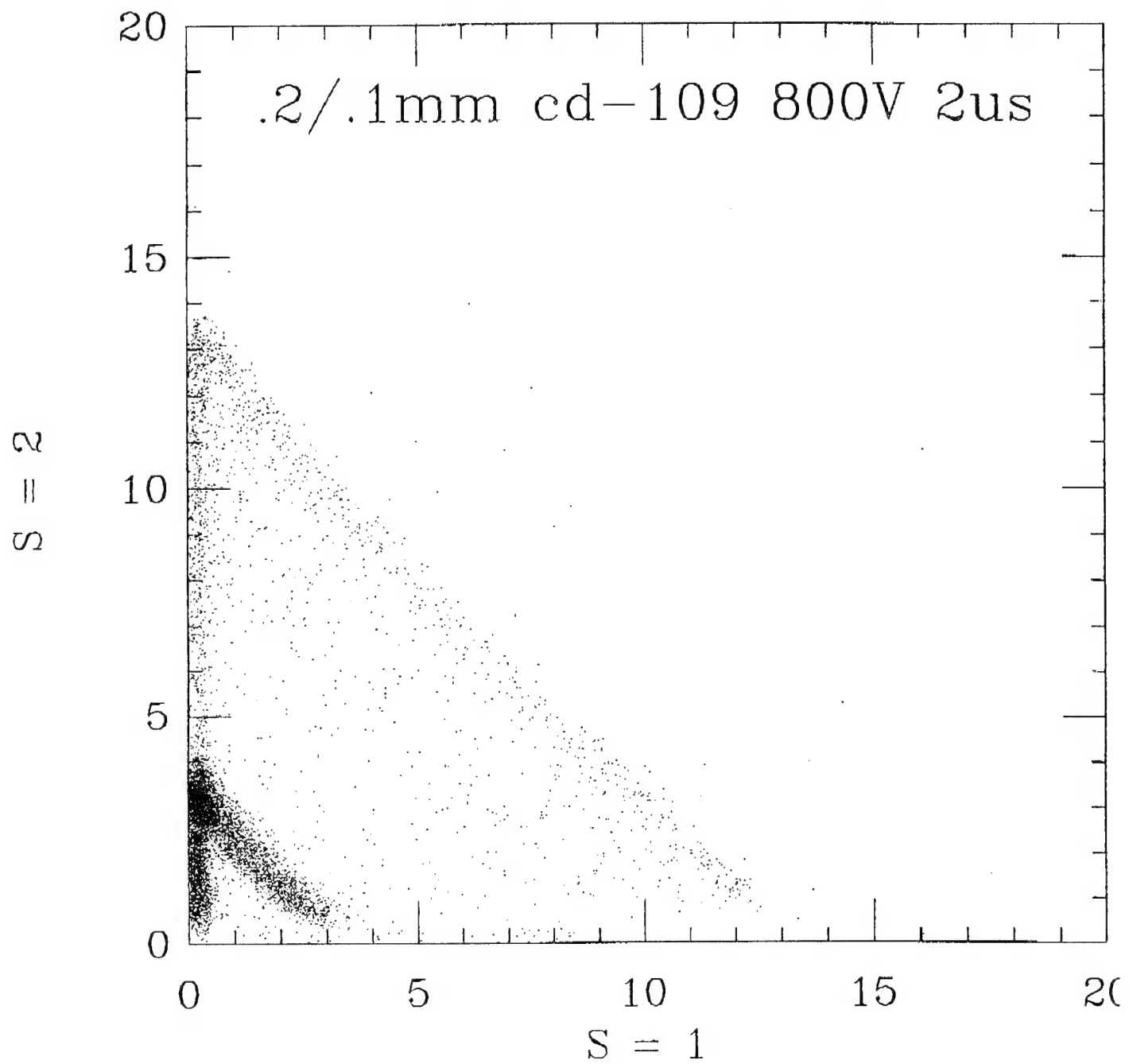


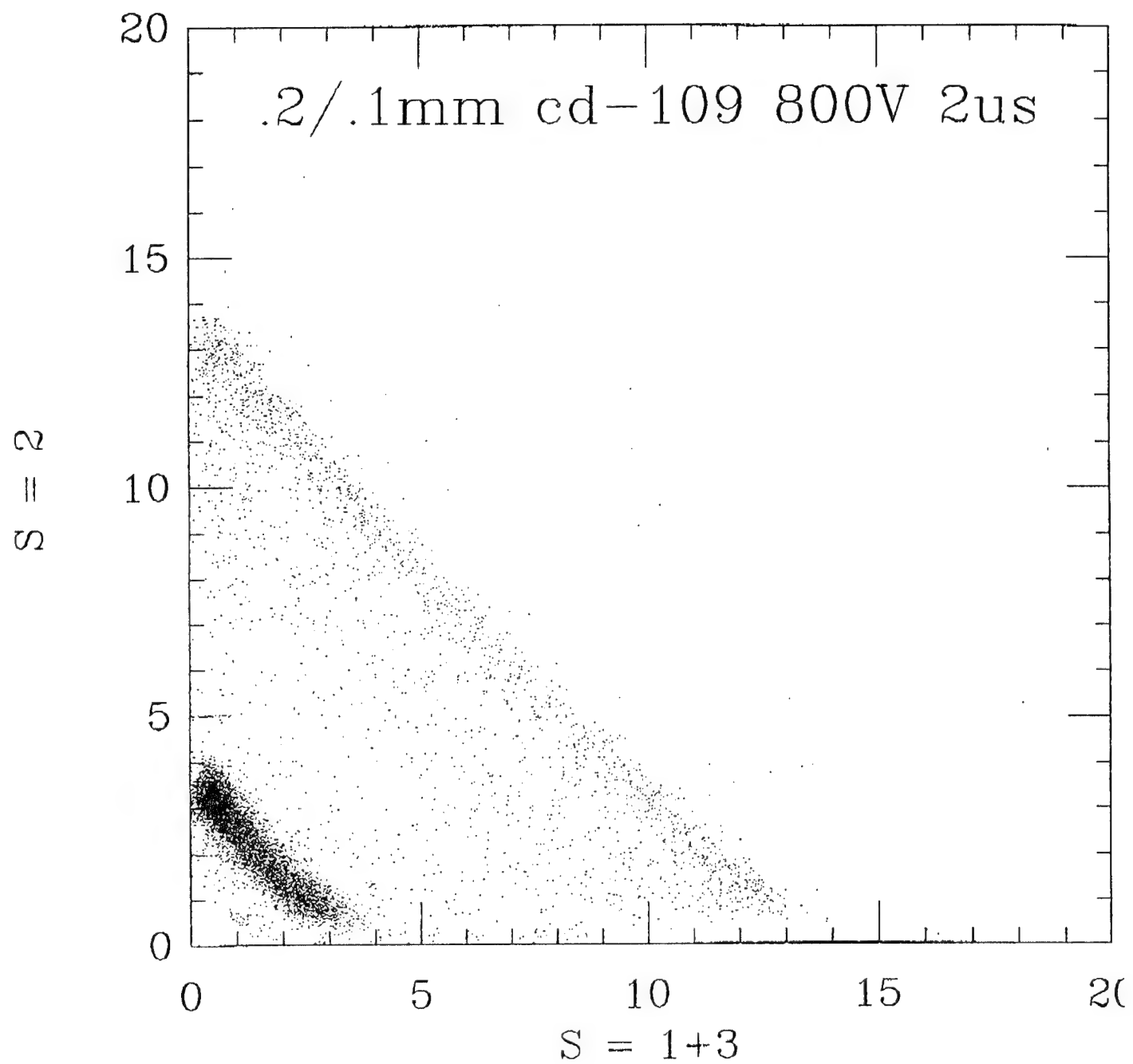


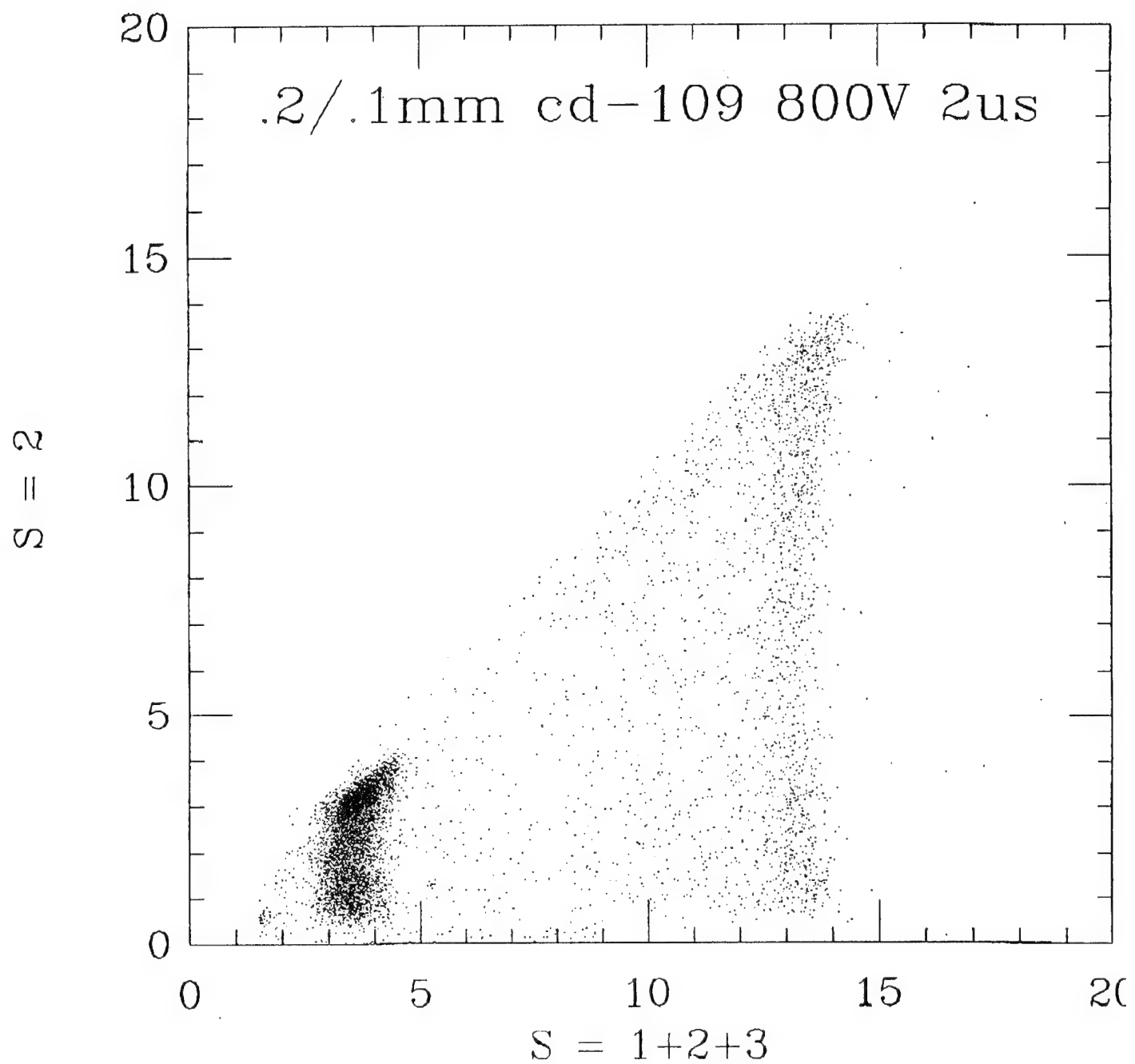


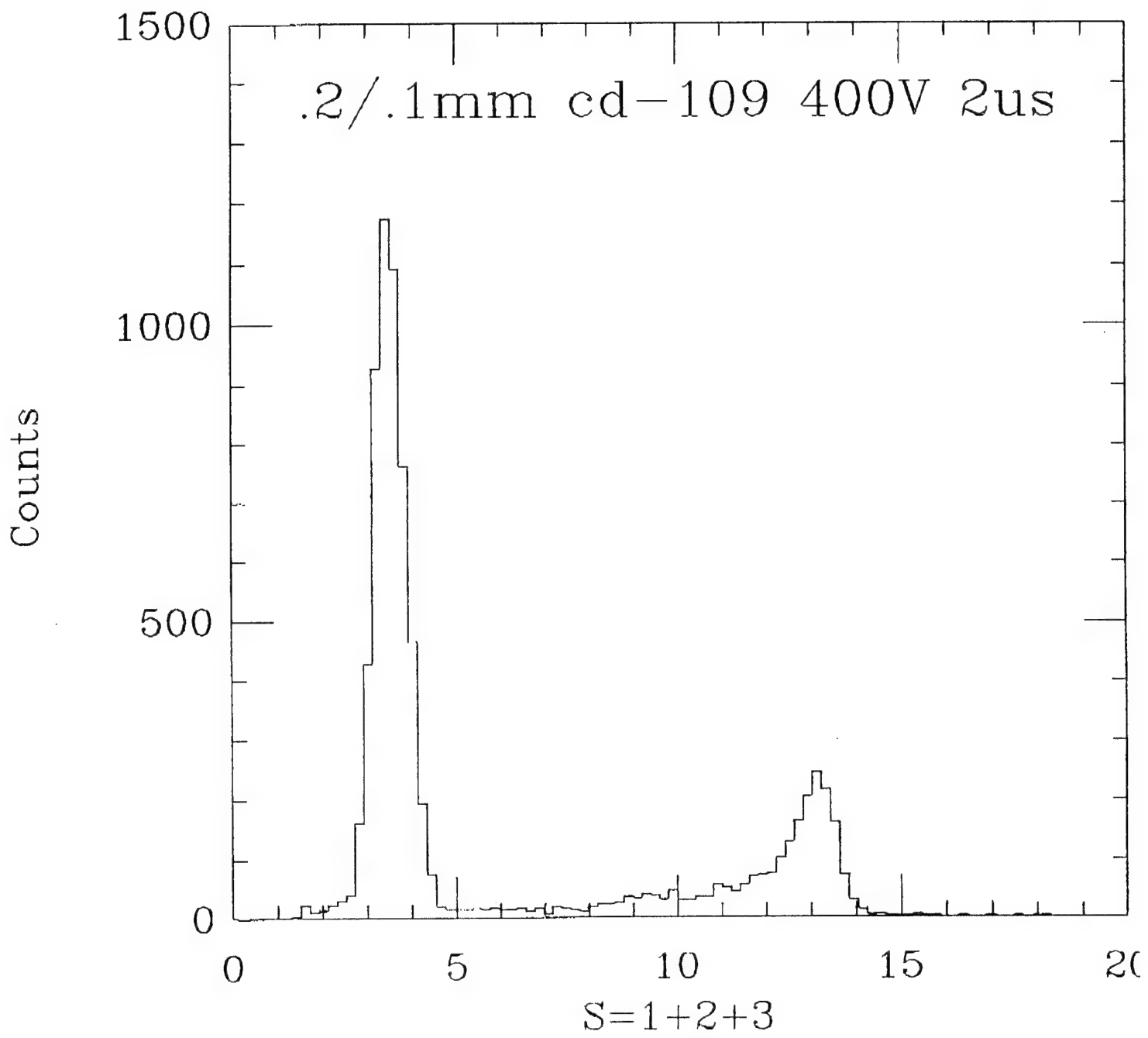


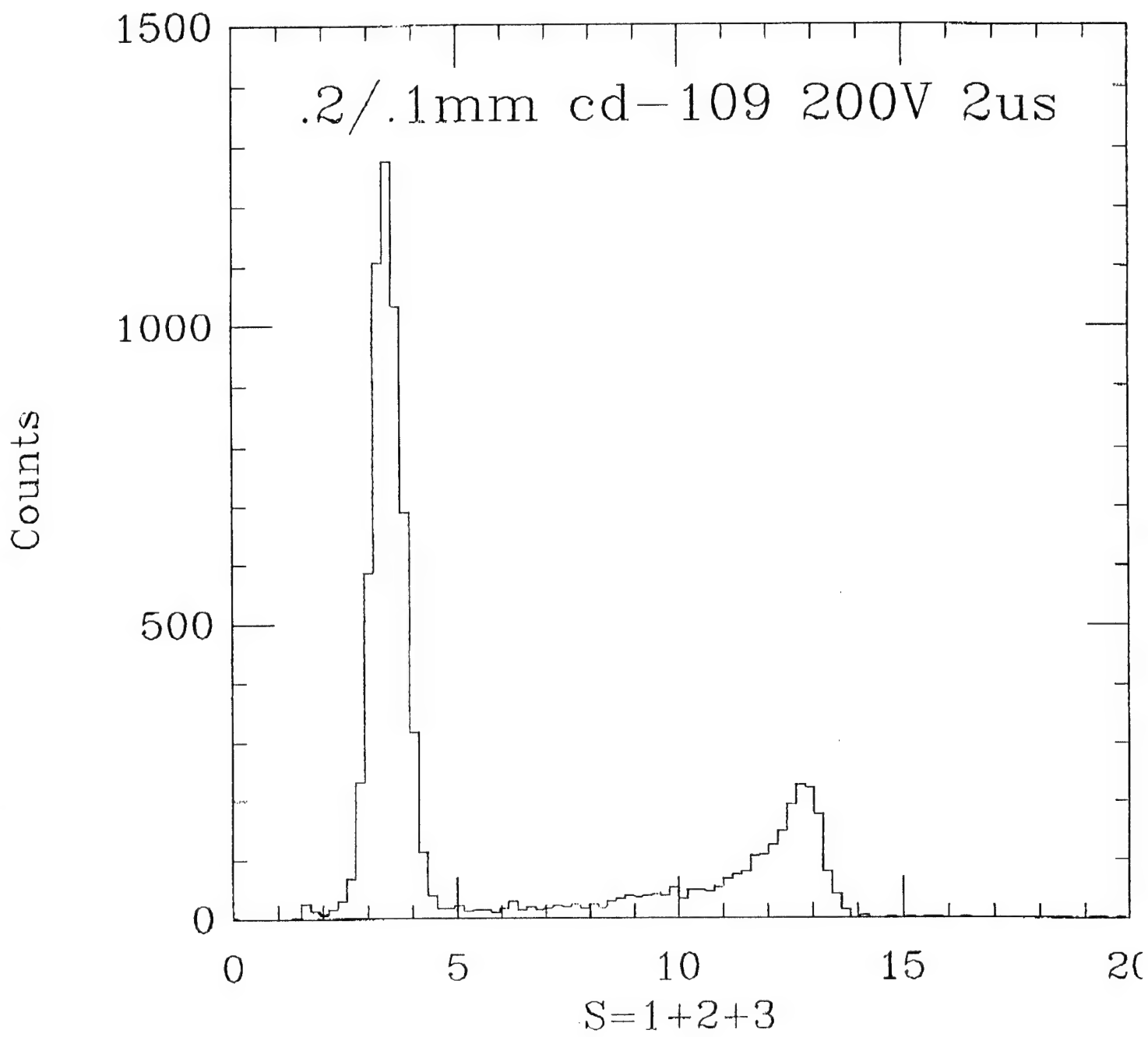


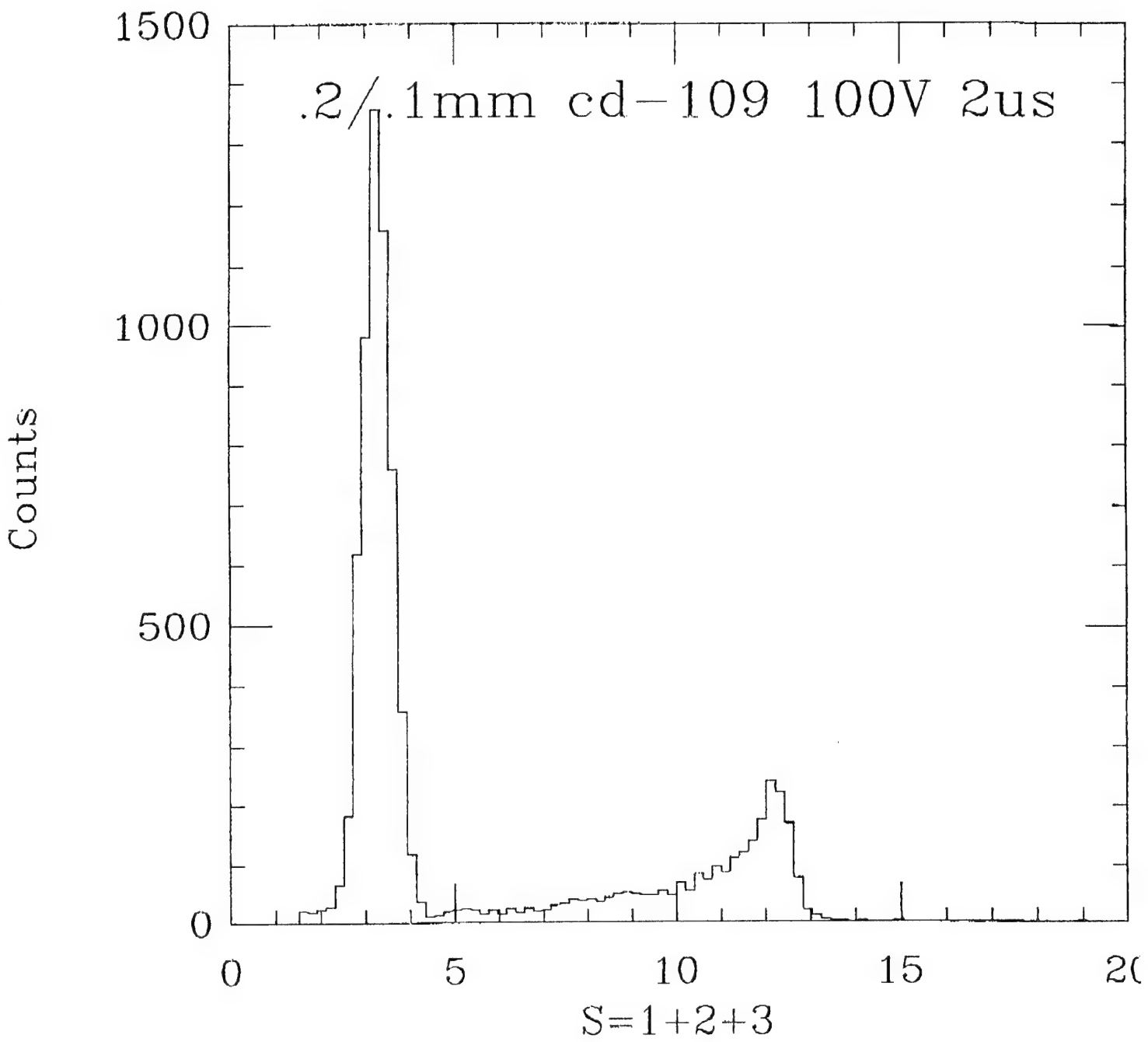


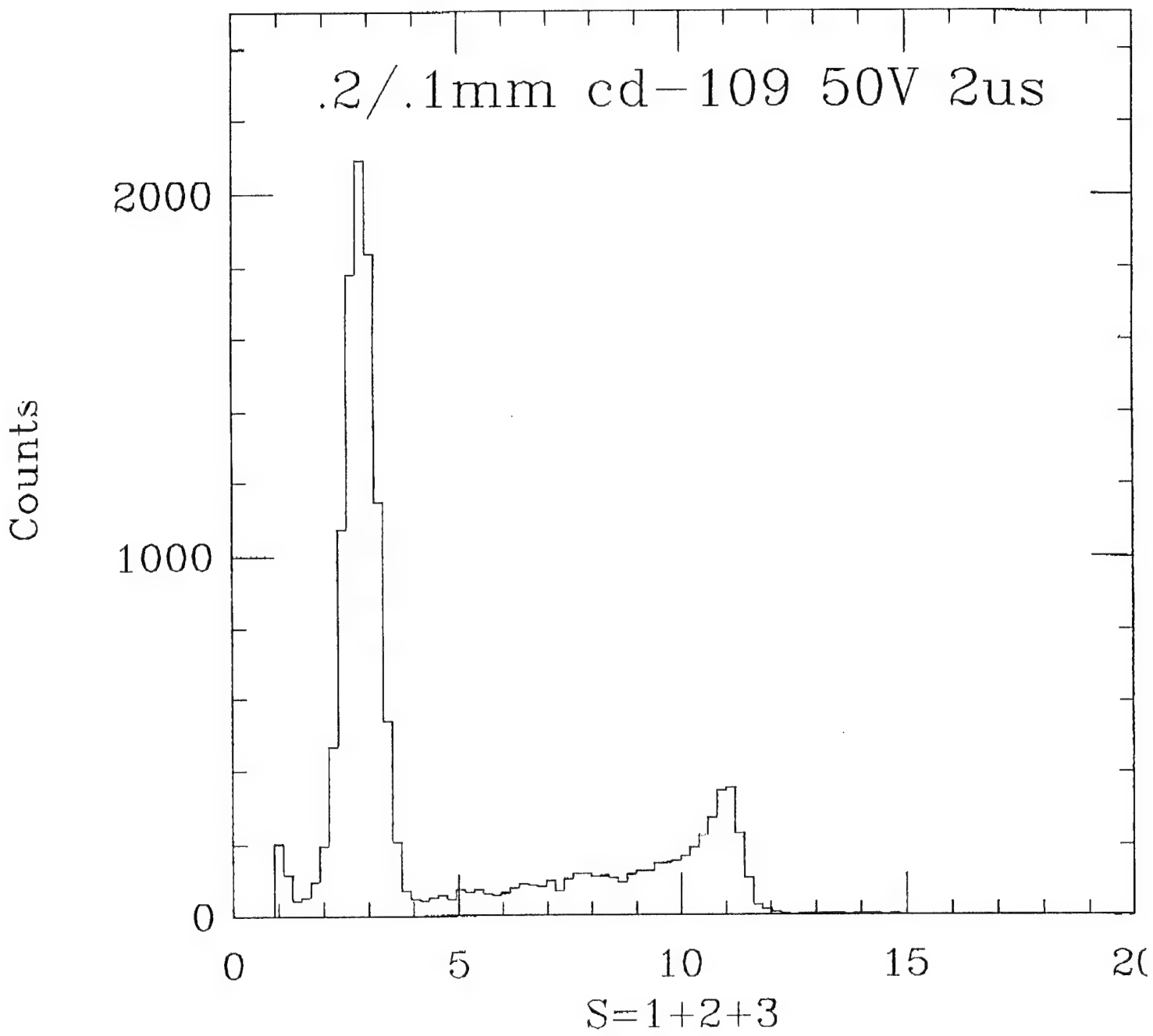


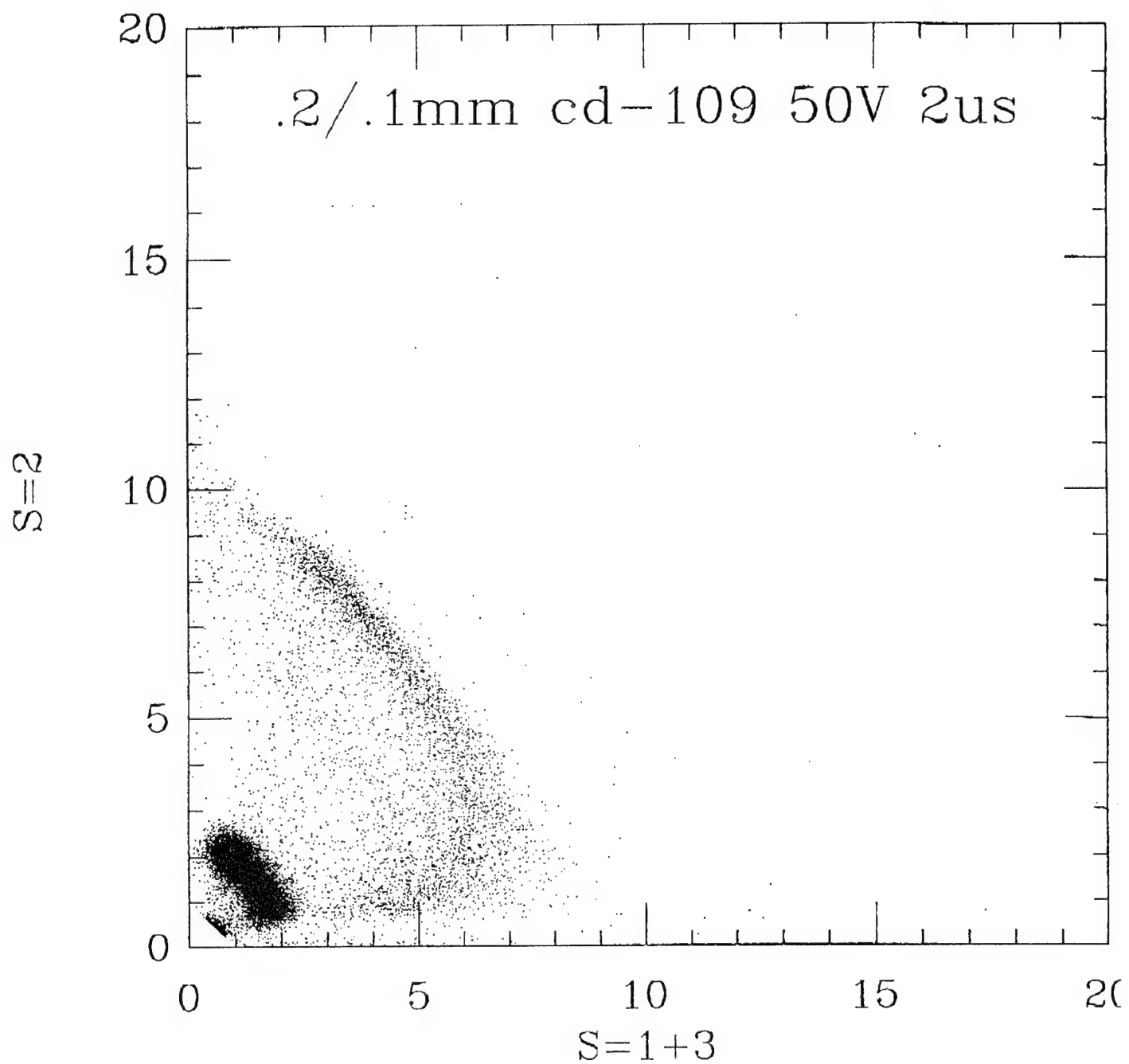


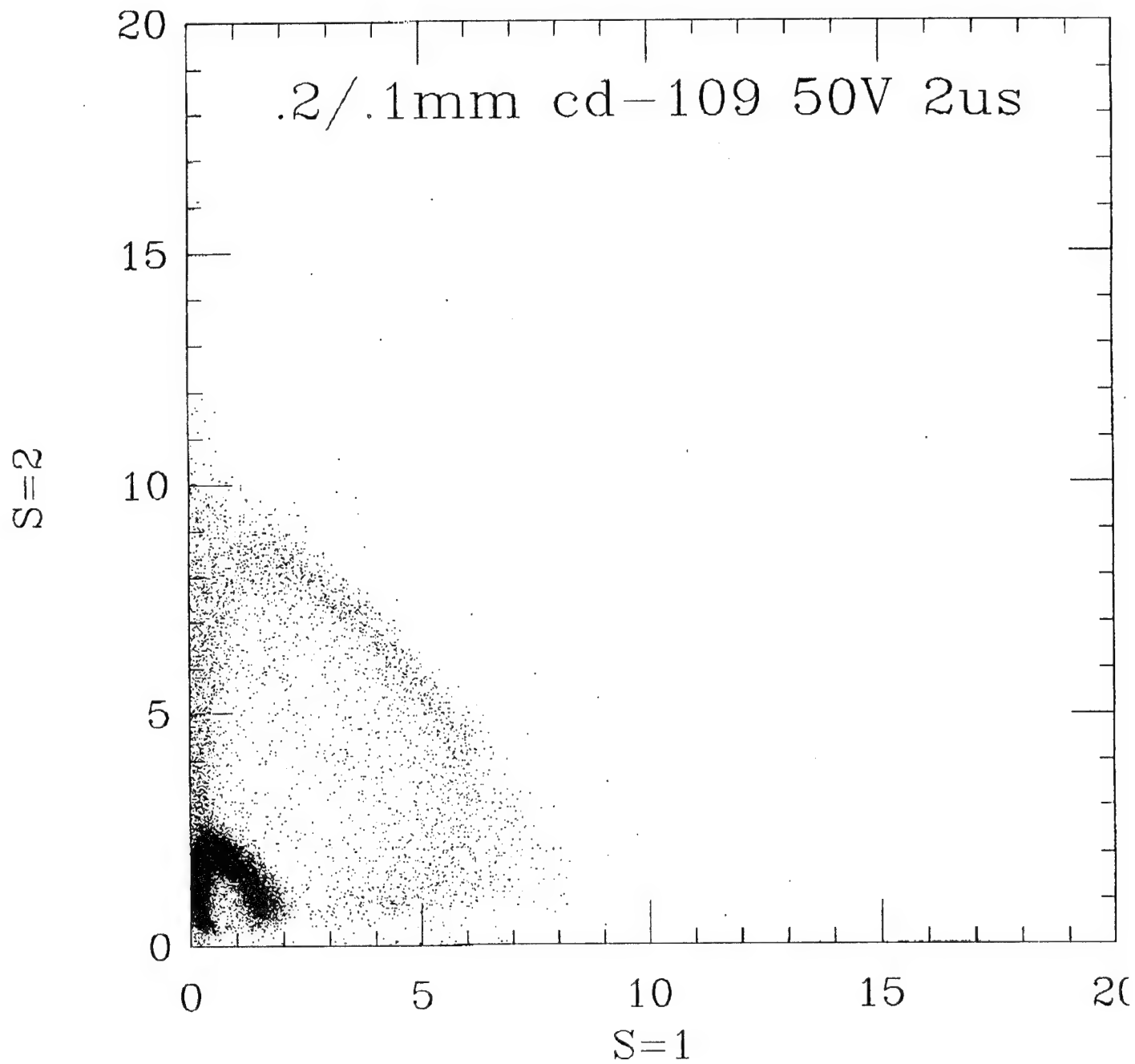


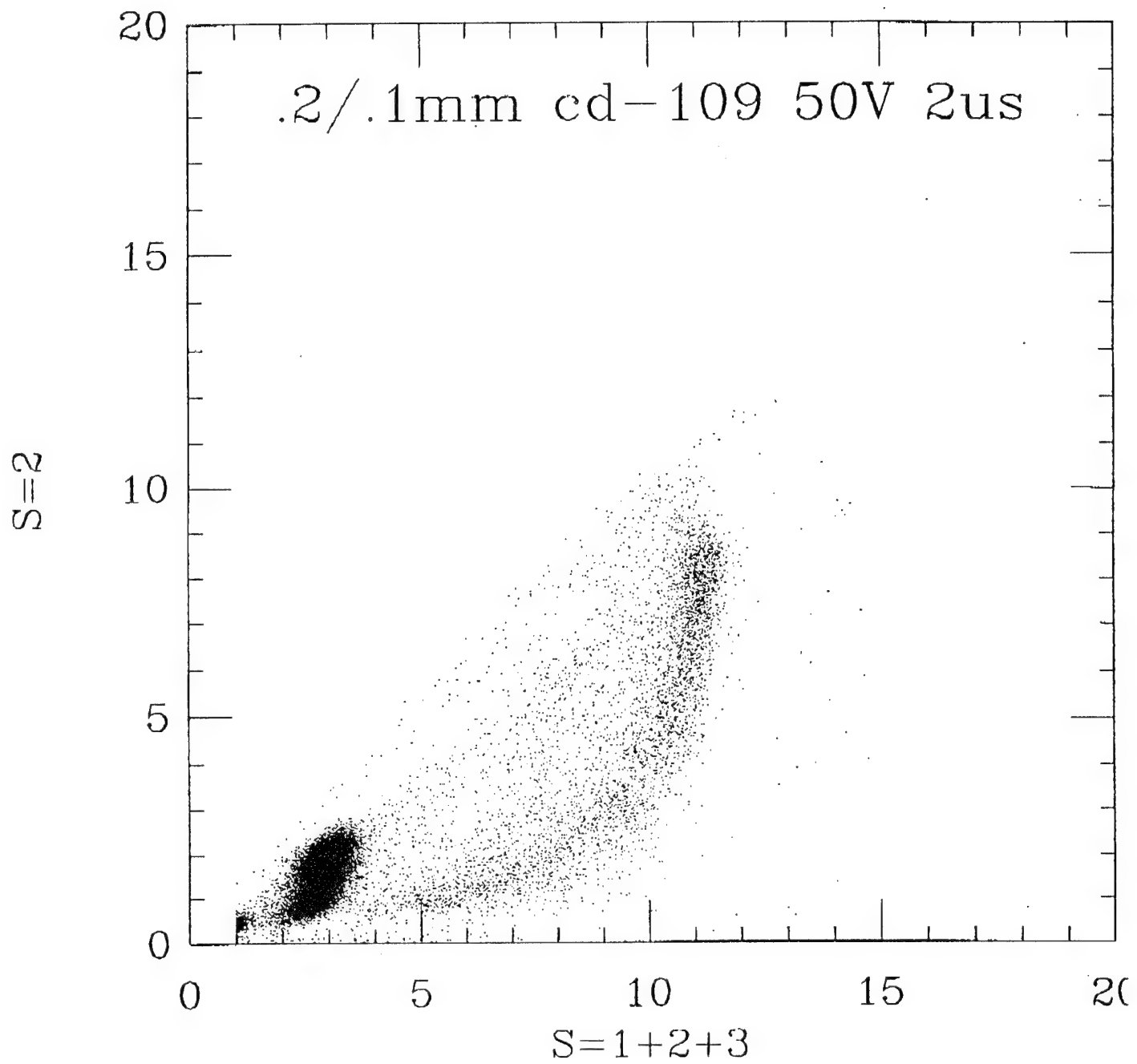


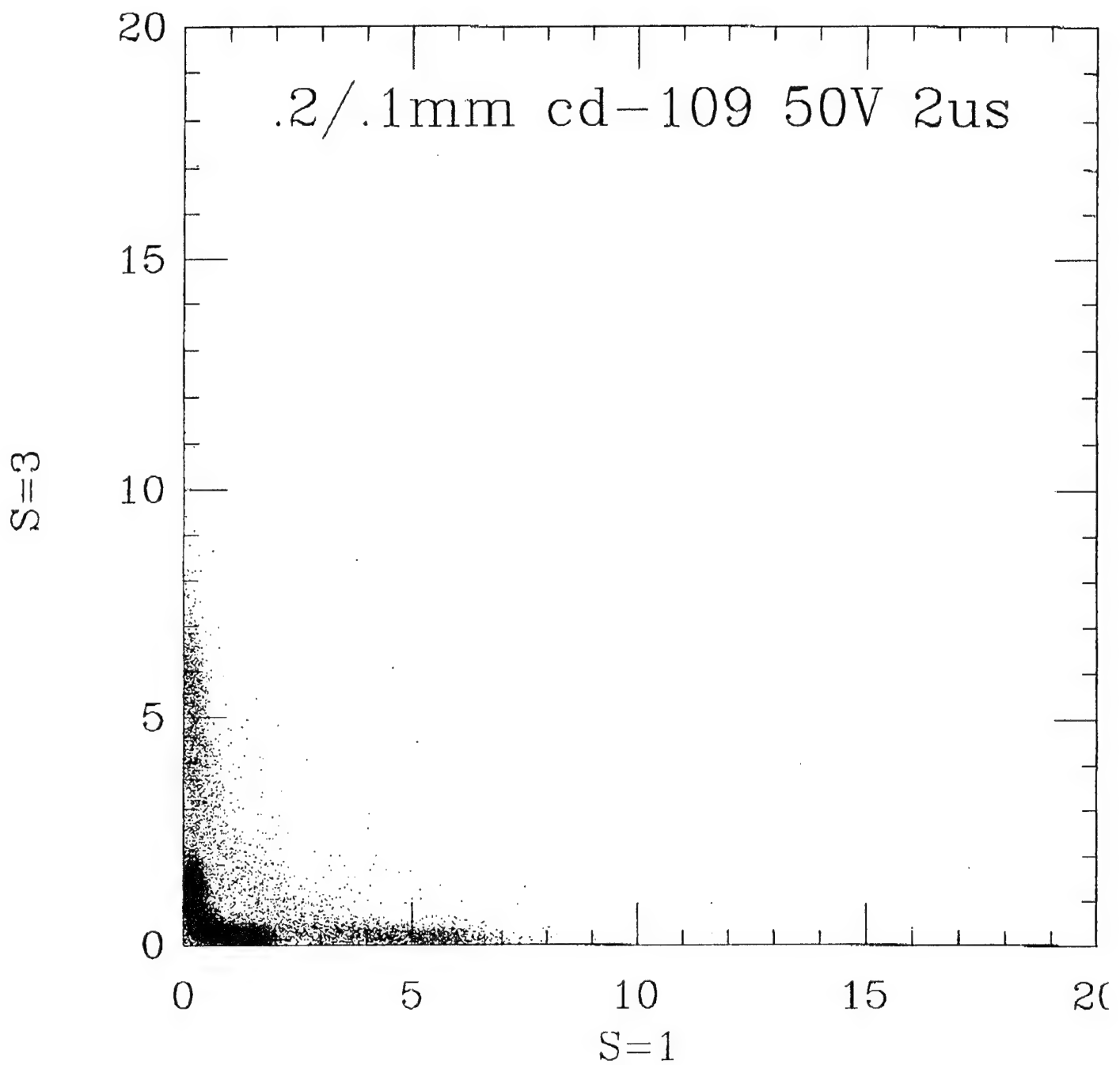












## **10. Appendix B: Commercial MUX specifications**



## MB Series

### 64, 128, and 256 Channel Amplifier-Multiplexer Array Chips

## Introduction

The RL0064/0128/0256MB family of integrated CMOS circuit chips is intended to provide flexible low-noise amplification and multiplexing components for interfacing with separate photosensitive arrays, such as gallium-arsenide, germanium or amorphous-silicon, or IR special-purpose arrays. These chips may also be used as general-purpose multi-input multiplexers for medical, scientific, or industrial instrumentation applications. These devices are available in die form. A simplified block diagram of the device is shown in Figure 1.

The various versions provide 64, 128, 256 bonding pads each with charge-sensitive preamplifiers, and the ability to sample and hold the pre-amplifier outputs (charge integrators with correlated double sampling and hold capability).

For additional application flexibility (i.e., interdigitated hybrids) both left-side bonding and right-side bonding arrangements are available, as shown on Figure 4 (see Typical Applications). The MB Series is fabricated in standard Reticon CMOS silicon gate technology, allowing dual or single supply operation. Very small photodiodes are connected to the multiplex switches for ease in testing.

## Key Features

- Left or right bond pad versions for interdigitated hybridizing
- Arrays with 64, 128, or 256 independent CMOS buffer-amplifier inputs
- Data storage and correlated double sampling
- Low noise - less than 1500 noise electrons for 1 MHz bandwidth, 15  $\mu$ V rms
- Differential output
- Variable input-amplifier reference voltage to maximize dynamic range
- 100 micrometer bond-pad spacing
- 1  $\mu$ V/100 electrons gain of pre-amplifier transducer
- Static shift-register for multiplexed clocking rate up to 5 MHz
- Low input bias current: 100 fA
- On-Chip bonding pad suitable for wire bonds or flip-chip bonds

## General Description

These multiplexer arrays eliminate many of the problems encountered in other designs. For example, the input offset level is in the low millivolt range, thus permitting operation of germanium or other types of diode arrays in a zero-bias or

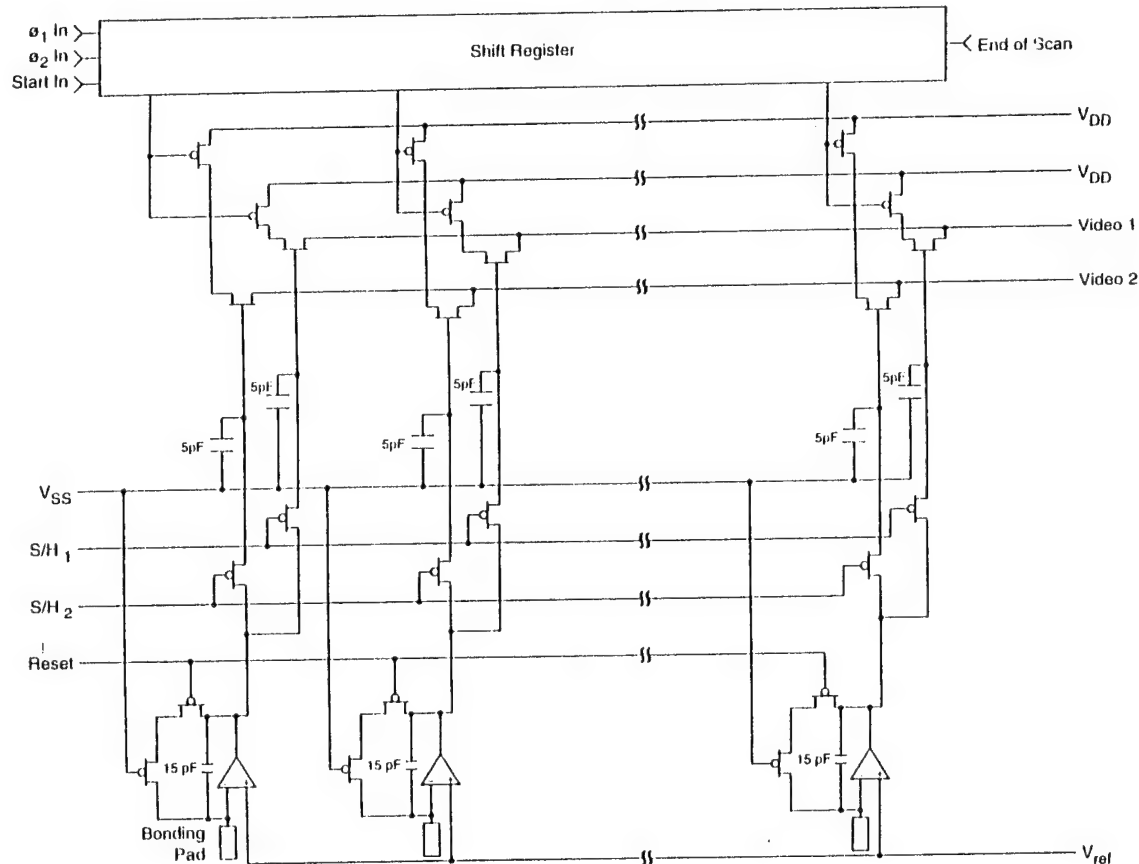


Figure 1. Simplified Block Diagram of the Multiplexer

## MB Series

photovoltaic mode, with extremely low leakage and minutes-long integration times. The correlated double sampling reduces further any leakage-caused offset as well as reducing low-frequency and switching noise. The timing of the switching of the analog buffers is derived by decimation from the multiplexer master clock, minimizing aliasing and other forms of switching noise.

### Operation

Figure 1 shows the simplified schematic diagram of the Buffered MUX. The off-chip sensors are bonded to the pads provided. Each pad is associated with a channel which can convert an input current or charge to an output voltage by using internal 15 pF feedback integration capacitors.

Switched sampling circuits follow the capacitors, they are designed to provide, along with the buffer's gain, correlated double sampling for noise and offset reduction. The stored voltage-output samples appear at the gate of source-follower pairs, each pair of samples in turn are read out sequentially, becoming the active differential output when addressed by the shift-register multiplexer.

By activating one sample and hold switch at the start of the integration time, the other to end the integration, as shown in the timing diagrams of Figure 2, one of the sampled pair of data pulses contains any noise which may have occurred on the signal, the other contains any noise on the signal as well as the integrated and converted optical signal. The pair of pulses can be differentially combined to subtract off the noise which may have occurred.

A start pulse is required to initiate the scan (see start pulse specification). Upon entry of the start pulse, the stored voltage output samples are sequentially interrogated, under control of a static shift register, through the amplifier multiplex switches as the loaded bit is clocked down the shift register. An End-Of-Scan (EOS) signal occurs at the termination of each scan.

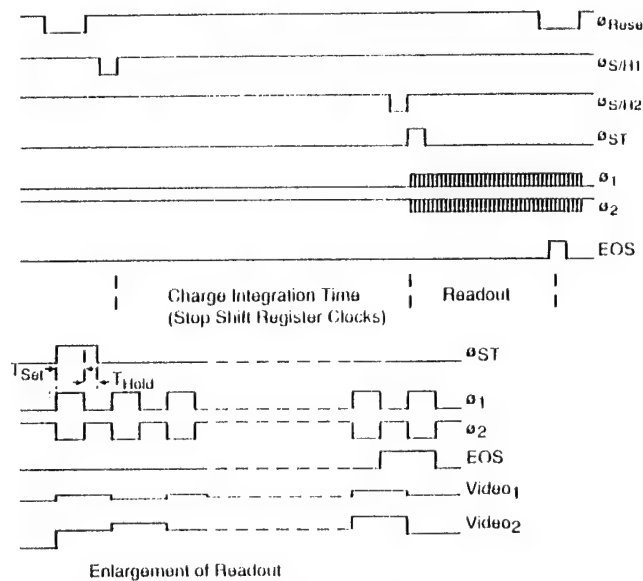


Figure 2. General MB Series Timing Diagram

Reset switches are provided on each video for use in signal processing (see Typical Application).

The RL0064/0128/0256MB series is designed to operate with either a single-ended +5 to +10V supply, or with split supplies in the range of 5 to 10V total ( $\pm 2.5$  to  $\pm 5$ ). The channel inputs should be operated within 1V of either rail. Logic inputs are active-low and should swing rail to rail. Because of the various power-supply configurations, and the necessity for full-range swing, these logic inputs typically require external interface elements if combined with TTL logic elements.

The photodiode sites, indicated in Figure 1, are used for testing. They are in parallel with a sensor pad, each represents a capacitance of .1 pF. Figure 2 depicts the general I/O timing requirements for the multiplexer family, the detailed clock specifications and timing are covered under Clock, Start, and, EOS Specifications. Figure 3 shows a typical measured noise versus frequency characteristic for the devices. Figure 4 shows the pinout arrangements, Figure 5 shows the bond pad dimensions, and Figure 6 shows a simple clock drive circuit.

The total output noise measured at each S/H source follower output is less than 15  $\mu$ V rms with a 1MHz bandwidth. When a detector is connected to the input pads, the equivalent output noise will be about 15 times the gain of the detector and multiplexer, or  $15X(1+C_{det} \text{ pF}/15 \text{ pF}) \mu$ V rms for each respective channel.

### Electrical Specifications

#### 1. Static Shift Register Clocks $\phi_1$ and $\phi_2$

These clocks operate the shift register. For optimum multiplexer operation the clocks should not overlap, if the application requires clock overlap, they should not overlap by more than 50%. Since the shift register is static the clock rise (tr) and fall (tf) times are not as critical as with a dynamic shift register.

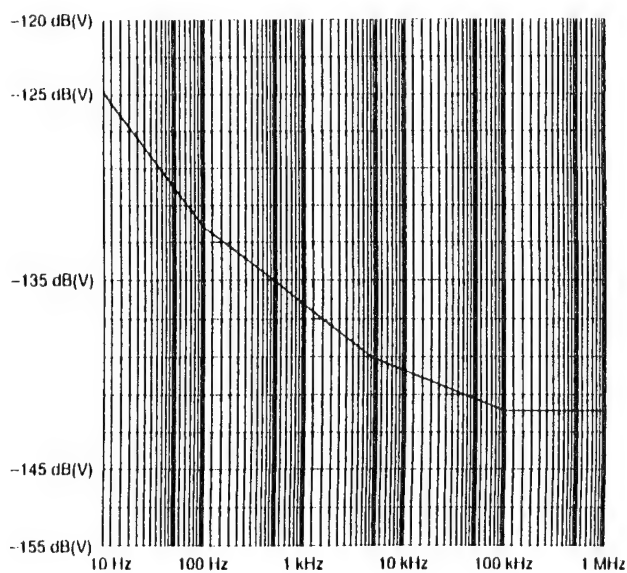


Figure 3. Noise Spectrum Density of the Preamplifier and Source Follower

## 2. Start Pulse ( $\phi_{SI}$ )

The start pulse loads the shift register with a voltage pulse to initiate the scanning process. It loads the register on each  $\phi_1$  high to low (positive to negative) transition as long as the start pulse is held high. Therefore to ensure that only one bit is loaded, the start pulse should be high during only one  $\phi_1$  falling edge. Figure 2 illustrates the timing relationship with respect to  $\phi_1$ . The clock amplitude of  $\phi_{SI}$  should be similar to the static shift register clocks ( $\phi_1$  and  $\phi_2$ ). The setup time ( $t_{SE}$ ) should be at least 30 ns, the hold time at least 20 ns.

Note: The shift register will load multiple bits if the start pulse is high for more than one  $\phi_1$  falling edge.

## 3. End of Scan (EOS)

The EOS pulse is generated at the output of the shift register to mark the termination of the scan. The last position accessed with the  $\phi_2$  clock going positive. On the next  $\phi_1$  falling edge, the output pulse is applied to the gate of the EOS transistor.

## 4. Sample and Hold (S/H1, S/H2)

The two sample and hold gates are used to facilitate the double correlated sampling. Each pair of gates are linked to one bonding pad then split to each of the video outputs. The circuit design for each sample and hold pair of gates are duplicates (see Figure 1). By sampling one gate immediate preceding the integration of the image and sampling the other to signify the end of the integration (immediately preceding the start pulse), a simple differential circuit as shown in Figure 7 would provide the user with a signal which contains only the integrated signal since all switching noise would have been subtracted out.

## 5. Bias

Bias is used to bias the operational amplifier, and should be connected to  $V_{SS}$  through a  $100K\Omega$  resistor in series.

## Typical Application

Figure 8 shows the interdigitated application of the mirrored devices where both left and right side devices are used with an array of sensor diodes. All three chips are bonded in a hybrid substrate, the pads bonded as shown. The clock inputs and video outputs are then bonded either to another dice on the substrate, or to pin connections on a package to accommodate inputs and outputs for the clocks and the video. In this particular application photodiodes are accessed by using two devices, one for accessing the even numbered diodes, and the other for the odd numbered diodes in the array. When the multiplexers are scanned, integrated-image charges will appear in sequence at the output, each one proportional to the light exposure at a given site.

Reset switches are provided for use in signal processing. They can be used to integrate signal charges on a capacitor (i.e., the video line capacitor or an external capacitor) then used to reset the capacitor after each multiplex site has been read out (see Figure 2).

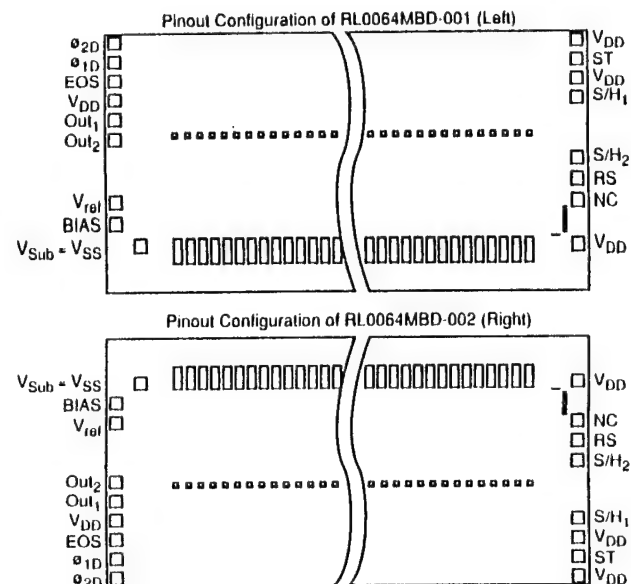


Figure 4. Pinout Configurations

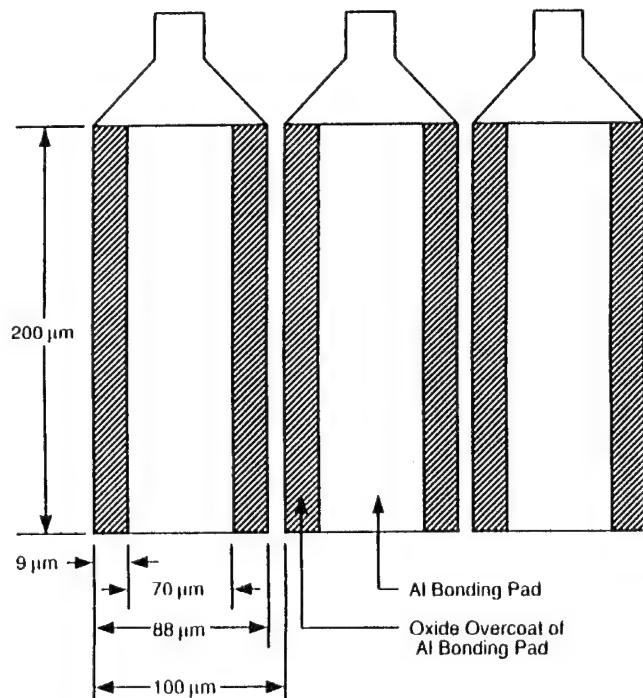


Figure 5. Switch Connection Bonding Pads

## MB Series

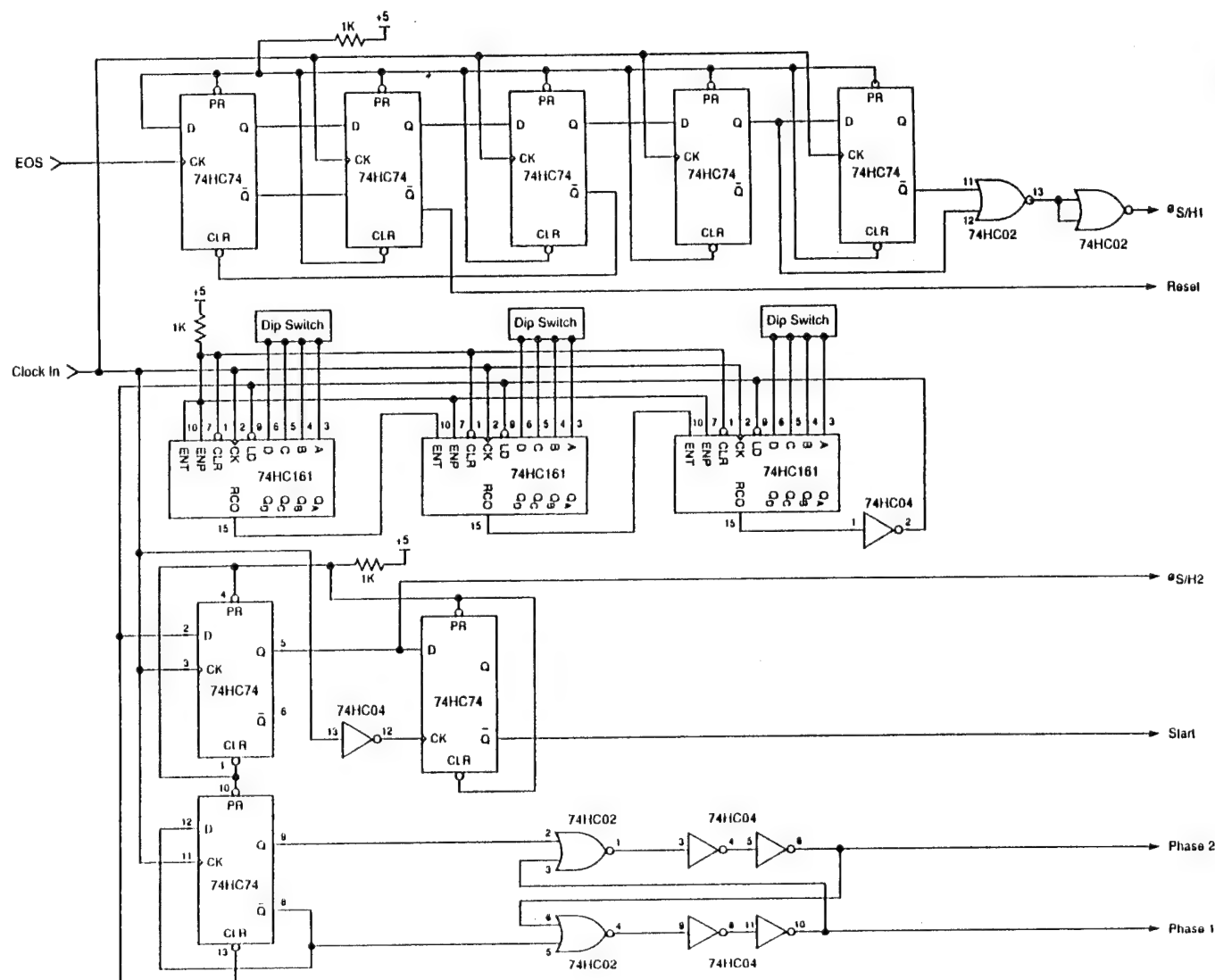


Figure 6. Simple Clock Drive Circuit

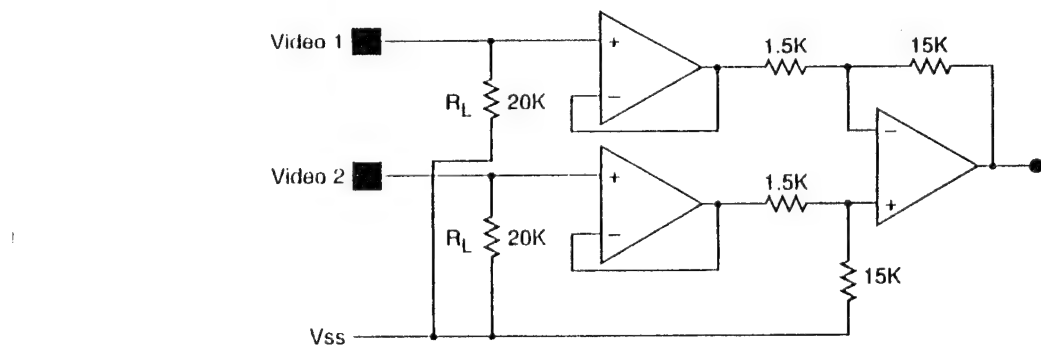


Figure 7. Differential to Single Video Output

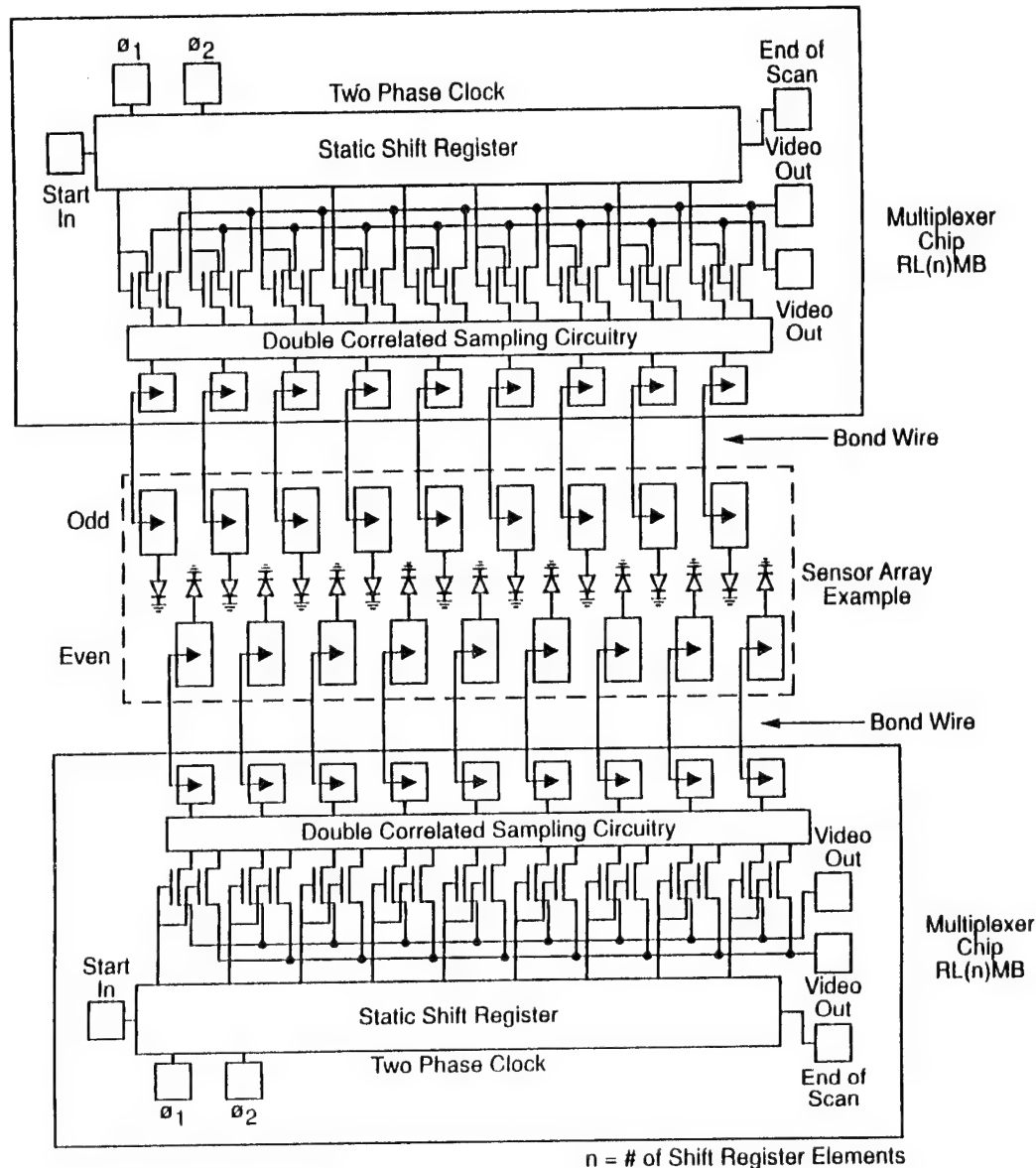


Figure 8. Interdigitated Array Using Left and Right MB Series Multiplexers

## **MB Series**

---

**055-0343**  
**October 1993**

## **11. Appendix C: Focused Collimator**

# Three-dimensional Endocardial Mapping System Using a Novel X-ray Imager and Locating Catheter

Jack W. Moonman, MS, Robert E. Melen, PhD, Brian Skillicorn, BEng,  
and Edward G. Solomon, MS

**Abstract:** Percutaneous radiofrequency catheter ablation (RFCA) has a very high success rate for certain arrhythmias, such as Wolff-Parkinson-White syndrome and idiopathic ventricular tachycardias in the right ventricular outflow tract. These arrhythmias are typically characterized by a single site of arrhythmogenic tissue that is well bounded by anatomic markers. Success rates for RFCA for reentrant ventricular tachycardias, tachycardias not closely associated with anatomic markers, and those having larger tissue areas requiring multiple overlapping lesions have been significantly lower. An endocardial mapping system is being developed that includes a fluoroscopic imager that scans the field of view with a series of small x-ray beams and electrophysiology catheters modified to include miniature x-ray sensor elements. Preliminary work indicates that the accuracy of determining the mapping catheter location relative to the reference catheters will be  $\pm 1.5$  mm. Substituting a highly accurate three-dimensional coordinate system for anatomic markers could improve the success rate of RFCA for complex arrhythmias. **Key words:** endocardial mapping, arrhythmia, electrophysiology, x-ray, catheter, locating.

One reason for the efficacy of RFCA is the ease of control

of lesion formation. However, the relatively small lesion size has resulted in demands for the ultraprecise targeting of the ablation sites by the catheter and has prevented clinicians from achieving a high success rate in the ablation of arrhythmias such as fibrillation and atrial tachycardia and

Finally, there is the condition of bilateral adnexal tumor, the tumor being bounded anatomically<sup>10</sup> and where only one lesion is required for the therapy.

Current catheter technology is considered primitive,<sup>11</sup> with bending accomplished by actuating pull wires and steering accomplished through pushing, pulling, or rotating the catheter while actuating it. The determination of a catheter's location is based on the view seen on a fluoroscopic monitor by the operator and inspection of the electrograms. For intracardiac mapping, the typical procedure is to estimate the location from the monitor<sup>12</sup> and manually mark it on a sketch of the heart.<sup>13-16</sup>

From Cardiac Mariners, Los Gatos, California.

*From Cardiac Mariners, Los Gatos, California.*  
Reprint requests: Jack W. Moorman, Cardiac Mariners, 120-B  
Albright Way, Los Gatos, CA 95030.

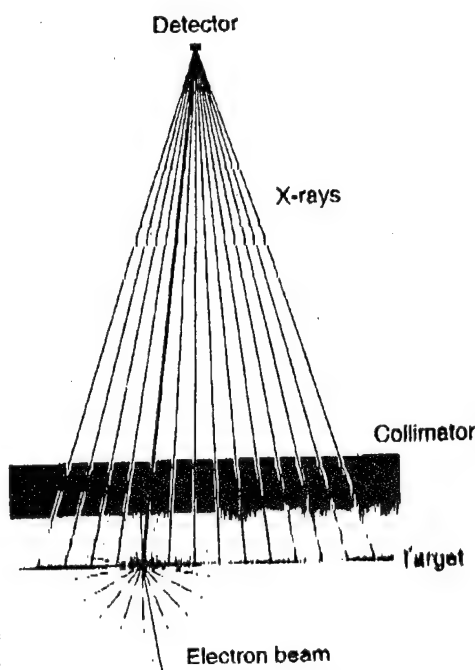


Fig. 3. Scanning beam x-ray source.

for each to point toward the detector that is 91.4 cm away from the collimator.

Figure 4 shows how the x-ray beams diverge from each collimator hole. If the object to be imaged is placed close to the collimator, the spatial resolution will depend on the collimator hole pitch, focal spot size, and detector size. If the object being imaged has substantial thickness and therefore cannot be located close to the collimator, spatial

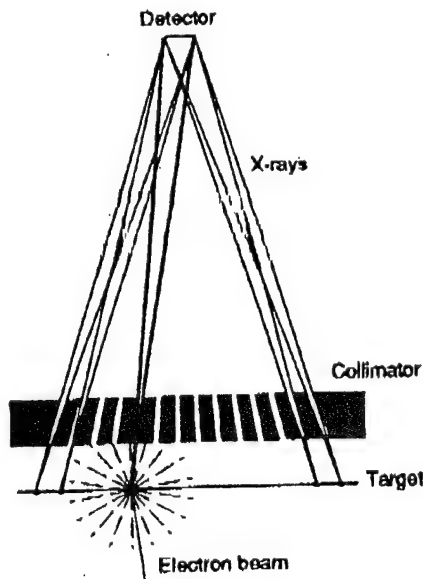


Fig. 4. Beam divergence through collimator holes.

resolution will be reduced because of the beam divergence and beam overlap shown in Figure 4. Spatial resolution at a distance from the collimator could be maintained by making the detector diameter (and collimator holes) smaller so that beam divergence was sufficiently small for a short distance close to the collimator where the object being imaged was located.

Unfortunately, this method of maintaining spatial resolution has a large effect on the overall system. For example, if the detector diameter is halved, the beam divergence is halved, but the x-ray flux measured by the detector is reduced fourfold. This square-law reduction in flux for reducing beam divergence necessitates substantially higher-power x-ray sources and/or substantially longer imaging times to yield sufficient x-ray flux to produce the required image quality. This problem has, until now, made scanning-beam systems impractical for medical applications.

The collimator holes of the SBDX system have a 0.38-

mm width to eliminate beam divergence, but instead of a single detector, the SBDX system uses a two-dimensional array of small detectors (Fig. 5) to break each beam emerging from a collimator hole into an array of smaller subbeams. The outputs from the detector elements are summed in a mathematical reconstruction algorithm shown graphically in Figure 6, using all the x-ray energy incident on the detector array to produce an image that has the spatial resolution corresponding to a single subbeam.

The array used in the SBDX is made up of 96 detectors, comprising the circular center section of a 12 × 12 rectangular array. This 96-element array allows the SBDX source to collect sufficient x-ray flux to produce images at a 30-Hz frame rate.

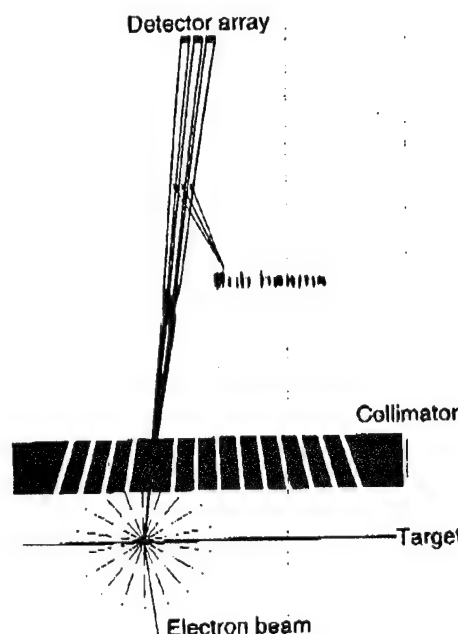


Fig. 5. Detector array preserves spatial resolution by breaking a beam into small subbeams.

The time required for mapping procedures also tends to increase with complexity. An angiography procedure may have a range of 1–20 minutes (mean, 5.4 minutes; median, 4.7 minutes) of fluoroscopy time,<sup>17,18</sup> whereas a supraventricular tachycardia (SVT) catheter ablation requires an average of 22–44 minutes<sup>19,20</sup> or up to 10 times more fluoroscopy time. More difficult SVT ablations and the more complex ventricular ablations have much longer fluoroscopy times yet, with up to 150 minutes being reported,<sup>12,19,21</sup> or 30 times the average angiography procedure. These long procedures represent a radiation safety risk to both patients and medical staff.<sup>22–27</sup>

It has been proposed to use eggbeaters,<sup>28</sup> baskets,<sup>29</sup> balloons, or plaques to provide multinodal data, such as is acquired during surgery.<sup>30,31</sup> These multinodal networks must overcome substantial objections to be acceptable. First, the deployable array must be safely retractable to remove it after the procedure.<sup>13</sup> Second, the array must be sufficiently dense to give data from points that are within a few millimeters of each other. Third, the array must have sufficiently large electrodes to perform the ablation or be sufficiently porous to allow an ablation source to pass through it. Fourth, the array must be large enough or maneuverable enough to cover large areas of the myocardium. Fifth, the array must be flexible enough to match the complex loops of the myocardium, including papillary muscles.

An alternative approach is one in which the fluoroscopy biplane images, gated to the cardiac cycle, are processed using pattern recognition to calculate a location. Motion artifacts due to the respiratory cycle and patient movement must be taken into account. Prior work by Saxon et al.<sup>32</sup> and Langberg et al.<sup>33</sup> suggests that the locating accuracy of such a system will be less than desired.

If ultraprecise mapping can be developed for interventional electrophysiology, such maps could significantly enhance the ability to identify pathways for reentrant tachycardias.<sup>14–28</sup>

## Materials and Methods

### Scanning Beam Imaging System

Conventional fluoroscopy systems use a point x-ray source and a large-diameter image intensifier to produce images (Fig. 1). The Cardiac Mariners (Los Gatos, CA) scanning beam digital x-ray (SBDX) system<sup>39</sup> uses a dramatically different geometry as it has a large x-ray source and a small detector (Fig. 2). The small detector is important for substantially reducing the acceptance of x-ray scatter. The SBDX detector has a 1.8-m diameter (as do I) with the 1.8- to 1.0-m diameter of the image intensifier. Also, the SBDX detector is farther away from the patient (the scatter source) than the image intensifier, resulting in a large air-gap effect. This results in the SBDX detector seeing a scatter reduction of greater than 100-fold as compared with an image-intensifier system. Because scatter has been virtually eliminated from the image, there is no need for a grid in front of the detector.

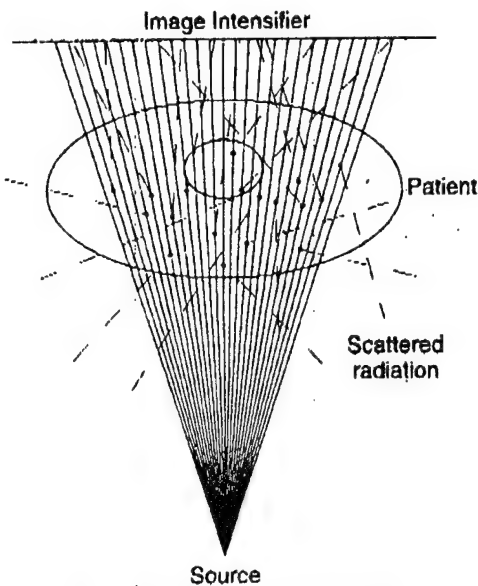


Fig. 1. Conventional x-ray system.

The large source is a conventional point source of x-ray radiation directed by a collimator, with in which produces a narrow beam of x-rays aimed toward the small detector. Each of the individual sources is pulsed sequentially to scan the overall field of view.

Figure 3 shows how the large x-ray source is produced by raster scanning an electron beam across a large liquid-cooled target positioned behind a collimator. The electron gun operates at between 70 and 100 kV. The collimator is 12.7-mm-thick molybdenum, 25.4 cm in diameter with approximately 200,000 holes on 0.51-mm centers. The axis of each 0.38-mm-diameter hole is different in order

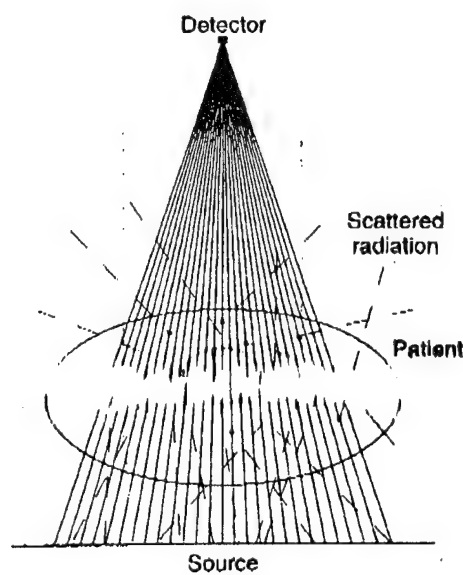


Fig. 2. Scanning beam digital x-ray system.

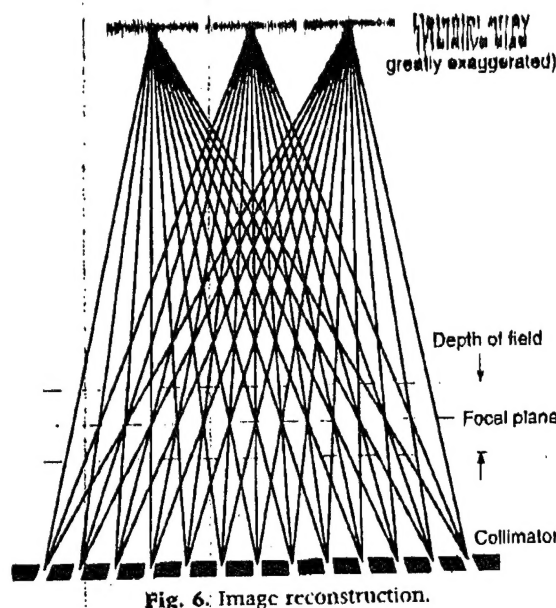


Fig. 6. Image reconstruction.

The two-dimensional detector array is made up of 96 scintillator crystals optically coupled to a 96-channel photomultiplier tube. X-ray intensity is measured by counting x-ray photons resulting in image signal digital-to-analog ratio is determined almost entirely by quantum effects. The detector chain (scintillator, photomultiplier tube, and associated electronics) discriminates single x-ray photons, 20 keV or greater, and counts them up to a rate of approximately  $10^7$  photons/s.

The image reconstruction hardware collects 96 data samples for each collimator hole illuminated and performs the required reconstruction summation in real time to produce  $500 \times 500$  pixel images at a 30-Hz frame rate. A key concept in the mathematical reconstruction is the creation of a plane of best focus (Fig. 6). Objects at a distance from this plane are subject to tomographic blurring. This is useful for improved imaging of the heart inside the chest cavity. The focal plane of the SBDX system is 24 cm from the source, has a field of view of 19 cm, and has a depth of field of approximately 7 cm. The system reconstructs 500 pixels across the 19-cm field of view and therefore has a pixel pitch of 0.38 mm in the focal plane.

A further important benefit of the geometry associated with SBDX technology is the larger patient entrance area.

With this technology, the dose to the patient is reduced. If done, it does reduce the entrance exposure, which is the cause of erythema and epilation in procedures with long fluoroscopy times.

The SBDX fluoroscopy system described here is expected to have comparable image quality ( $500 \times 500$  pixels at true 30-Hz frame rate) but at an order of magnitude lower exposure rate than current systems, which operate typically between 2 and 5 R/min at the patient entrance for cardiac procedures. The exposure reduction arises from four main contributors described above: elimination of effects of scatter, elimination of grids between the patient and detector, improved-efficiency x-ray detector, and larger entrance aperture.

## Two-dimensional Locating

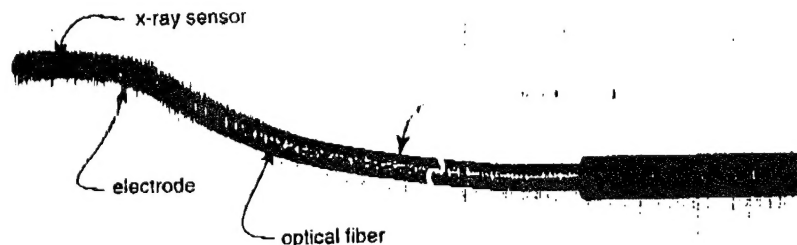
The location of the distal end of a catheter in the SBDX beam can be determined by placing a scintillator-tipped optical fiber inside the catheter,<sup>40</sup> as shown in Figure 7. The optical fiber is connected to an optical detector to measure the light output from the scintillator as a function of beam position. As the x-ray source scans the field of view, the x and y coordinates of the scintillator can be determined by noting when the scanning x-ray beam illuminates the scintillator.

Figure 8 shows a data set of the expected intensity detected by the catheter scintillator as a function of the position of the scanning beam. The catheter's location in the x and y directions is at the centroid of the peak illumination. Because the catheter is located inside a scattering medium, in addition to the direct radiation, the scintillator will also detect some scattered radiation. The mapping and reference catheters all have scintillators, and the position of the mapping catheter is determined relative to the reference catheters. The data must still be gated to the cardiac cycle, but because the mapping and reference catheters are intracardiac, the respiratory cycle and patient movement will have only a small effect on positional accuracy.

## Three-dimensional Locating

The location of the scintillator can be determined in two dimensions using the above technique, and the third dimension<sup>41</sup> can be obtained using a similar technique from

Fig. 7. Locating catheter construction.



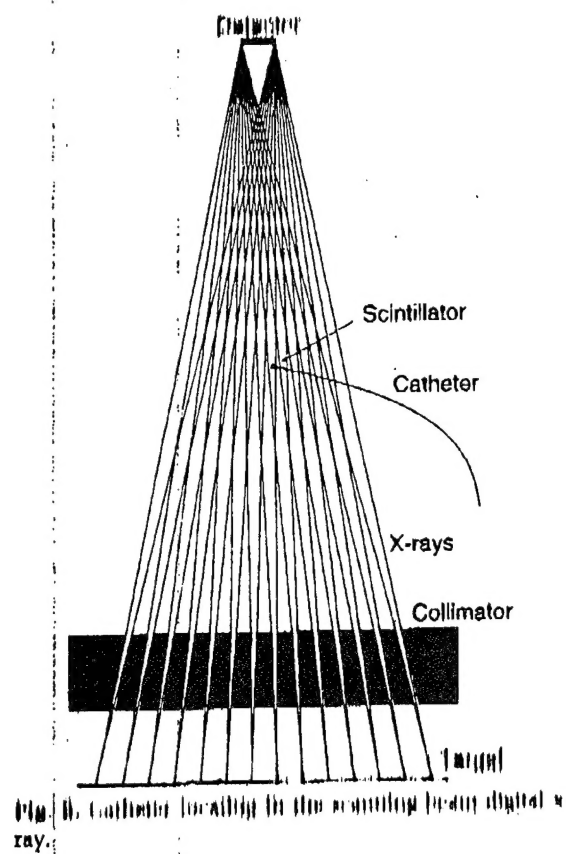


Fig. 8. Catheter location in the resulting beam digital x-ray.

Fig. 9. Intensity measured by the scintillator as a function of x and y beam positions.

two x-ray sources as in a biplane or stereo version of the SBX.

## Results

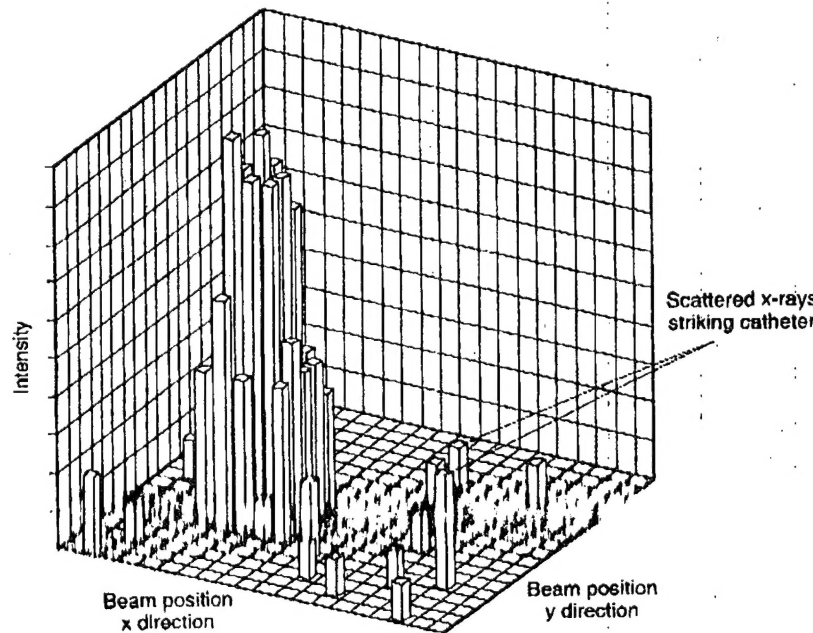
An engineering prototype of the SBX has produced images of a variety of phantoms. These images have, to date, verified the low-dose high-image-quality design.

Engineering prototypes of steerable 7F quadrupolar mapping/ablation catheters have been fabricated. These contain a scintillator-tipped optical fiber (Fig. 10). Tests have demonstrated the ability of these catheters to detect x-ray photons inside a chest phantom.

Further work is needed to develop the algorithms necessary to calculate the position of the scintillator in two dimensions. Development of a stereo or biplane version is planned to demonstrate three-dimensional location accuracy.

## Discussion

Although there are many reasons for the lower success rate of ablation as a treatment for complex tachyarrhythmias, one major problem is the lack of accurate mapping tools. Research in humans has been hindered by inadequate mapping tools and concern for the safety of patients and staff due to radiation exposure. The SBX imaging system described here addresses these issues by substantially reducing the radiation exposure and,



## 3-D Endocardial Mapping System • Moorman et al. 145

long radiation exposure in the cardiac catheterization laboratory? *J Am Coll Cardiol* 23:347, 1994

23. Cascade PN, Peterson LE, Wajszczuk WJ, Mantel J: Radiation exposure to patients undergoing percutaneous transluminal coronary angioplasty. *J Am Coll Cardiol* 4:725, 1984

24. Biese J: Radiation exposure risks haunt interventionists. *Dtsch Imaging* 15:68, 1993

25. Brody WR: Non-invasive imaging: a problem with radiation. *Diagnostic Imaging*, Miller Freeman Magazine, San Francisco, 1992

26. Pratt TA, Shaw A: Factors affecting the radiation dose to the lens of the eye during cardiac catheterization procedures. *Br J Radiol* 66:346, 1993

27. Jenkins KJ, Walsh EP, Colan SD et al: Multipolar endocardial mapping of the right atrium during cardiac catheterization: description of a new technique. *J Am Coll Cardiol* 22:1105, 1993

28. Chilson RA, Shudi KW: Intraventricular multielectrode cardiac mapping probe and method for using same. US Patent 4,699,147 Oct, 1987, assigned to Cardis Corp

29. Kaltenbrunner W, Cardinal R, Dubuc M et al: Epicardial and endocardial mapping of ventricular tachycardia in patients with myocardial infarction. *Circulation* 84:1058, 1991

30. Prager NA, Gox JL, Lindsay BD et al: Long-term effectiveness of surgical treatment of ectopic atrial tachycardia. *J Am Coll Cardiol* 11:81, 1983

31. Saxon LA, Stevenson WG, Bonow RO et al: Transesophageal echocardiography during radiofrequency catheter ablation of ventricular tachycardia. *Am J Cardiol* 72:658, 1993

32. Langberg JJ, Franklin JO, Landzberg JS et al: The echotransponder electrode catheter: a new method for mapping the left ventricle. *J Am Coll Cardiol* 12:218, 1988

33. Kuck KH, Schlüter M, Geiger M, Siebels J: Successful catheter ablation of human ventricular tachycardia with radiofrequency current guided by an endo-epicardial dual-plane catheter. *PACE* 14:1000, 1991

34. Ometto R, Bedogni F, LaVecchia L et al: Radiofrequency catheter ablation of the slow reentrant pathway of sustained ventricular tachycardia. *PACE* 16: 1891, 1993

35. Stevenson WG, Weiss JN, Wiener I, Nademanee K: Slow conduction in the infarct scar: relevance to the occurrence, detection, and ablation of ventricular reentry circuits resulting from myocardial infarction. *Am Heart J* 117:452, 1989

36. Josephson ME, Gottlieb CD: Ventricular tachycardia associated with coronary artery disease. p. 573. In Zipes DP, Jalife J (eds): *Cardiac electrophysiology from cell to bedside*. WB Saunders, Philadelphia, 1990

37. Stevenson WG, Khan H, Sager P et al: Identification of reentry circuit sites during catheter mapping and radiofrequency ablation of ventricular tachycardia late after myocardial infarction. *Circulation* 87(Part 1): 1647, 1993

38. Wilent J, Moorman JW, Skillcorn B, Flekowsky P: X-ray detector for a low dosage scanning beam digital X-ray imaging system. Patent pending, assigned to Cardiac Mariners

39. Moorman JW, Wilent J: Catheter including an x-ray sensitive optical-sensor locating device. Patent pending, assigned to Cardiac Mariners

40. Moorman JW, Wilent J: Catheter including an x-ray sensitive optical-sensor locating device. Patent pending, assigned to Cardiac Mariners

41. Wilent J: Optical and apparatus for determining the location of an x-ray sensing catheter within an object undergoing x-ray examination by a scanning beam x-ray apparatus. Patent pending, assigned to Cardiac Mariners

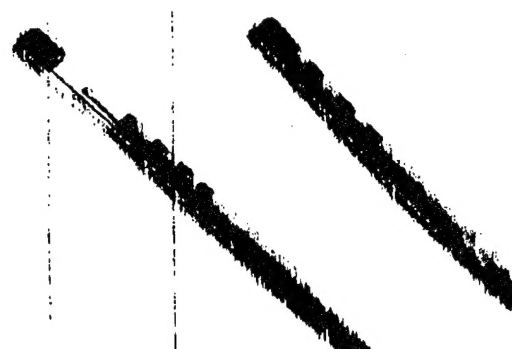


**Fig. 10.** Electrophysiology mapping catheter with scintilla-tipped optical fiber.

when combined with modified EP catheters, allows endocardial locations to be recorded. The three-dimensional maps created are expected to be significantly more accurate than previous closed-chest techniques, possibly improving the understanding of complex tachycardias and the success rates of RFCA.

Improved mapping may involve existing tools used in combination with this new locating technique. For example, smaller multinodal arrays can overcome the objections listed earlier if their location and orientation is accurately determined using multiple scintillators. Adjunctive tools, such as echocardiography, may assist in confirming the anatomic landmarks used, and previously acquired magnetic resonance imaging or computed tomography images may be correlated with the maps created using the locating catheters.

The eventual success of ablation therapy may depend on the availability of the above-mentioned tools and on the research performed with those tools.

#### References

1. Langberg JJ, Chin MC, Rosenqvist M et al: Catheter ablation of the atrioventricular junction with radiofrequency energy. *Circulation* 80:1527, 1989
2. Jazayeri MR, Himpel SL, Sra JS et al: Selective trans-catheter ablation of the fast and slow pathways using radiofrequency energy in patients with atrioventricular nodal reentrant tachycardia. *Circulation* 85:1318, 1992
3. Jackman WM, Wang X, Friday KJ et al: Catheter ablation of accessory atrioventricular pathways (Wolff-Parkinson-White syndrome) by radiofrequency current. *N Engl J Med* 324:1605, 1991
4. Klein LS, Shih HT, Hackett FK et al: Radiofrequency catheter ablation of ventricular tachycardia in patients without structural heart disease. *Circulation* 85:1666, 1992
5. Cohen TJ, Chien WW, Lurie KG et al: Radiofrequency catheter ablation for treatment of bundle branch reentrant ventricular tachycardia: results and long-term follow-up. *J Am Coll Cardiol* 18:1767, 1991
6. Walsh EP, Saul JP, Hulse JE et al: Transcatheter ablation of ectopic atrial tachycardia in young patients using radiofrequency current. *Circulation* 86:1138, 1992
7. Calkins H, Kalbfleisch SJ, El-Atassi R et al: Relation between efficacy of radiofrequency catheter ablation and site of origin of idiopathic ventricular tachycardia. *Am J Cardiol* 71:827, 1993
8. Scheinman MM: Catheter ablation for cardiac arrhythmias: personnel and facilities. *PACE* 16:713, 1993
9. Halperin DH: The biophysics of radiofrequency catheter ablation in the heart: the importance of temperature monitoring. *PACE* 16 (Part II):586, 1993
10. Lickm LB: Catheter ablation for the treatment of ventricular tachycardia. In Sung RJ (ed): *Management of cardiac arrhythmias: an update*. Stanford University School of Medicine, Stanford, 1993
11. Ruskin JN: Catheter ablation for supraventricular tachycardia. *N Engl J Med* 324:1660, 1991
12. Chen SA, Chiang CE, Yang CJ et al: Radiofrequency catheter ablation of sustained intra-atrial reentrant tachycardia in adult patients. *Circulation* 88:578, 1993
13. Nakagawa H, Beckman KJ, McClelland JH et al: Radiofrequency catheter ablation of idiopathic left ventricular tachycardia guided by a Purkinje potential. *Circulation* 88:2607, 1993
14. Feld GK, Fleck RP, Chen PS et al: Radiofrequency catheter ablation for the treatment of human type 1 atrial flutter: identification of a critical zone in the reentrant circuit by endocardial mapping techniques. *Circulation* 86:1233, 1992
15. Josephson ME, Horowitz LN, Spielman SR et al: Role of catheter mapping in the preoperative evaluation of ventricular tachycardia. *Am J Cardiol* 49:207, 1982
16. Stevenson WS, Weiss MT, Wyman EF et al: Partitioned atrial and ventricular conduction and the atrial ventricular conduction in humans: evidence from pace-mapping. *J Am Coll Cardiol* 13:369, 1989
17. Pattee PL, Johns PC, Chambers RJ: Radiation risk to patients from percutaneous transluminal coronary angioplasty. *J Am Coll Cardiol* 22:1044, 1993
18. Bell MR, Berger PB, Menke KK, Holmes DR: Balloon angioplasty of chronic total artery occlusions: what does it cost in radiation exposure, time and materials? *Cathet Cardiovasc Diagn* 25:10, 1992
19. Calkins H, Niklason L, Sousa J et al: Radiation exposure during radiofrequency catheter ablation of accessory atrioventricular connections. *Circulation* 84:2376, 1991
20. Kuck KH, Schluter M: Single-catheter approach to radiofrequency current ablation of left-sided accessory pathways in patients with Wolff-Parkinson-White syndrome. *Circulation* 84:2366, 1991
21. Kuck KH, Schluter M, Geiger M et al: Radiofrequency current catheter ablation of accessory atrioventricular pathways. *Lancet* 337:1557, 1991
22. Pederman J, Bell MR, Wondrow MA et al: Does the use of a new intracoronary interventional devices pro-